HI View of the Norma Galaxy Cluster with MeerKAT

By

Koketso Vincent Mophahlane

Supervisors

Dr Mpati Ramatsoku

Prof Oleg Smirnov

Department of Physics & Electronics

Faculty of Science, Rhodes University

September 19, 2023

HI View of the Norma Galaxy Cluster with MeerKAT

By

Koketso Vincent Mophahlane

Supervisors

Dr. Mpati Ramatsoku

Prof. Oleg Smirnov

A research project submitted in conformity with the requirements

for

the degree of Masters of Science in Physics

(Extra-galactic Studies & Observational Radio Astronomy)

Department of Physics & Electronics

Rhodes Center for Radio Astronomy Techniques and Technologies

(RATT)

Faculty of Science, Rhodes University

South Africa

September 19, 2023

Abstract

Studies reveal that galaxies assemble into clusters as gas-rich, active star-forming disks and eventually settle in the virialized core as quenched early-type galaxies with depleted gas. To examine environmental effects responsible for the quenched population in the cluster core, we exploit the higher sensitivity of the MeerKAT telescope to probe HI properties of galaxies in the Norma cluster. The Norma cluster is an ideal laboratory for this study since it is a rich and massive cluster of nearby galaxies.

The HI data cube used covers a velocity range of $483 - 11,113$ km/s, with a noise rms sensitivity of 0.09 mJy/beam and an angular resolution of $\sim 14.65'' \times 9.28''$. A total of 25 reliable HI sources were detected over the entire velocity range. The HI detections reveal two major galaxy overdensities located at $v_{rad} \sim 2096 - 7646$ km/s and $v_{rad} \sim 10,000$ km/s. The first is associated with the Norma cluster gravitational potential and indicates a substructure in its velocity distribution; the other is a population of background galaxies. In this work, the Norma cluster has 13 cluster members detected in HI and 130 galaxies from optical surveys. The spatial distribution of cluster members covers a field that is $2/3 \times R_A$, where $R_A = 2.02$ Mpc at $cz = 4871$ km/s. From the spatial distribution, optical galaxies are densely populated in the central regions, while most galaxies in HI were detected on the outskirts. From the phase-space diagram, 6 galaxies detected in HI are found in the virialised region, while the rest of the detections are infalling for the first time. HI detections that are not yet virialised have asymmetrical morphologies, while virialised detections have truncated gas disks. Most cluster members that were found to have asymmetrical gas disks are also HI deficient by $0.8 - 1.2$ dex but show excess SFR efficiency for the amount of HI detected. The results demonstrate that the initial phase of galaxy-ICM interactions might be responsible for morphological transformation and enhancement of star formation activity.

Contents

List of Figures

List of Tables

Acknowledgments

Words cannot express my gratitude to my supervisor, Dr. Mpati Ramatsoku, for her infinite patience, valuable and prompt feedback, training, and the knowledge she imparted along the way. I am very grateful for all the minutes and hours I stole from you during weekends and even during your leave (very sorry for that). I appreciate the RATT research chair and supervisor, Prof Oleg Smirnov, for making this journey bearable and for the radio astronomy training during busy week, the student journals, the coffee machine, the extra funding for broken equipment and expensive conference trips. I am indebted to you for the knife-throwing and gun-shooting activities at the farm. I "have a very particular set of skills," which I have acquired through a lengthy thesis writing period.

The Norma cluster in HI was observed with the MeerKAT telescope. The MeerKAT telescope is operated by the South African Radio Astronomy Observatory, which is a facility of the National Research Foundation, an agency of the Department of Science and Innovation. This endeavour would not have been possible without the generous support from SARAO. I also thank Prof Thomas Jarrett for sending WISE data from his private catalogue and Prof Patrick Woudt for providing MeerLICHT images of the Norma cluster. I could not have undertaken this journey without the office RATTs, Robert, Eric, Kamva, and Charles. My friends have generously provided knowledge and expertise whenever I was struggling with code or when I needed some cheering after my thesis draft came back with red/yellow/green/black highlights. It was during those days that they shared some relevant information about Fegelein, "astronaut chickens", "Mpati log-scale" and "blesser AGNs". Lastly, I am thankful to my partner, Letlhogonolo Selolo, who has known me since undergrad while I was still a dreamer. I thank my mother, Annah Mophahlane, who gave birth to me and did everything she could to support my dreams.

Chapter 1

Introduction

1.1 Galaxy clusters

Clusters of galaxies are the largest known gravitationally bound overdensities whose studies have proven them to be unique laboratories for probing the main processes that govern galaxy evolution (e.g., Solanes et al. 2001; Koopmann & Kenney 2004; Braglia et al. 2009; Grossi et al. 2015; Boselli et al. 2016; Chung et al. 2017). The interactions within these dense environments are agents of morphological transformation that occur through the removal of interstellar medium (ISM) gas and quenching of star formation (SF) activity (Bahé et al. 2013). They occur in galaxy clusters more frequently since they contain hundreds to thousands of galaxies and have a typical mass range of $10^{14} - 10^{15}$ $M_{\odot}$ and an average velocity dispersion of $\sigma_{cl} \sim 1000$ km/s, translating into the high likelihood of interactions responsible for the physical transformation of galaxies (Abell 1958; Bahcall 1996; Carlberg et al. 1996; Panko 2015; Ranchod et al. 2021).

Galaxy clusters are small compared to cosmological scales but contain essential information about the Universe because they form part of inter-filamentary clumps of dark matter. These clumps are due to the gravitational attraction of dark matter halos as well as the repeated structural merging of galaxies into larger gravitationally bound structures (Bahcall 1996; Kravtsov & Borgani 2012).

Clusters contain galaxies, dark matter, intracluster stars (faint diffuse light), the highly luminous hot gas, as well as the intracluster medium (ICM) (Sarazin 1988; Zwicky 1933; Donahue 1998). The ICM is a superheated, X-ray-emitting dense plasma in the centres of clusters. It is composed mostly of baryonic matter comprising of ionized hydrogen

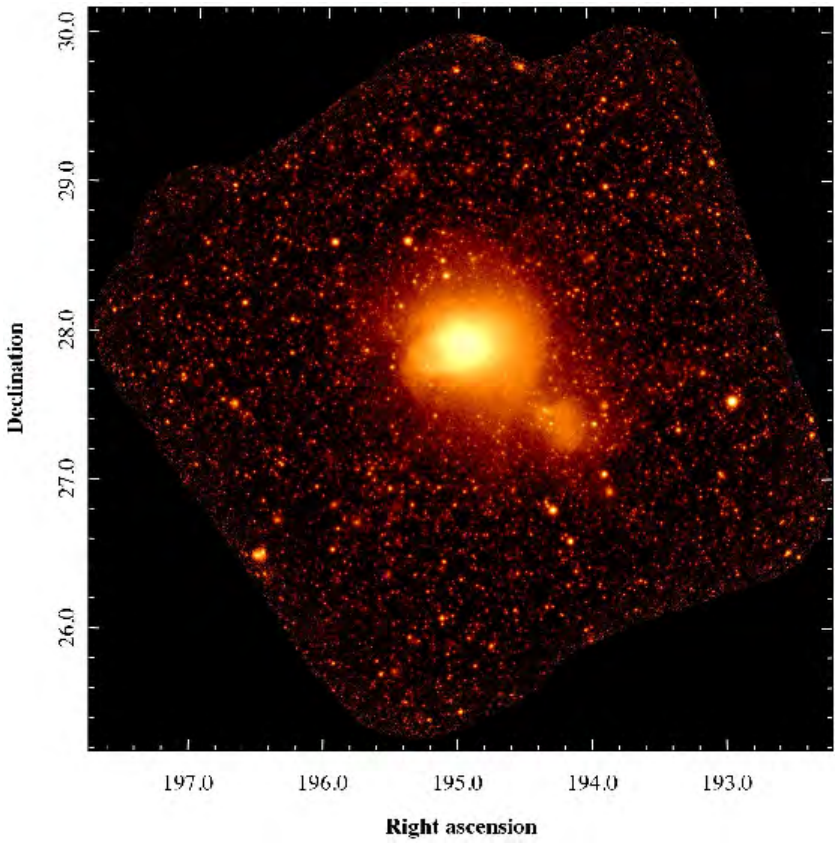

Figure 1.1: The X-ray image of the Coma cluster in the $0.4 - 2$ keV band observed with the eROSITA space telescope, adopted from Churazov et al. (2021). The image illustrates the peak X-ray luminosity of the cluster core where the ICM is most dense and the smooth luminosity integration into the halo.

and helium, as well as heavier elements such as iron (Kotov & Vikhlinin 2006; Sparke & Gallagher III 2007; Staniszewski et al. 2009). Observations of nearby clusters have determined that cluster metallicity (i.e., the ratio of heavier elements to hydrogen) peaks in the cores of most clusters (e.g., Press & Davis 1982; Mohr et al. 1995; Allen & Fabian 1998; De Lucia et al. 2004; Tornatore et al. 2007; Leccardi & Molendi 2008; Biffi et al. 2017). The ICM metal content is enriched through deposits from dying stars (Mazzei et al. 2018). It is heated to temperatures on the order of 10 to 100 MK, emitting strong X-ray radiation, mainly by the bremsstrahlung process, and comprises roughly 10% of the mass of clusters (Zwicky 1937; Sarazin 1988; Böhringer & Werner 2010).

Figure 1.1 is an X-ray image of the well-known Coma cluster observed with the eROSITA space telescope (Churazov et al. 2021). The X-ray image adequately illustrates the ICM, highly luminous intergalactic gas, and a few visible galaxy members.

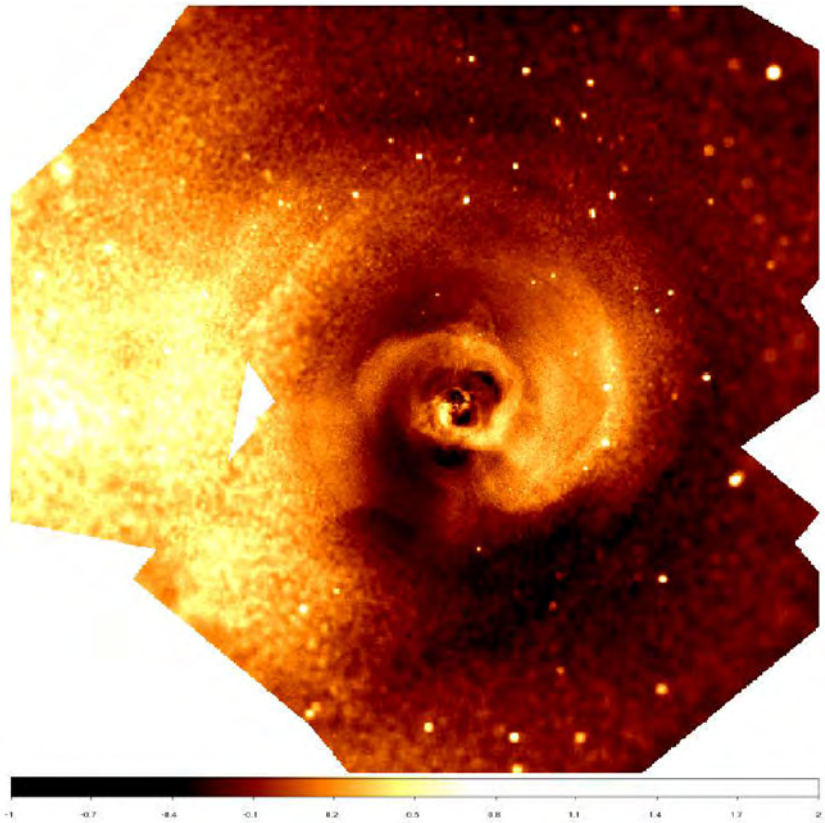

Figure 1.2: The ICM in the core of the Perseus cluster in the $0.5 - 7$ keV band spanning $25.6'$ from N to S, viewed with the Chandra Flagship-class X-ray space telescope (Fabian et al. 2011). The hot plasma in the image demonstrates the havoc and dynamic processes in the cluster core.

Figure 1.2 shows the dynamical processes in the core of the Perseus cluster due to the ICM plasma. The gravitational well of the cluster comprises 50 MK X-ray emitting hot plasma from the relativistic jets in the Active Galactic Nucleus (AGN) of the central galaxy NGC 1275, inducing motions in the ICM (Hitomi Collaboration et al. 2016).

1.2 Galaxy classification scheme

Galaxies consist of stellar disks containing $10^6 - 10^{12}$ stars; interstellar dust grains that absorb starlight and later re-emit as infrared (IR) light; loosely-bound gas disks; and dark matter. The stellar disk, gas disk, and dark matter typically constitute $3 - 5\%$, $\sim$ 12%, and $\sim$ 84% of the galaxy mass, respectively. Hubble (1926) formulated a preliminary classification of galaxies shown in Figure 1.3, which groups into four main types: spirals (SB- for barred spirals and S- for unbarred spirals), lenticulars (S0-),

ellipticals (E-) and irregulars (Irr). Figure 1.4 presents examples of a barred spiral galaxy (NGC 1300), a bright dwarf irregular galaxy (NGC 1427A), a massive elliptical galaxy (ESO 325-G004), and a massive lenticular galaxy (NGC 6861).

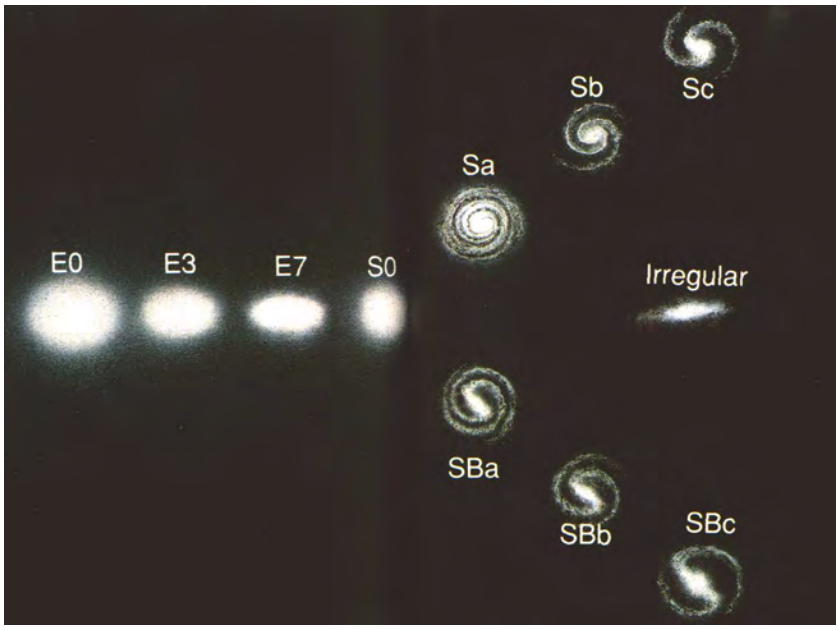

Figure 1.3: Hubble's "tuning fork" diagram illustrates a primitive model that classifies morphological types along a sequence from E, transitioning into S0 and branching into SB (with bars) and S (without bars).

Spiral galaxies are typically gas-rich, star-forming systems that possess a twisted physical feature dominated by two or more spiral arms curling around the disk, indicating the system's rotational direction (Hubble 1937; Bournaud et al. 2009; Randriamampandry et al. 2021). Their physical structure includes a bulge surrounded by a flat, rotating disk of older, dimmer stars at the galaxy's centre.

NGC 1300 in Figure 1.4, panel (a)[1], is a barred spiral galaxy, SB(rs)bc, located in the Eridanus cluster (De Vaucouleurs et al. 1976; Lindblad & Kristen 1996, Lindblad & Kristen 1996; Lindblad et al. 1997). It has two spiral arms that spring from the two ends of the central bar, which consist of star-forming clouds, clusters of new stars, and dust lanes (Sandage 1961; England 1989a; England 1989b). The VLA[2] 21 cm observations of NGC 1300 reveal that the neutral gas is almost completely restricted to the spiral arms, while the central optical bar has very little gas, which could suggest that the galaxy has

[1]HST image of NGC 1300, https://hubblesite.org/contents/media/images/2005/01/1636-Image.html
[2]Large Array Telescope in New Mexico, http://www.vla.nrao.edu/

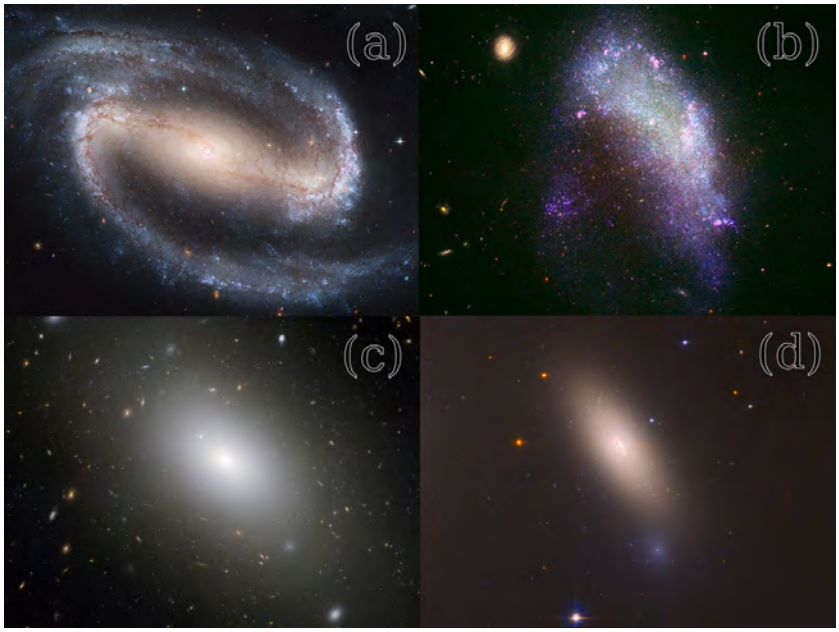

Figure 1.4: Examples of different galaxy morphologies according to the Hubble "tuning" fork classification scheme. Panel (a) is NGC 1300, a barred spiral galaxy, SB(rs)bc, in the Eridanus cluster. Panel (b) is NGC 1427A, a bright dwarf irregular galaxy, dIrr, and the brightest dwarf irregular galaxy in the Fornax cluster. Panel (c) is ESO 325-G004, which is a massive elliptical galaxy, E, that lies at the centre of Abell S0740. Panel (d) is NGC 1277, a peculiar lenticular galaxy (S0, pec) in the Perseus cluster.

had intense SF activity in the central regions (Sandage 1961; England 1989a, 1989b).

Irregular galaxies, unlike the spirals, do not possess any regular shape, nor have a central bulge of stars or spiral arms, but instead appear distorted, possibly due to a recent gravitational interaction with a neighbour object or due to intense bursts of star-forming clouds, causing chaotic arrangement of young stars (Hubble 1937; Tayler 1993; Binney & Tremaine 2011). Irregular galaxies are gas-rich (ISM gas contributes more than 30% of the mass), with large ionized gas (HII) regions (Tayler 1993; Binney & Tremaine 2011).

One such example is NGC 1427A (Fig. 1.4, panel (b)[3]), which is a bright dwarf irregular galaxy (dIrr) in the Fornax cluster. It has no nucleus, no central bulge, and no spiral arms. Instead, it has a distorted ring that consists of gaseous clusters and star-forming regions (Cellone & Forte 1997; Hilker et al. 1997; Chanamé et al. 2000; Mora et al. 2015;

[3]HST image of NGC 1427A https://hubblesite.org/contents/media/images/2005/09/1662-Image.html

Lee-Waddell et al. 2018); and a higher than average gas content for irregular galaxies (Hunter & Gallagher III 1985; Cellone & Forte 1997). Cellone & Forte (1997) suggested that its peculiar morphology is either the result of distortion caused by gravitational interactions between a faint northern object characteristic of dwarf E/Irr galaxies in the Fornax cluster and elliptical isophotes which is a plume-like southern half of the galaxy.

Elliptical galaxies, on the other hand, have an ellipsoidal shape and are typically early-type galaxies (Hubble 1937; Kuntschner 2000; Naab et al. 2006). Unlike the spirals, their rotation is slower and in random directions (Pedraz et al. 2002; Toloba et al. 2015). Ellipticals are known as "dead" galaxies since they comprise old stellar populations due to gas depletion induced by environmental interactions, which leads to the quenching of SF activity (Salim et al. 2012).

ESO 325-G004 (Fig. 1.4, panel (c)[4]) in the centre of the Abell cluster S0740 is a giant elliptical galaxy (E) with a bulge consisting of thousands of gravitationally bound globular clusters, a halo and with strong gravitational lensing (e.g., Smith et al. 2005; KOLE 2018; Collett et al. 2018; Gurzadyan & Stepanian 2018; Yang et al. 2019).

Lenticular galaxies are also early-type galaxies that sit between elliptical and spiral galaxies and constitute mainly the nucleus (Hubble 1937). They have a thin, rotating disk of stars, a central bulge, and little dust and gas in the ISM, and they seem to form more often in densely populated regions (Van den Bergh 2009) such as the cluster cores.

NGC 1277 (Fig. 1.4, panel (d)[5]) is a massive early-type ($z > 2$) peculiar lenticular galaxy (S0, pec; Corwin et al. 1994) with a massive black-hole (van den Bosch et al. 2012). Trujillo et al. (2013) define NGC 1277 as a relic since (i) the galaxy consists only of a population of older stars ($\sim$ 8 Gyrs old). (ii) No recent SF activity is observed. Quenching may have been caused by extreme bursts of SF activity over a period of 100 Myrs, about 12 Gyrs years ago (van den Bosch et al. 2012). (iii) It is massive and compact and shows no signs of external interactions.

According to the morphology-density relation (Dressler 1980), spirals are often found in the cluster outskirts, where they are sparsely distributed. However, ellipticals and lenticulars are mainly located in cluster cores, with a high concentration of galaxies and the hot, dense, X-ray-emitting ICM.

[4]HS image of ESO 325-G004, https://esahubble.org/images/opo0708b/

[5]HST image of NGC 1277, https://hubblesite.org/contents/media/images/2018/17/4137-Image.html

1.3 The environment and gas removal processes

Most galaxies in the local universe ($\sim 74\%$, at $z \lesssim 0.1$) are clumped together in virialized groups and clusters. The remaining populations are "field galaxies" found in pairs and compact groups in underdense regions, and "lonely galaxies" (void galaxies) that appear completely isolated in filamentary voids (Argudo-Fernández et al. 2015).

Therefore, galaxy evolution appears accelerated in overdense environments such as clusters (Cerulo et al. 2016). This is because interactions between a galaxy and its local environment can (i) first compress the ISM gas, enhance SFR during the initial phase, and (ii) eventually remove the ISM gas and suppress SF activity. Figure 1.2 (briefly discussed above) is an example of a chaotic, hot, dense environment in the centre of the Perseus cluster, where galaxies are processed.

Within cluster environments, galaxy evolution takes place, and galaxies are transformed from late-type S/Irr to early-type E/S0 (Thomas et al. 2005; Clemens et al. 2006; Haines et al. 2007; Park & Hwang 2009). The agents of galaxy transformation in clusters may be in the form of gravitational (e.g., galaxy-galaxy) or hydrodynamical (e.g., galaxy-ICM) interactions.

1.3.1 Galaxy-galaxy interactions

Gravitationally interacting galaxies are galaxies whose gravitational fields disturb one another (Bothun & Dressler 1986). An example of a minor interaction is a satellite galaxy disturbing the primary galaxy's spiral arms (e.g., Byrd 1988; Gordon et al. 2006; Semczuk et al. 2017; Zasov et al. 2019). An example of a major interaction is a galactic collision in which galaxies collide violently and merge, subsequently stripping their ISM gas and disrupting their morphology. This interaction commonly results in more massive elliptical galaxies, depending on the collision angle as well as the relative speeds and sizes of the interacting galaxies (Toomre 1977; Negroponte & White 1983; Zepf & Ashman 1993; Barnes & Hernquist 1996; Iono et al. 2004; Bridge et al. 2007; Di Matteo et al. 2007; Conselice et al. 2009; Dekel et al. 2009; Hopkins et al. 2009; Lambas et al. 2012; Kaviraj et al. 2014; Fiacconi et al. 2015; Zolotov et al. 2015; Deeley et al. 2017; Goulding et al. 2017; Zeng et al. 2021).

Tidal gravitational interactions may result in cannibalism in which the larger galaxy

accretes gas from its companion, resulting in a larger, irregular galaxy (Hausman & Ostriker 1978; Balick & Heckman 1981).

In other cases, such as flybys, galaxies do not permanently unite but only come close enough due to a massive mutual gravitational potential and pull away each one on its own orbital path (Miller 1986; Moore et al. 1999; Sinha & Holley-Bockelmann 2012; Martin et al. 2021). The interaction can disrupt and strip the ISM gas in the interacting galaxies.

1.3.2 Harassment

Harassment occurs when a galaxy encounters frequent, high-speed flybys from neighbour galaxies while transitioning into the dense cluster core along its orbital path (Moore et al. 1996). Such interactions are known to severely disrupt the gas and stellar disk morphology of the "harassed" galaxy, and often induce instantaneous starbursts in a gas-rich galaxy and tidal tails in rich Coma-like clusters, consuming all the star-forming reservoir gas (e.g., Moore et al. 1996, Moore et al. 1998; Ghigna et al. 1998; Mayer et al. 2001; Davies et al. 2005; Knebe et al. 2006; Popesso et al. 2006; Smith et al. 2010; Vivek et al. 2022). However, if less severe, galaxy harassment will only disrupt the extended gaseous halo, thereby preventing the gas from cooling and forming stars (Dressler et al. 2013; Cattaneo 2015; Peng et al. 2015).

1.3.3 Starvation

Starvation (or strangulation) is a non-environmental quenching process that is only slightly connected to external interactions (Peng et al. 2010; Wetzel et al. 2013). The quenching process occurs when a galaxy ISM gas is consumed as it forms stars or when the gas cannot condense due to inefficient cooling processes. Such inherent mechanisms may be caused by ejective feedback driven in massive galaxies that host massive black holes, which remove the ISM gas from galaxies, thus halting SF activity (Gabor et al. 2011; Nelson et al. 2019; Terrazas et al. 2020; Piotrowska et al. 2021). It can also occur when the surrounding circumgalactic medium is heated via energy injection through radio jets and winds, halting cold gas accretion and suppressing SF activity (e.g., Gabor et al. 2011; Gaspari et al. 2012; Zinger et al. 2020). Starvation is the main quenching mechanism for low mass galaxies, i.e., $\log(M_\star/M_\odot) < 11$, where the metallicities of

galaxies increase rapidly, due to the lack of inflow of external gas (e.g., Fabian 2012; Cicone et al. 2014; King & Pounds 2015; Fluetsch et al. 2019).

1.3.4 Ram-pressure stripping

Ram-pressure stripping (RPS) is a gas-only stripping mechanism that occurs when an infalling galaxy encounters the ICM wind while crossing through the cluster centre. As the galaxy "rams" through the hot, dense environment, the ICM winds push back against the galaxy ISM. If the ICM wind is strong enough to overcome the galaxy's capacity to hold on to its gas, the ISM gas is then effectively pushed into the parallel tentacle tails (Gunn & Gott 1972; Abadi et al. 1999; Vollmer et al. 2001a; Hester 2006; Kapferer et al. 2008; Kapferer et al. 2010; Bekki 2014; Roediger et al. 2015; Steinhauser et al. 2016; Jaffé et al. 2018; Wang et al. 2020). Initial interactions with the ICM can compress the galaxy's ISM gas and enhance SF activity. Several encounters with the ICM can eventually strip the gas and cause SF to cease and spiral arms to disappear.

There are still questions remaining that have the focus of many past and current studies on these topics. Studies seek to answer questions such as how much impact environmental effects have in the transformation of galaxies from their point of assembly into the population of early-type, gas-poor, and quenched galaxies in cluster centres and how this impact works in a given galaxy with a given mass and size. The second question is which gas depletion process has the most dominant effect and whether the harsh environment in the cluster core is where galaxies lose their gas and become quenched.

The cluster central region where the ICM is most dense is the resting place for gas-poor and quenched galaxies (or red sequence galaxies) and often the environment where galaxies are transformed. RPS is considered the eventual processing mechanism for galaxies crossing cluster centres while interacting with the ICM. However, even during the transition into the core, infalling galaxies cross paths and are transformed due to mergers, harassment, and flybys (Lewis et al. 2002; Treu et al. 2003). Simpson et al. (2018) showed that many quenched systems cease SF within 1 Gyr of first infall. Therefore infalling galaxies may be pre-processed to some extent or even completely losing their gas content before encountering the ICM (Zabludoff & Mulchaey 1998; Ellingson et al. 2001; Verdes-Montenegro et al. 2001; McGee et al. 2009; De Lucia et al. 2012; Vijayaraghavan & Ricker 2013).

1.4 Radio astronomy and HI

The 21 cm line emission of neutral hydrogen gas (HI) is an important indicator of various environmental mechanisms mentioned in section 1.3. This line emission is the electromagnetic (EM) radiation spectral line that comes from the transition between the two levels of the hydrogen $1s$ ground state. The interaction slightly splits the two levels between the electron spin and proton spin configurations. This results in the emission of a photon with a wavelength that falls within the microwave region of the L-band in the EM spectrum. In its $1s$ ground state, the hydrogen atom consists of an electron and a proton. The electron is not spatially displaced from the proton but encompasses it, causing both particles to interact continually. Both particles possess magnetic dipole moments due to intrinsic properties such as spin and charge. Only parallel and anti-parallel states are allowed. The electron and nuclear spins are 1/2 for the proton, so there are two possible discrete states. The total angular momentum of the system becomes discretized quantum mechanically. The interaction results in a slight increase in energy when the spins are parallel (relatively less tightly bound) and a decrease when anti-parallel (relatively more tightly bound). A photon is emitted when the spins flip from parallel to anti-parallel. This splitting of the hydrogen ground state is extremely small compared to the ground state energy (of 13.6 eV). The difference between the two energy levels is $\Delta \mathrm{E} \approx 5.9$ eV. The emitted photon is thus detectable in the wavelength of;

$$\lambda = \frac{1}{v} \times c = \frac{\mathrm{h}}{\mathrm{E}} \times c \approx \frac{4.14 \times 10^{-15}\ \mathrm{eV/s}}{5.9 \times 10^{-6}\ \mathrm{eV}} \times 3.0 \times 10^{8}\ \mathrm{m/s} = 21.1\ \mathrm{cm}, \tag{1.4.1}$$

where h is Planck's constant and c is the speed of light. The 21 cm line has a frequency of $\sim 14 \times 10^8$ Hz and a very low transition probability. This means large amounts of hydrogen are required for it to be seen.

The thickness of an HI gas cloud can be defined from the equation;

$$\tau_{\mathrm{HI}} = \int_0^{\mathrm{l}} \alpha(\mathrm{s})\, \mathrm{ds}, \tag{1.4.2}$$

where s is the path length of the beam, and l is the thickness of the gas cloud. The attenuation coefficient is defined as $\alpha(\mathrm{s}) = -\frac{1}{\phi_{\mathrm{e}}} \frac{\mathrm{d}\phi_{\mathrm{e}}}{\mathrm{ds}}$, where ϕ_{e} is the radiant flux of the gas cloud. For an optically thin gas cloud, $\tau_{HI} \ll 1$, the column density ($\mathrm{N_{HI}}$, Eqn 2.6.2) and HI mass ($\mathrm{M_{HI}}$, Eqn. 2.3) can be derived from their relations with the flux density

of the source. Flux density (S_v) is related to the brightness temperature (T_B) over the solid angle (Ω) of the source as;

$$S_v = \frac{2k_B}{\lambda^2} \iint T_B d\Omega. \tag{1.4.3}$$

T_B is derived from relations with the spectral radiance B_v based on the Rayleigh-Jeans approximation to Planck's law;

$$T_B = \frac{c^2 B_v}{2k_B v^2}, \tag{1.4.4}$$

where v is the frequency of emission ($v\lambda = c$).

The HI content of a galaxy and its distribution can be used to estimate the relative efficiency of the gas removal mechanisms (Haynes et al. 1984). HI is thus a good tracer of the physical processes at work within a galaxy as it manifests the relation between the ISM gas content and environmental processes during its evolutionary history. This is because galaxy gas disks are far more extended than stellar disks and are the first to collapse during tidal interactions, gas stripping and mergers (e.g., Rosenberg & Schneider 2002; Oosterloo et al. 2007; Sancisi et al. 2008; Chung et al. 2009; Mihos et al. 2012). Furthermore, HI dominates a galaxy's gas content (by mass), making it a useful tracer of the overall gas content.

1.5 Norma galaxy cluster

In this thesis, we study the HI properties of galaxies in the Norma cluster (A3627 or ACO3627). The Norma cluster is a rich, nearby cluster at 67 ± 0.7 Mpc (assuming $H_0 = 73$ km/s/Mpc; Woudt et al. 2007), located near a large localized mass concentration known as the Great Attractor (GA; Kraan-Korteweg & Lahav 2000). The GA is the gravitational focal point of large-scale filamentary structures of the Laniakea supercluster, with a mass concentration that is a thousand times more massive than the Milky Way (MW) galaxy (Burstein et al. 1990; Woudt et al. 2007). The Norma cluster is the most massive cluster in the GA with a dynamical mass of $M_{dyn} \sim 1 - 1.1 \times 10^{15} h_{73}^{-1}$ $M_\odot$ (Woudt et al. 2007) and has not yet reached the state of virialization, since it exhibits galaxy substructures (Woudt et al. 2007). It is hidden behind the MW within the Zone of Avoidance (ZoA). Hence, it is not easily seen with instruments observing at optical wavelengths (Lu et al. 1990). It is comparable in size and richness to the Coma cluster, but it is nearer, thus making the Norma cluster an ideal laboratory to study galaxy

transformation, gas depletion, environmental effects, and how these affect the SF activity of galaxies residing in the cluster (Woudt et al. 2007). The following is a brief summary of the properties of the Norma cluster.

- It is X-ray bright, which reveals how far the ICM is distributed from its core (Bohringer et al. 1996; Woudt et al. 2007).
- It shows signs of an ongoing merger as revealed by its elongated X-ray morphology (Bohringer et al. 1996).
- It harbors an in-falling spiral-rich subgroup (Woudt et al. 2007).
- It contains two central cD galaxies (Woudt et al. 2007) and has two strong radio continuum sources, namely PKS 1610-608 and PKS 1610-605 (Jones & McAdam 1992; Woudt & Kraan-Korteweg 2001).

Within the past three decades, observational studies at multi-wavelengths have revealed interesting galaxies that are transformed in the dense environments of the Norma cluster (e.g., dating from Bohringer et al. 1996). Using the Hubble Space Telescope (HST) and the Atacama Pathfinder Experiment (APEX) telescope, an interesting galaxy called the ESO 137-002 shown in Figure 1.5 (Laudari et al. 2022) was revealed to feature disk perturbations and asymmetric distribution of dust clouds induced by RPS. The observed young star clusters immediately upstream of the residual dust clouds in the galaxy suggest enhanced SF activity triggered by RPS. Such galaxies are important for studies of the evolution of the removed gas.

Figure 1.6 from Jáchym et al. (2019) shows the jellyfish galaxy, ESO 137-001, another interesting galaxy in the Norma cluster. The tail reveals regions of SF activity induced by RPS, varying degrees of correlation between the CO and Hα emissions, and regions of young stars in the narrow central regions of the multi-phase gaseous tail. The map also reveals the head-tail morphology and compact clumps of gas closer to the galaxy.

Banfield et al. (2013) mapped the ICM in the Norma cluster to search for HI absorption and study the polarised emission from cluster members. Skelton et al. (2010) surveyed the Norma cluster in the near-infrared (NIR) with the SIRIUS survey. Nishino et al. (2012) observed the Norma cluster core with the Suzaku X-ray satellite observatory and found a cool region in the ICM. Mutabazi (2021a) studied the peculiar velocities in the

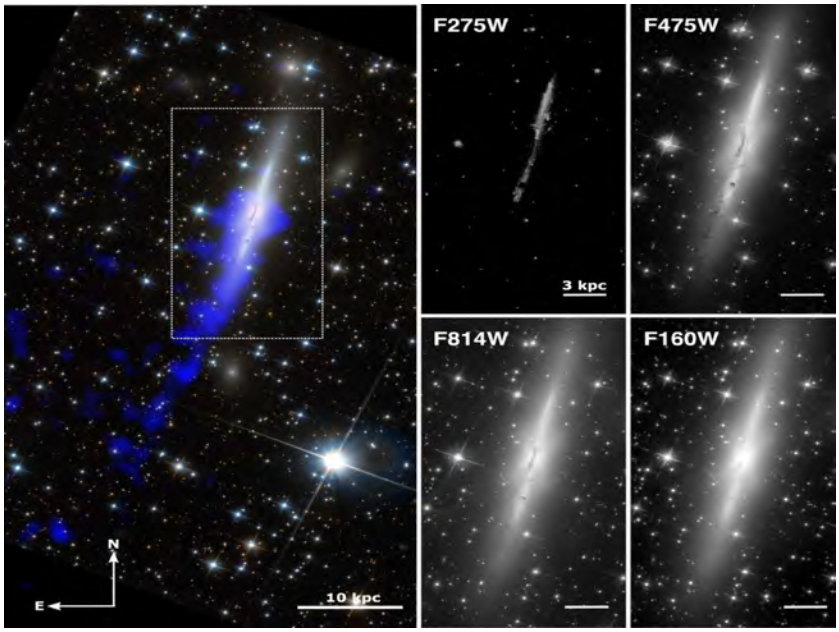

Figure 1.5: An example of a galaxy undergoing a morphological transformation in the Norma cluster. The illustration shows a composite image of ESO 137-002 with the HST F475W/F814W data overlaid with $0.6 - 2$ keV X-ray emission from Chandra in blue to show the X-ray tail (Zhang et al. 2013; Laudari et al. 2022). The galaxy region inside the dotted white box (left panel) is mapped in the four HST bands (right panel). The panel on the right is a close-up view of ESO 137-002 in the four HST bands. The panels illustrate stripping, asymmetric dust clouds, and dust filaments.

Norma cluster based on J- and K_s-band photometry analysis using the 1.4 m IR Survey Facility (IRSF) at the South African Astronomical Observatory[6]. The authors showed that the Norma cluster peculiar velocity is 44 km/s, although the GA itself has a mean positive peculiar velocity of $\sim$ 600 km/s (e.g., Raychaudhury 1989; Mathewson et al. 1992; Tonry 1996).

These are some of the most prominent observations conducted to study kinematic properties, morphological transformation, and SF activity in the Norma cluster's massive and highly dynamic environment.

Studies of the HI emission in the Norma cluster have only been limited to pointed radio observations with the Australian Telescope Compact Array (ATCA[7]: Wilson et al. 2011). These data have an HI flux density sensitivity of 20 mJy/beam, i.e., which results in a

[6]https://irsf2016.saao.ac.za/
[7]https://www.narrabri.atnf.csiro.au/

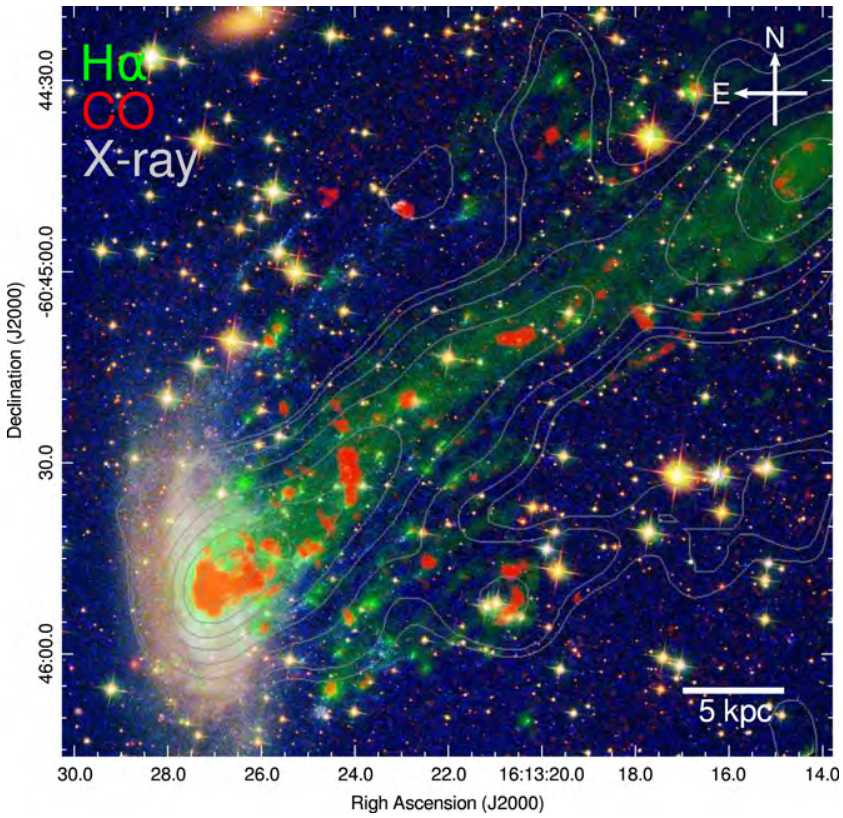

Figure 1.6: The multi-wavelength map of the jellyfish galaxy ESO 137-001 from Jáchym et al. (2019). The cold, dense CO emission was traced with ALMA and the superimposed Hα emission from MUSE and the HST images, while the X-ray contours were added from Sun et al. (2010). The image displays the inner half of the X-ray tail.

total upper limit of HI mass of about 2×10^9 $M_\odot$ at the 5σ noise level for a 50 km/s linewidth per 30″ beam. With this beam the ATCA HI data only reached column density sensitivity levels of $N_{HI} = 3.7 \times 10^{21}$ cm^2. Hardly any diffuse extraplanar HI gas exists in nature at such high N_{HI}. This made these ATCA observations impractical to detect and resolve the HI gas.

To complete the multi-wavelength (optical and X-ray) observation of the Norma cluster, we use deeper HI data from MeerKAT. The primary motivation for observing the Norma cluster galaxies in HI is that it can be used as a probe of the large-scale structures (e.g., Battye et al. 2004; Pritchard & Loeb 2012) since HI is the gas reservoir fed into molecular clouds where SF activity is observed to occur. Therefore, the amount of HI supply may ultimately set the rate of SF. The second motivation for using HI line emission to map gas disks in the Norma galaxy cluster is that the cluster is located behind the galactic plane (GP) of the MW galaxy where there is obscuration due to large clouds of interstellar

cosmic dust. The HI emission line has properties that make it useful to detect gas-rich galaxies behind the MW since dust is transparent at this long radio wavelength.

Throughout this work, we adopt the Hubble constant $H_0 = 70.5$ km/s/Mpc.

Chapter 2

Data Sample & Analysis

2.1 Observations and data reduction

To detect and map HI sources in the Norma cluster, we used high-resolution and deep L-band observations from MeerKAT, which is a precursor to the Square Kilometre Array (SKA) telescope. It is located in the Karoo region of the Northern Cape Province in South Africa. The South African government has put legislation in place that strictly reserves the location for radio astronomy observations in the frequency band from 100 MHz to 2170 MHz and maintains low human population density, thus significantly reducing radio frequency interference[1] (Booth et al. 2009; Booth & Jonas 2012; Jarvis 2012).

MeerKAT is the most sensitive decimetre-wavelength radio interferometer array in the southern hemisphere (Jonas & MeerKAT Team 2016). It has 64 inter-linked antennas, which are positioned on a steerable pedestal, each one equipped with a main paraboloidal reflector with a projected diameter of 13.5 m plus a sub-reflector with a diameter of 3.8 m and a V/H dual-polarisation single-pixel receiver. Three radio receivers and associated digitizers are mounted on a rotating support structure that allows the appropriate receiver to be automatically moved into the antenna focus position (Theron et al. 2012).

The receiver can either be in one of the three bands of the radio spectrum, namely UHF ($0.58 - 1.015$ GHz), L ($0.9 - 1.67$ GHz), and S ($1.75 - 3.5$ GHz). The main function of the receiver is to capture EM radiation and convert it to a voltage signal that is then amplified by cryogenic receivers that add very little noise to the signal. The three

[1] https://www.gov.za/sites/default/files/gcis_document/201409/37397gen141-1.pdf

digitizers mounted on the indexer will then convert the radio frequency voltage signal (RFVS) from the receiver into digital signals using the analogue to digital converter (ADC) (Theron et al. 2012).

The mean measured system equivalent flux density (SEFD) for a single MeerKAT dish at the L-band ($881-1670$ MHz) with a system temperature of $T_{sys} \approx 20$ K, is about 388 Jy (Geyer et al. 2021)[2][3]. The antennas are set below the focal point so that each dish has an offset Gregorian configuration resulting in a sensitivity between 300 and 400 m^2/K, in the frequency range $0.9-1.67$ GHz (Booth et al. 2009; Booth et al. 2009; Jarvis 2012; Theron et al. 2012; Mauch et al. 2020). The key advantage of the Gregorian optical configuration for the MeerKAT antennas is lower T_{sys}, unblocked aperture, and higher sensitivity, while the low far side-lobes improve immunity to radio frequency interference (RFI) (Jonas & MeerKAT Team 2016). With this configuration, the EM waves from cosmic radio sources bounce off the main reflector, project onto the sub-reflector, and thereafter focus onto the feed horn on the receiver (Theron et al. 2012).

MeerKAT has a dense inner core containing 48 antennas (75%) spanning 1 km diameter and distributed in a two-dimensional fashion with a Gaussian uv-distribution, and a mean dispersion of 300 m, a shortest baseline of 29 m, and a longest baseline of 1 km. The other 16 are set out to a radius of 4 km, also distributed in a two-dimensional Gaussian distribution with a mean dispersion of 2500 m, and the longest baseline of 8 km, giving a maximum baseline of 8 km (Theron et al. 2012).

The data is then sent to the correlator through buried fibre optic cables for processing, such as correlation to combine all the antennas' signals to form an image of the observed sky field (Theron et al. 2012). MeerKAT data engineers and scientists then conduct further data reduction and imaging. Table 2.1 summarises some of MeerKAT's specialized structural components. Figure 2.1 shows the distribution of the 64 MeerKAT antennas at the Karoo in panels (a) and (b) and key structural components of a single antenna of the MeerKAT array telescope in panel (c).

The Norma cluster was observed with the MeerKAT telescope in the L-band, and the HI datacube was obtained after data reduction was conducted using the CARAcal pipeline[4] (Józsa et al. 2020). The resulting datacube for this project is in the frequency range of

[2]https://science.ska.ac.za/meerkat

[3]https://skaafrica.atlassian.net/servicedesk/customer/portal/1/article/277315585

[4]https://caracal.readthedocs.io/en/latest/index.html

$1372 - 1417$ MHz and is sampled with 243 spectral channels, each one 187 kHz in width (44.1 km/s) in full polarization, thus covering a velocity range of $483 - 11,113$ km/s. The field of view is about $2^\circ \times 2^\circ$ with a pixel scale of $2''$. The rms noise level in the datacube is $\sigma = 0.09$ mJy/beam with a beam size of $\sim 14.65'' \times 9.28''$ and position angle of PA $\sim 146^\circ$. The properties of this HI datacube allows the HI mass detection limit of $M_{HI,lim} = 7.25 \times 10^7$ $M_\odot$ at the 5σ noise level, assuming a linewidth of 200 km/s. The HI channel maps of the datacube are included in the atlas (Figure A.1). Further details regarding the data reduction process can be found in Ramatsoku et al. (2020).

2.2 Source finding

To detect HI line emission in the datacube, the Source Finding Application (SoFiA[5]) was used. SoFiA is a flexible software application for the detection and parameterization of sources in HI datacubes (Serra et al. 2015; Westmeier et al. 2021). It uniquely combines source-finding and parameterization algorithms to search for line emission and produces moment maps, cut-out datacubes, and a catalogue of source parameters for the detections (Serra et al. 2015). The network of SoFiA parameters includes noise measurements along the frequency axis, source finding using smooth and clip (S+C) algorithms, merging of detected voxels into sources, calculation of reliability (and removal of unreliable sources), source parametrization with the Fit Busy Function, creation of output products, and catalogues (Serra et al. 2015; Westmeier et al. 2021).

The datacube was smoothed spatially and spectrally using smoothing kernels. We used the "Smooth+Clip Finder" method for source finding at the noise threshold of 4σ. This combination proved to be the best for source finding (Serra et al. 2015). Sources are created when pixels are merged. For the pixel value assumed by the smoothing algorithm in "Edge mode" (outside the boundaries of the datacube), we opted for "constant", which assumes the value of 0. For the statistics used to determine the noise in the datacube ("RMS mode"), we selected "median absolute deviation". Reliability calculations in the "Parametrisation" module were also carried out, for which sources were discarded if they were below the threshold value of 0.9. Any more would produce fewer reliable sources

[5]https://github.com/SoFiA-Admin/SoFiA-2

Telescope Name	MeerKAT Array Telescope
Location	Northern Cape, South Africa
Project Funders and Organisers	South African National Research Foundation (NRF) and/or South African Radio Astronomy Observatory (SARAO)
Number of Dishes	64
Configuration	Offset Gregorian
Emission line frequency	Radio
Main Reflector Diameter	13.5 m
Sub-Reflector Diameter	3.8 m
Collecting Area	$9,000$ m^2
Surface Accuracy Diameter	0.6 mm RMS
Receivers	4 positions for cryogenic receivers with associated digitizers
Reflector Noise Contribution	< 1 K
Height	19.5 m
Weight	42 tons
Aperture Phase Efficiency	0.91 at 14.5 GHz
Frequency Bands	$0.58 - 1.015$ GHz $1 - 1.75$ GHz $8 - 14.5$ GHz
Sensitivity L-band ($0.9 - 1.67$ GHz)	220 m^2/K required (> 300 m^2/K achievable)
Continuum Imaging Dynamic Range at 1.4 GHz	60 dB
Minimum Baseline	29 m
Maximum Baseline	8 km

Table 2.1: Summary of the MeerKAT array interferometer

and miss other sources well above the noise distribution, and vice versa. The full SoFiA parameters used for source detection in this work are presented in Appendix A.2.

SoFiA pipeline detected 31 HI sources spanning a velocity range of $v_{rad} \sim 604 - 10,353$

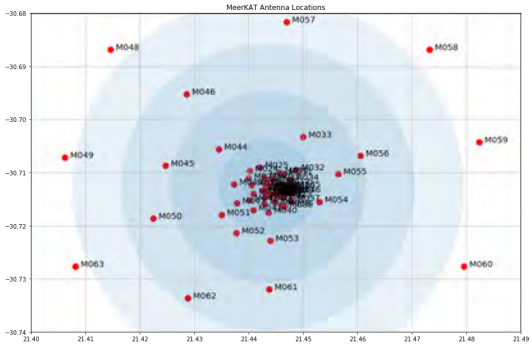

(a) Layout of 64 antennas in coloured rings of 1, 2, 4, 6, 8 km from the core.

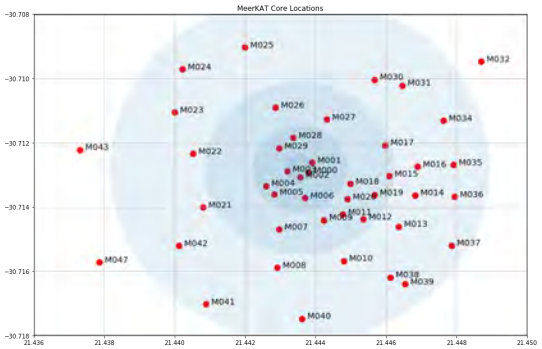

(b) Layout of core antennas in coloured rings of 50, 100, 300, 600 m from the centre.

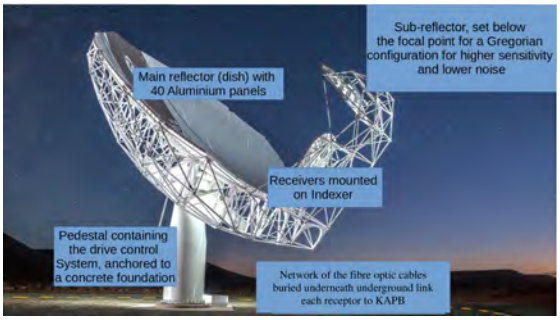

(c) The MeerKAT antenna configuration (image obtained from sarao.ac.za).

Figure 2.1: The MeerKAT array telescope in the Karoo location. Figures in panels (a) and (b) are schematic presentations of the distribution of 64 antennas on location, annotated by antenna number from the centre to the outskirts, in a Gaussian distribution (Jonas 2009; Booth & Jonas 2012). In panel (a), 30% of the antennas are distributed outside the core, and in panel (b) 70% are positioned within the dense inner core. Panel (c) is a MeerKAT antenna, annotated to illustrate some of its key structural components, including the main reflector, sub-reflector, receivers, and connecting structures.

km/s. A careful inspection of all the detections was conducted by eye, and a total of 6 sources were found to be unreliable based on their spectra. This resulted in a total of 25 HI sources detected within the volume of the Norma cluster datacube.

2.2.1 Completeness and reliability of detected sources

To assess the completeness and reliability of source-finding tasks completed with the SoFiA pipeline, we first assess completeness using the cumulative galaxy counts, as illustrated in Figure 2.2. We define the completeness HI mass of the Norma clus-

ter HI galaxy sample as the point where the cumulative galaxy distribution plateaus (Kochanek et al. 2001). Employing this technique, we determine that the distribution flattens at $\log(M_{HI}/M_\odot) \approx 9.4$. The source detection process is 80% complete for $\log(M_{HI}/M_\odot) \lesssim 9.0$, and 100% complete for $\log(M_{HI}/M_\odot) \lesssim 9.4$.

Second, one of the essential parameters derived from source-finding efforts is the integrated flux. SoFiA-2 computes this flux by summing the flux density values within the source mask, then multiplying by the spectral channel width and dividing by the beam solid angle. Moreover, SoFiA-2 calculates the statistical uncertainty of the integrated flux using Gaussian error propagation and accounting for pixel correlations due to the finite beam size. The local noise level surrounding each detection is assessed to facilitate this calculation. The investigation by Westmeier et al. (2021) delves into SoFiA-2's flux recovery process. They identify a specific aspect of the S+C finder that introduces a systematic effect. This arises at the outset of each iteration, where pixels previously detected are assigned $\pm$n times the noise level within the data cube. This pre-smoothing treatment preserves the original flux value sign, curbing emission extension beyond source limits. However, an unintended outcome emerges: the source mask grows in directions where noise-driven contributions are predominantly positive, creating a net positive flux bias. The magnitude of this bias is linked to the "n" replacement value. Defaulting to $n = 2$ introduces a $2 - 3\%$ positive flux bias. Modifying n to 1.5 eradicates the bias, although at the expense of a slightly stronger negative bias for faint sources. A statistical correction is advised for flux measurements with higher accuracy ($< 3\%$) to counteract the bias.

In Fig. 8 of the paper, the authors illustrate a histogram portraying the ratio of flux measurement error to uncertainty from SoFiA-2. This histogram is compared to an ideal Gaussian distribution with expected properties. The fitted histogram aligns closely with theoretical expectations: centroid at 0.27 ± 0.02 and standard deviation of 1.22 ± 0.02. This correspondence underscores the accuracy of flux uncertainties reported by SoFiA-2. Minor deviations and distribution broadening are attributed to the flux bias, influenced by signal-to-noise ratio (SNR) variations. Thus, Westmeier et al. (2021) confirm that reported flux uncertainties in SoFiA-2 remain accurate despite slight variations due to the flux bias and signal-to-noise ratio.

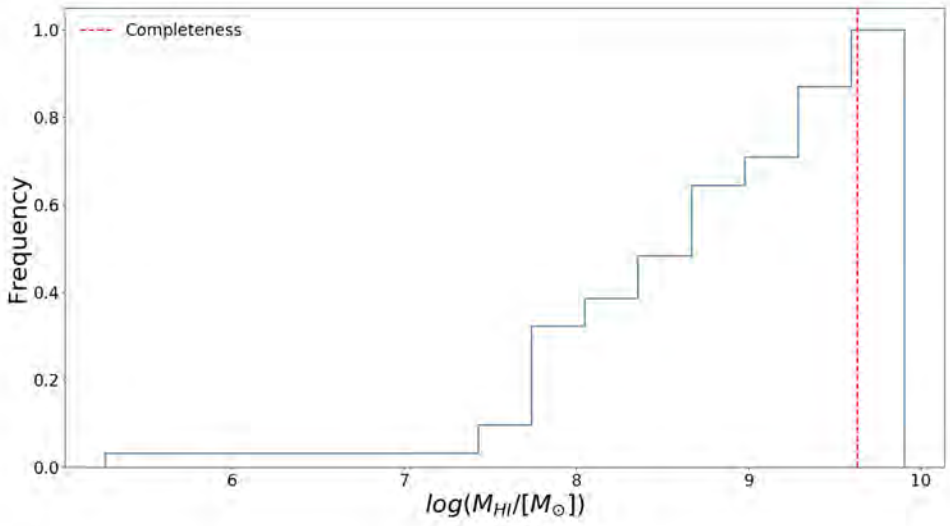

Figure 2.2: The cumulative distribution of galaxy counts as a function of HI mass. The black vertical line denotes the estimated completeness mass limit for the observed masses of all the detected HI galaxies.

2.3 HI data products

SoFiA products include moment maps and catalogues containing information about the detected sources' radial velocity, flux density, and spatial properties. We can compute from these other parameters, such as HI masses, find counterparts in other wavelengths, and quantify the degree of asymmetry in the HI gas disks.

We use the radio radial velocity definition where SoFiA computes velocities of the detected HI galaxies, and velocities of their optical counterpart from the Woudt et al. (2007) catalogue are converted to radio radial velocities using the equations;

$$\frac{\mathrm{v_{opt}}}{c} = \frac{\mathrm{f_0}}{\mathrm{f}} - 1 = z, \tag{2.3.1}$$

and

$$\frac{\mathrm{v_{rad}}}{c} = 1 - \frac{\mathrm{f}}{\mathrm{f_0}} = \frac{z}{1+z}, \tag{2.3.2}$$

so that

$$\mathrm{v_{rad}} = \frac{c \times \mathrm{v_{opt}}}{c + \mathrm{v_{opt}}}. \tag{2.3.3}$$

The HI mass was computed using;

$$\frac{\mathrm{M_{HI}}}{[\mathrm{M_\odot}]} = 2.36 \times 10^5 \times \left(\frac{\mathrm{D}}{[\mathrm{Mpc}]}\right)^2 \int \frac{\mathrm{S_v}}{[\mathrm{Jy}]} \frac{\mathrm{dv}}{[\mathrm{km/s}]}, \tag{2.3.4}$$

where dv is the channel width, and D is the distance to the source calculated using Hubble's law;

$$v = H_0 D, \tag{2.3.5}$$

where $H_0 = 70$ km/s/Mpc.

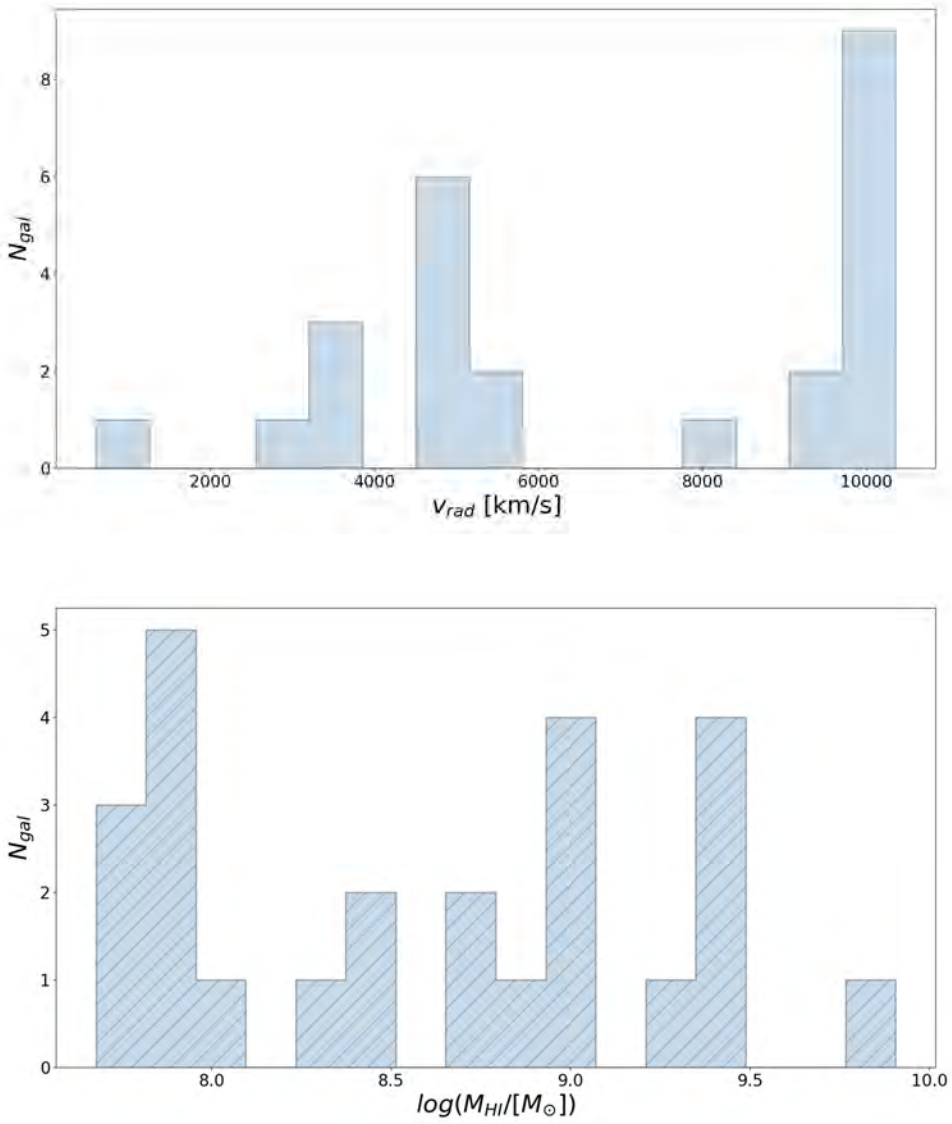

Figure 2.3: Global HI properties of the detected galaxies. The top and bottom panels in the figure show the radial velocity and HI mass distributions of the detected galaxies, respectively.

This study determines the distances to the HI detections without accounting for their random motions. This choice is based on the findings of Mutabazi (2021b), which reported a peculiar motion of the Norma cluster as 44 ± 151 km/s, suggesting consistency

with zero so that random motions of galaxies are not significant and therefore would not affect the results obtained. This suggests that the higher-velocity group comprises background galaxies within a distinct gravitational potential. To investigate global HI properties of the detected galaxies, we present the radial velocity and HI mass distributions in Figure 2.3. The velocity distribution on the top panel reveals a compact population of 11 sources at $v_{rad} \sim 10,000$ km/s and another source at $v_{rad} \sim 604$ km/s. The majority of the detected sources lie within the velocity range of $v_{rad} \sim 2000 - 8000$ km/s peaking at a velocity of $v_{rad} \sim 4870$ km/s which is where the Norma cluster is located.

The M_{HI} distribution in the bottom panel shows all detections have a wide range of masses covering the range of $\log(M_{HI}/M_{\odot}) \sim 7.5 - 9.9$, with an average HI mass of $\log(M_{HI}/M_{\odot}) \sim 8.3$.

In the bottom panel of Figure 2.5 we show M_{HI} as a function of v_{rad}. About 77% of the detections within the Norma cluster velocity range ($\sim 2000 - 8000$ km/s) have low M_{HI} (within the range $\log(M_{HI}/M_{\odot}) \sim 7.5 - 8.5$), with only 3 detections exhibiting higher M_{HI}. Those galaxies belonging to the compact substructure in the background are massive with $\log(M_{HI}/M_{\odot}) \sim 8.4 - 9.9$. This is possibly due to the detection limit of our data. We examine this effect in Figure 2.4, which shows the detection limit assuming a 5σ detection of a typical dwarf galaxy with a linewidth of 45 km/s (red curve) and a massive galaxy with a linewidth of 300 km/s (blue curve). The curves retain a steeper slope at < 2000 km/s and are slightly less pronounced after that, indicating that most massive galaxies were detected at velocities of $\sim 8000 - 11,000$ km/s.

2.3.1 Galaxy linewidths

The rotational motion of a galaxy around its axis is observed while half of the galaxy plane is approaching and the other half is moving away from the observer. This creates a spectral distribution with two "horns" for a typical spiral galaxy, depending on the inclination of the rotating galaxy gas disk. The rotation is nearly constant across the "horns", causing Doppler shift within the galaxy to broaden the line.

Spectral intensity profiles (21 cm linewidths) are a proxy for galaxy rotational speed, internal kinematics, and parameters from which gas disk size and morphology can be mapped (Verheijen 2001; Yegorova & Salucci 2007; Stewart et al. 2014). The HI full

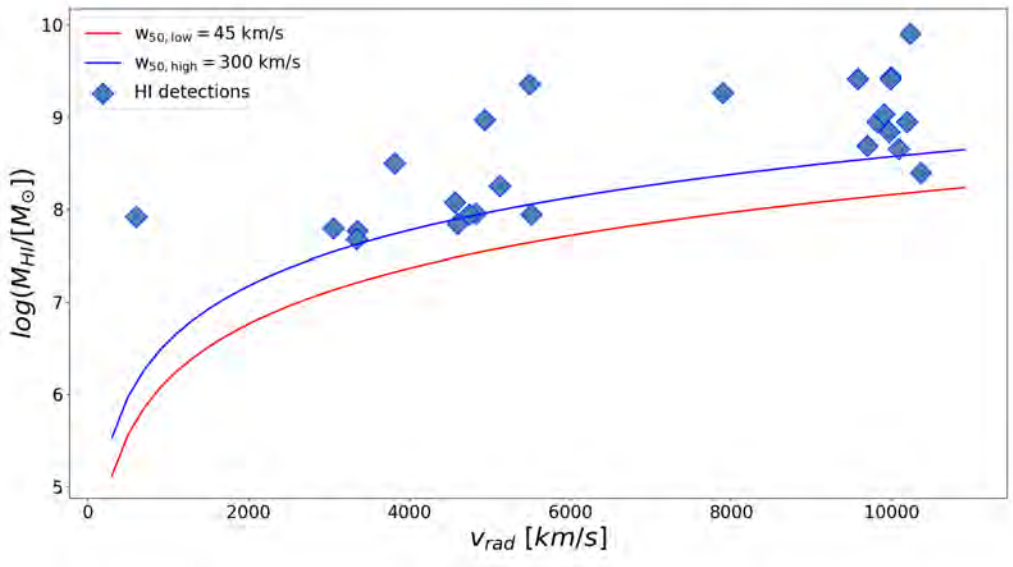

Figure 2.4: The HI mass limit as a function of velocity at 5σ. The red curve represents the mass limit for a galaxy with a linewidth of 45 km/s, while the blue line represents the mass limit for a galaxy detection with a linewidth of 300 km/s. The steelblue diamond markers are the HI detections.

width at half maximum (FWHM) of a galaxy's spectral profile is typically measured at 50% (w_{50}) and 20% (w_{20}) of the maximum. For this work, we only use the w_{50} which we corrected for inclination ($w_{50,corr}$) using;

$$w_{50,corr} \approx w_{50}/\sin(i). \tag{2.3.6}$$

The inclination angle, i, is approximated by $\cos(i) \approx \frac{b}{a}$, where b and a are the minor and major axis, respectively. Typically, linewidths of "normal" rotating spiral galaxies are in the range of $\sim 200 - 300$ km/s, and deviations from this may be due to a set of parameters including mass, size, and/or external interactions (e.g., McGaugh 2012; Ogle et al. 2019).

We present the distribution of $w_{50,corr}$ for the detected galaxies in Figure 2.6. First, the figure shows a skew distribution in the range $\sim 66 - 392$ km/s with a linewidth mean of ~ 203.4 km/s. We note that although some ellipticals are known to have HI disks embedded within the dark matter halo of the galaxy and settled into an equilibrium configuration, the gas disk is often kinematically decoupled from the stellar disk and

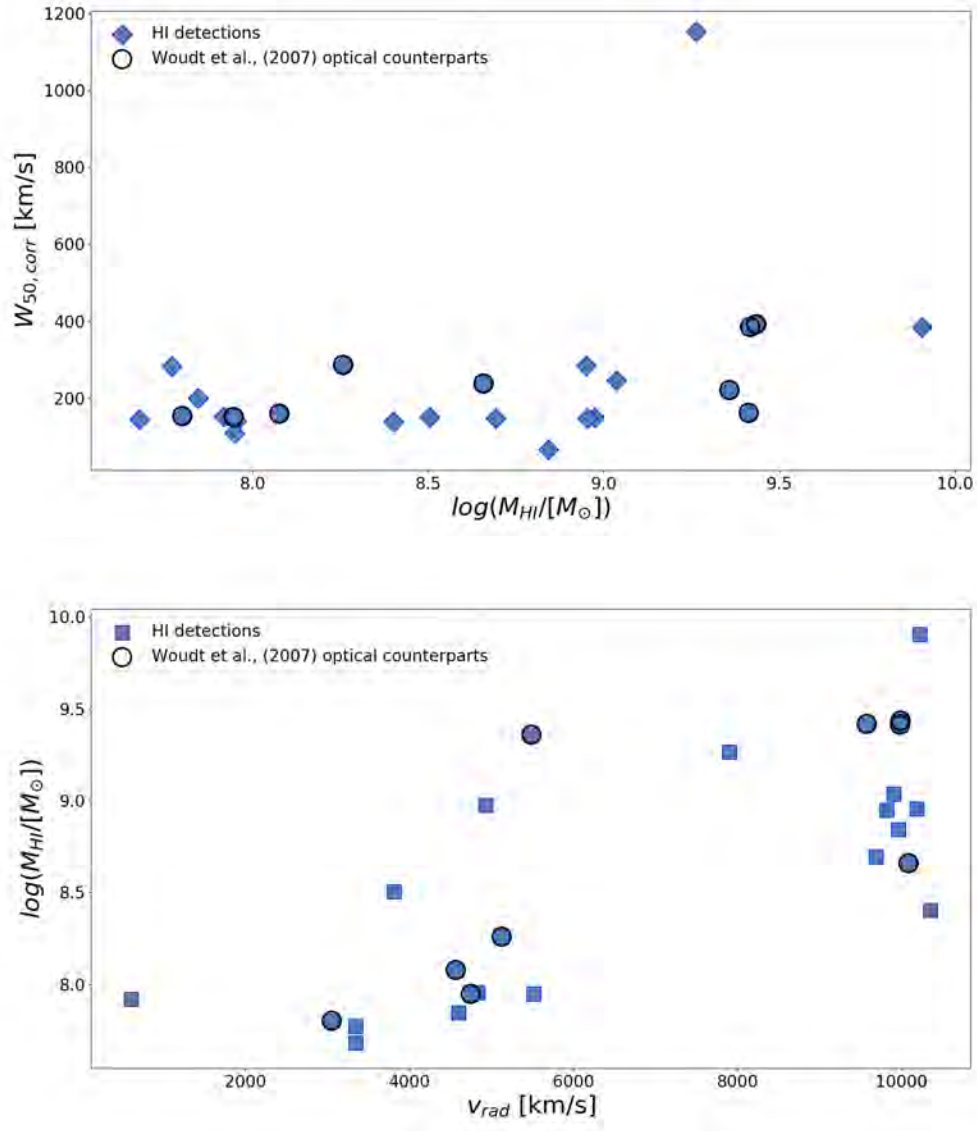

Figure 2.5: The distribution of galaxies with and without optical counterparts in Woudt et al. (2007) catalogue. The top panel shows linewidth as a function of HI mass, and the bottom panel is the HI mass as a velocity function. HI detections with optical counterparts from Woudt et al. (2007) catalogues are indicated with black circle markers.

massive ellipticals may have rapidly rotating HI components even though many ellipticals are slow rotators in the stellar component (e.g., Raimond et al. 1981; Van Gorkom et al. 1986; Lake et al. 1987; Kim et al. 1988; Schweizer et al. 1989; Van Gorkom et al. 1990; Lees et al. 1991; Bertola et al. 1993; Schiminovich et al. 1995, 1997). However, there is an observed correlation between morphology and linewidth. About 78% of ellipticals (E5,

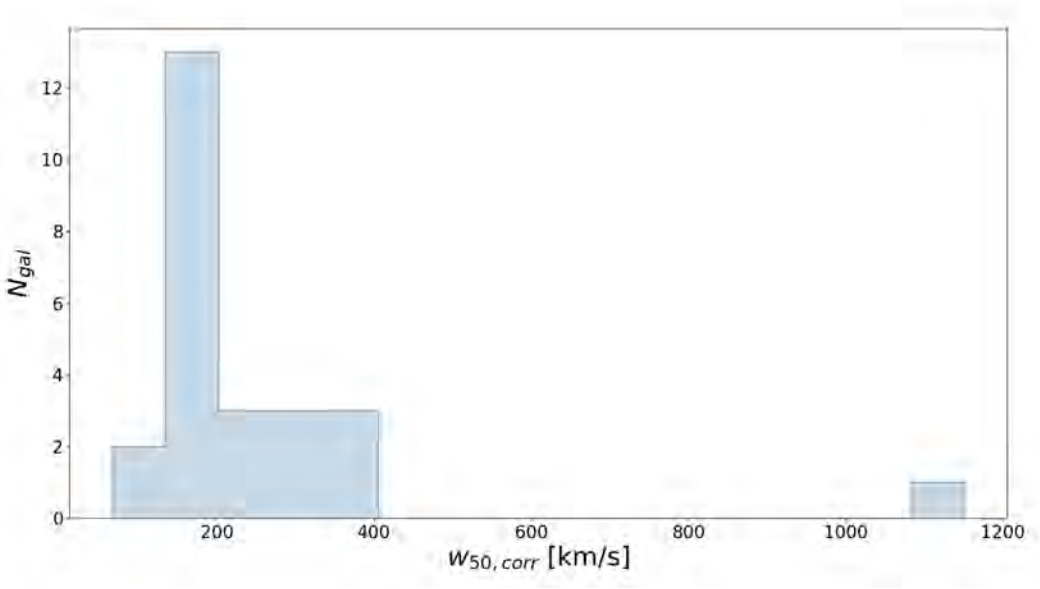

Figure 2.6: The linewidth distribution of all the galaxies detected in HI.

E) have narrow linewidths ($w_{50,corr} \sim 66 - 161$ km/s; McGaugh 2012; Ogle et al. 2019), while all the spirals exhibit the widest linewidths ($w_{50,corr} \sim 240 - 392$ km/s; McGaugh 2012; Ogle et al. 2019) and higher masses in the range $\log(M_{HI}/M_{\odot}) \sim 7.8 - 9.5$. The lenticulars (S0 and SA0) have linewidths in the range $w_{50,corr} \sim 153 - 199$ km/s, and the irregulars and peculiars (Irr, Pec) have linewidths in the range $w_{50,corr} \sim 147 - 237$ km/s.

For galaxies with confirmed optical counterparts, most of them have normal linewidths (e.g., McGaugh 2012; Ogle et al. 2019) with linewidth mean of 213.62 km/s, in the range $w_{50,corr} = 138.47 - 391.51$ km/s, and $w_{50,corr,\delta} = 89$ km/s.

The outlier with $w_{50,corr} \sim 1151$ km/s has high mass and the most perturbed gas disk morphology in the sample (section 2.6). This wide linewidth was observed for the active, hyperluminous galaxy, SMM02399-0136 (Ivison et al. 1998), although in this case, it is more likely that the wide $w_{50,corr}$ is due to the noise seen in the galaxy's spectral profile. At the same time, the signal appears with a very low peak.

In total, about 84% of detections have $w_{50,corr}$ expected for "normal" galaxies. It is worth mentioning that by examining the sizes of the HI disks in relation to the optical in panel A in Figure 2.19 and HI linewidth, we find that most galaxies within the Norma cluster have slightly equal disk sizes with the optical (i.e., truncated disk),

e.g., (1) J160906.49-610923.7, (10) J161157.16-610749.8, (15) J161326.06-604539.2, (17) J161459.10-604603.5, (21) J161627.69-611421.3. This indicates that the observed linewidths may reveal the degrees of disk truncation in our HI sample.

2.4 Optical counterparts

The spectroscopic optical studies of galaxies in the Norma cluster were conducted by Woudt et al. (2007) with the Anglo-Australian Observatory 2dF Facility[6] (Lewis 2002). They catalogued 182 optical galaxies in the Norma cluster field within the Abell radius $R_A = 2.02$ Mpc, in the velocity range of $v_{rad} \sim 3022 - 63,770$ km/s. To obtain more information on the HI detected galaxies, we searched for optical counterparts from the catalogue for each galaxy detected in HI. To find maps of the optical counterparts we used imaging conducted with MeerLICHT telescope[7] (de Wet et al. 2021). MeerLICHT images were searched in all the observed bands, g, i, q, r, u and z bands.

The Norma cluster is more visible at X-ray, HI and IR wavelengths than the optical. It is a complicated task to search for optical galaxies in the field due to the location of the cluster, which is crowded by stellar objects in the MW and suffers from dust extinction. As a result, most optical galaxies appear faint, except for cD galaxies with higher surface brightness and some giant ellipticals around the central regions.

The optical sky area covered has foreground extinction that goes up to A = 0.242 mag in the B-band (Woudt et al. 2007). We searched for optical counterparts from Woudt et al. (2007) catalogue by considering their 2D on-sky position and v_{rad}. Candidates that are concentric with the HI position, with a velocity difference of < 200 km/s, are considered likely counterparts. We use a velocity window consistent with that of Woudt et al. (2007), which showed a difference of up to 200 km/s between their redshift detections and previous studies (Woudt et al. 2007). We then verified the candidates through visual inspection by overlaying their positions on the optical images from MeerLICHT. Of the 25 HI detections, 12 ($\sim 48\%$) were found to have optical counterparts from both Woudt et al. (2007) catalogue and MeerLICHT images, with an average velocity offset of $v_{rad} \sim 78$ km/s, and a concentric position with the HI detection. A further 9 ($\sim 36\%$) candidates were found to have optical counterparts in MeerLICHT, but not in Woudt

[6] https://aat.anu.edu.au/front

[7] http://www.meerlicht.uct.ac.za/mt/project

et al. (2007) catalogue.

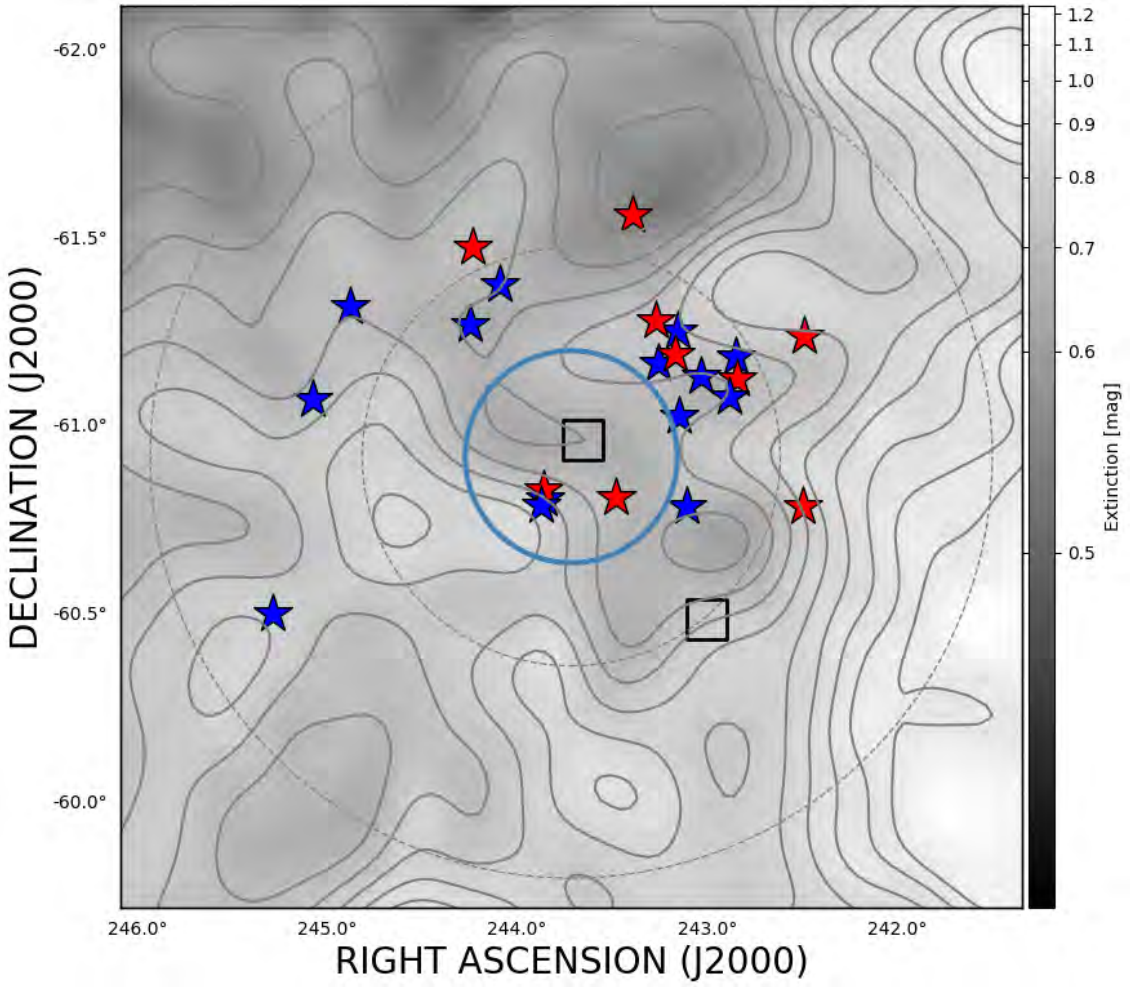

Figure 2.7: The spatial distribution of HI detections. The detected HI gas disks are superimposed on a DIRBE/IRAS map of A_g galactic extinction values in the optical g-band, ranging from 0.5 to 1.2 mag as shown on the scale bar. Dust extinction contour levels are set between 0 and 1 mag in ~ 0.042 mag intervals. HI detections with optical counterparts from both Woudt et al. (2007) catalogue and MeerLICHT images are indicated with blue star markers, and HI detections with optical counterparts inspected from MeerLICHT are indicated with red star markers. HI detections without optical counterparts are indicated with black-edge square-box markers. The blue circle represents the core of the Norma cluster within a radius of 0.34 Mpc from the centre, and the grey circles indicate $1/3 \times R_A$ and $2/3 \times R_A$ radii, respectively.

In Figure 2.7, 25 verified HI detections are overlaid on the g-band galactic extinction

map (A_g) made from E(B − V) colour reddening measurement (DIRBE/IRAS[8]; Schlegel et al. 1998). Within the MeerLICHT g-band field of view, the galactic extinction value is $R_\lambda = 3.269$ mag (Yuan et al. 2013). The extinction law states that;

$$A_\lambda = R_\lambda \times E(B-V), \tag{2.4.1}$$

where R_λ is the extinction in a given band. E(B − V) is the colour reddening from Schlegel et al. (1998). Thus the derived extinction is;

$$A_g = 3.269 \times E(B-V). \tag{2.4.2}$$

Foreground extinction increases towards the East side of Figure 2.7 (0.6 − 1.2 mag) and is less severe towards the South ($\sim 0.5 - 0.6$ mag). Furthermore, comparing the results in this work (A_g) with results from Woudt et al. (2007) (A_B), and based on the population density of optical galaxies, which is the highest in the central regions, it is more likely to match HI candidates with optical counterparts within the central regions, because, as shown in Figure 2.7 and Figures 2 & 3 in Woudt et al. (2007), the sky area of focus is located where $A_B = 0.242 \times E(B-V)$, which is three times lower than the extinction towards the galactic belt. However, the severity is even less within a field radius of 1.35 Mpc (this work).

We found that all 2 detections without optical counterparts in both Woudt et al. (2007) and MeerLICHT catalogues are located in regions of high foreground extinction (> 0.6 mag). Furthermore, most of the 12 galaxies with optical images in MeerLICHT but no counterpart in Woudt et al. (2007) may have been missed in earlier works since their faint, blurry MeerLICHT images are almost imperceptible.

To investigate HI properties that may have affected the optical counterpart recovery rate, we look at M_{HI} and $w_{50,corr}$ of galaxies with optical counterparts (Woudt et al. 2007 catalogue and/or MeerLICHT) in comparison with galaxies without. In Figure 2.5, on the top panel, galaxies $w_{50,corr}$ are plotted as a function of M_{HI}. We find that for the gas disk with the highest $w_{50,corr}$ and 2 with the lowest $w_{50,corr}$, no counterpart was found. On the bottom panel, we show the plot of M_{HI} as a function of v_{rad}, in which 11 of the detections within $v_{rad} \sim 604 - 8000$ km/s have optical counterparts while all but 1 detections at $v_{rad} \sim 10,000$ km/s does not have an optical counterpart. However,

[8] https://irsa.ipac.caltech.edu/cgi-bin/bgTools/nph-bgExec, and https://irsa.ipac.caltech.edu/cgi-bin/bgTools/nph-bgExec

there are slightly more foreground sources with optical counterparts in Woudt et al. (2007) catalogue than in the background, possibly due to the ZoA obscurities. As such, the inclusion of MeerLICHT images roughly completes the optical data.

Optical counterparts for HI detections in regions of high extinction (mostly towards the East regions in Figure 2.7) are missed, which makes galaxies with low surface brightness undetectable in optical wavelengths. Some of these detections at greater distances are high-mass gas disks (Figure 2.4, in Section 2.3), and it is possible they could be young galaxies with low surface brightness in the optical or were too far to be seen at optical wavelengths.

2.5 HI Morphologies

The physical parameters of a galaxy are associated closely with its morphology, and disturbed or asymmetrical gas disks can provide clues for historical events of interactions and/or intrinsic dynamical activities of galaxies. In this work, the HI morphologies of the detected gas disks are quantified using the asymmetry parameter, A_p, which is defined as the degree of rotational asymmetry around the centre of the galaxy (Abraham et al. 1994; Conselice et al. 2000; Holwerda et al. 2011; Lelli et al. 2014). The parameter was introduced for optical studies of nearby galaxies (e.g., Abraham et al. 1994) and modified for HI gas disks (e.g., Conselice 1997; Conselice et al. 2000; Conselice 2003a; Holwerda et al. 2011). In this work, an adaptation of the asymmetry parameter from Conselice (2003b) is used and is defined as;

$$A_p = \frac{\Sigma_{i,j}|I(i,j) - I_{180}(i,j)|}{\Sigma_{i,j}|I(i,j)|}, \tag{2.5.1}$$

where $I(i,j)$ and $I_{180}(i,j)$ are the integrated fluxes at the index point (i,j) in the original and rotated column density maps, respectively. The formulation normalizes the residuals between the original image and the rotated image to the total flux in the index point (i,j). If equal HI emission is detected on both sides of the gas disk, A_p assumes a minimum value of 0, and if asymmetry is detected on one side of the gas disk, then A_p becomes a maximum value of 1.

Figure 2.8 presents the A_p distribution measured from Equation 2.5.1. A_p results were compared with visual inspections based on moment-0 maps as well as spectral profiles. Gas disks with $A_p \sim 0.6 - 1.0$ were determined to have major asymmetries, and gas

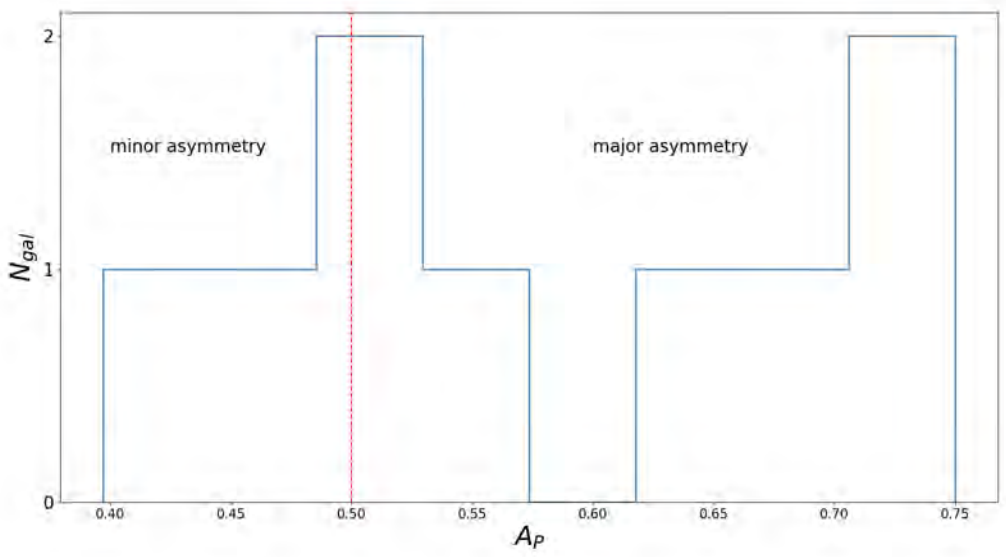

Figure 2.8: The A_p distribution for spatially resolved HI detections. Galaxies whose gas disk morphologies exhibit minor asymmetries have $A_p \sim 0.3 - 05$, while galaxies with major asymmetries in their gas disk morphologies exhibit the asymmetry quantity in the range $A_p \sim 0.5 - 1$.

disks with $A_p \sim 0.3 - 0.4$ have minor asymmetries.

For unresolved galaxies, the A_p parameter could not be used to qualify asymmetries reliably. Therefore, we used the skewness and kurtosis of the spectral profiles to qualify asymmetry in galaxies that are not spatially resolved. While calculating the ratio of total flux on each side of the systemic velocity (V_{sys}) can be somewhat more physics-oriented, we opted for the skewness-kurtosis parameter. This choice is driven by its higher statistical robustness, as it remains unaffected by variations on either side of the profile. Skewness can reveal the presence of a tail ("lopsidedness"), while kurtosis can quantify the intensity of the tail distribution.

Figure 2.9 shows distributions of the skewness (top panel) and kurtosis (bottom panel) in the spectral profiles of the detected galaxies. The distribution of skewness in the spectral profiles of all HI detections on the top panel is presented, with the skewness threshold indicated by the dotted vertical line. Normal symmetrical distributions have a degree of skewness in the range -1 to 1 (Brown 2011). Therefore, a total of 13 detections can be considered to have "normal" distributions. The outlier at skewness > 3 is the noisy detection which was found to feature the highest linewidth and very high HI mass

(section 2.3) at a radial velocity of ~ 7800 km/s. From its HI intensity map, it seems to have a distorted gas disk with a long HI tail. The 2 detections with skewness of 1.06 and 1.07 are only slightly asymmetrical. Other detections were considered slightly asymmetrical for reasons such as skewness quantity based on an absorption even though the spectral profile appears symmetrical; beam size much larger than the intensity map of the gas disk; and spectral profile of the galaxy observed face-on is a double horn symmetrical distribution but has a small lump in one extension of the spiral arm.

On the bottom panel, the kurtosis distribution is presented. A normal univariate distribution is one in which the kurtosis ranges between -2 and 2 (George & Mallery 2010). A total of 9 spectral profiles of the HI detected galaxies have heavy-tailed distributions, and these are the same sources with skewness greater than 1.

In summary, out of all the 25 HI detections in the Norma volume, a total of 9 detections were determined to have lopsided HI morphologies based on the asymmetry parameter. Using the skewness and kurtosis properties of the spectral profiles, a further 4 detections were found to be lopsided. Thus, within the Norma volume, 13 detections are considered asymmetric.

2.6 HI Catalogue & Atlas

2.6.1 HI Catalogue

The HI catalogue of the detected galaxies is presented in Table 2.2. The column entries of the detected galaxies are listed as follows:

- column (1) galaxy ID defined as Jhh:mm:ss-dd:mm:ss, and we use * to indicate galaxies that are spatially resolved;
- columns (2) and (3) are the 2D on-sky celestial coordinates: right ascension (RA [deg]) and declination (Dec [deg]), respectively;
- columns (4) and (5) are the integrated flux density (S_{int} [Jy km/s]) and linewidth corrected for inclination angle ($w_{50,corr}$ [km/s]), respectively;
- columns (6) and (12) are the radial velocities (v_{rad} [km/s]) and Hubble distances to the detected galaxies (D_H [Mpc]), respectively;

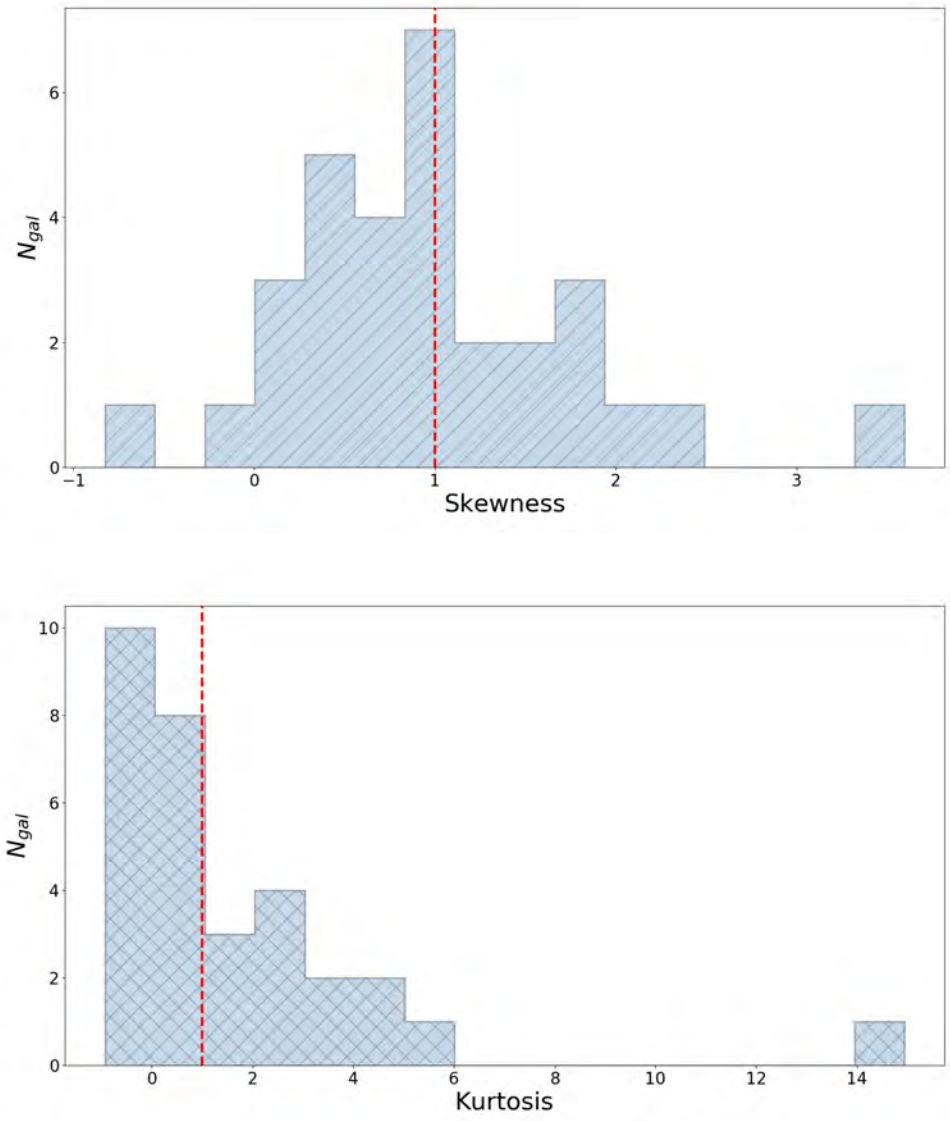

Figure 2.9: The distribution of Skewness (top panel) and Kurtosis (bottom panel) for all HI detections. The vertical lines at Skewness = 1 and Kurtosis = 2 delineate between "normal" distributions (symmetrical mass distribution) on the left and skew/kurtosis distributions (asymmetrical mass distribution) on the right.

- columns (7) and (8) are the minor and major axis ([arcsec]) of the ellipsoid geometry of the sources, respectively;
- column (9) is the galaxy inclination angle ([deg]);
- columns (10) and (11) are the kurtosis and skewness of the HI spectra, respectively;
- column (12) is the HI mass in log-scale ($\log(M_{HI}/[M_{\odot}]$) computed using Equation

2.3;

- column (14) is the asymmetry parameter (A_p) computed using Equation 2.5.1;
- columns (15), (16), (17), (18) and (19) are the WISE approximate morphology, stellar masses ($\log(M_\star/[M_\odot])$), SF rates (SFR) from the mid-IR fluxes at 22 μm (SFR_{22}: $[M_\odot/yr]$), and WISE colours $W1-W2$ and $W2-W3$ ([mag]), respectively;
- column (20) entries are the optical counterparts. The optical velocity of the counterpart is indicated where available.

	Galaxy ID	RA	DEC	S_{int}	$w_{50,corr}$	v_{rad}	Ellipse		$\measuredangle i$	Kurtosis	Skewness	D_H	$\log(M_{HI}/[M_\odot])$	A_p	Morphology	$\log(M_\star/[M_\odot])$	SFR_{22}	W1 − W2	W2 − W3	Optical Counterpart
							Minor Axis	Major Axis												
	(JHH:MM:SS-DD:MM:SS)	(deg)	(deg)	(Jy km/s)	(km/s)	(km/s)	(arcsec)	(arcsec)	(deg)			(Mpc)					($M_\odot$/yr)	(mag)	(mag)	
	(1)	(2)	(3)	(4)	(5)	(6)	(7)	(8)	(9)	(10)	(11)	(12)	(13)	(14)	(15)	(16)	(17)	(18)	(19)	(20)
(1)	J160906.49-610923.7*	242.277	−61.157	0.081	150.621	4748.64	6.91	13.951	1.053	−0.616	0.322	67.838	7.947	0.707	Irr	9.314	0.1089	−0.261	3.511	ZOA-J16091364-6111091 at v_{opt} = 4615.471 km/s
(2)	J160923.81-604220.9*	242.349	−60.706	0.143	286.035	5124.94	12.671	15.264	0.592	0.714	0.817	73.213	8.258	0.496	SBc	9.802	0.8214	0.066	3.696	WKK98-5979 at v_{opt} = 5123.902 km/s
(3)	J161037.92-610647.9*	242.658	−61.113	0.109	282.494	3347.9	9.894	12.689	0.677	0.309	0.622	47.827	7.77	0.75	SABcd	9.183	0.2827	0.168	3.328	MeerLICHT
(4)	J161039.19-610317.7	242.663	−61.055	0.592	384.694	9575.97	21.403	35.855	0.931	0.597	0.874	136.8	9.417	–	E	10.704	0.9456	−0.058	2.75	WKK98-6032 at v_{opt} = 9550.723 km/s
(5)	J161049.62-610031.2	242.707	−61.009	0.192	283.895	9816.97	14.418	16.039	0.454	0.408	1.072	140.242	8.95	–	SA-c-pec	10.198	1.183	0.044	3.625	MeerLICHT
(6)	J161126.51-610412.4	242.86	−61.07	0.109	147.206	9689.74	11.937	14.236	0.576	−0.126	0.937	138.425	8.693	–	Irr	8.898	0.2186	0.066	3.426	MeerLICHT
(7)	J161137.84-602519.4	242.908	−60.422	0.611	1151.194	7897.11	11.126	32.211	1.218	0.234	−0.109	112.816	9.264	–	–	–	–	–	–	–
(8)	J161152.51-611137.9	242.969	−61.194	0.23	245.048	9905.25	14.618	18.745	0.676	0.056	0.692	141.504	9.037	–	SAc	10.111	1.0047	0.086	3.278	MeerLICHT
(9)	J161155.50-604329.0	242.981	−60.725	0.804	148.789	4932.15	22.633	28.446	0.651	3.422	1.923	70.459	8.974	–	Pec	9.399	0.6488	0.277	3.499	MeerLICHT
(10)	J161157.16-610749.8	242.988	−61.13	0.093	237.751	10085.1	7.584	10.954	0.806	−0.724	0.17	144.073	8.658	–	Irr	9.728	0.4602	−0.01	3.465	WKK98-6098 at v_{opt} = 10127.886 km/s
(11)	J161157.91-605757.3*	242.991	−60.966	0.18	147.111	10186.7	7.662	20.137	1.18	2.153	1.365	145.524	8.954	0.397	Irr	10.007	0.9216	−0.193	2.412	MeerLICHT
(12)	J161220.62-610632.3	243.086	−61.109	1.601	383.267	10221.7	47.393	55.404	0.544	1.969	1.393	146.024	9.906	–	E5	11.031	0.0606	−0.07	0.385	MeerLICHT
(13)	J161220.83-611321.4*	243.087	−61.223	0.539	161.39	9981.42	15.239	23.843	0.877	5.85	2.251	142.592	9.413	0.619	E5	9.783	0.1837	−0.157	1.566	ZOA-J16122118-6113155 at v_{opt} = 10215.075 km/s
(14)	J161243.55-613026.6*	243.181	−61.507	0.141	153.175	3053.29	11.033	15.54	0.781	−0.254	0.524	43.618	7.8	0.562	SA0	8.969	0.2499	0.123	3.615	WKK98-6139 at v_{opt} = 3071.211 km/s
(15)	J161326.06-604539.2	243.359	−60.761	0.119	159.268	4565.16	8.099	14.437	0.975	−0.497	0.185	65.217	8.077	–	SA0	9.873	1.8329	0.116	3.707	WKK98-6167/ESO137-G001 at v_{opt} = 4661 km/s
(16)	J161404.87-605503.0	243.52	−60.918	0.049	138.468	10353.5	5.598	7.057	0.655	0.437	1.057	147.907	8.402	–	E5	9.56	0.1655	−0.335	2.285	–
(17)	J161459.10-604603.5	243.746	−60.768	0.089	144.49	3344.9	6.469	11.236	0.957	−0.934	0.447	47.784	7.679	–	E5	8.877	0.0252	−0.093	2.893	MeerLICHT
(18)	J161500.28-604723.3	243.751	−60.79	1.573	220.692	5487.13	13.838	33.889	1.15	14.948	3.596	78.388	9.358	–	SAc	9.522	0.1283	−0.034	3.323	WKK98-6265 at v_{opt} = 5507.912 km/s
(19)	J161503.98-604505.6	243.767	−60.752	0.061	109.316	5512.67	7.766	9.037	0.537	2.363	1.48	78.752	7.948	–	E5	8.542	0.069	−0.629	5.252	MeerLICHT
(20)	J161545.47-612029.8	243.939	−61.342	0.146	66.492	9964.24	9.781	14.115	0.805	4.293	2.129	142.346	8.844	–	E	12.384	0.0029	−0.093	2.893	MeerLICHT
(21)	J161627.69-611421.3	244.115	−61.239	0.069	199.311	4598.69	8.384	9.744	0.535	−0.658	0.441	65.696	7.845	–	S0	9.065	0.1794	−0.01	3.036	MeerLICHT
(22)	J161905.01-611802.2*	244.771	−61.301	0.456	150.395	3811.86	9.774	35.124	1.289	4.056	1.917	54.455	8.504	0.484	Irr (S0)	8.52	0.1414	−0.237	0.148	MeerLICHT
(23)	J161959.55-610318.1*	244.998	−61.055	0.08	139.149	4826.71	7.713	13.491	0.962	0.259	0.595	68.953	7.954	0.527	E	8.907	0.3239	0.184	4.358	MeerLICHT
(24)	J161619.34-612641.8*	244.081	−61.445	0.566	391.506	9988.12	16.631	41.082	1.154	2.351	1.228	142.687	9.435	0.664	SAab	10.064	1.0015	0.192	2.24	WKK98-6339 at v_{opt} = 9950.398 km/s
(25)	J162058.75-602922.2	245.245	−60.489	4.714	152.028	604.07	43.354	130.175	1.231	3.507	1.873	8.63	7.918	–	E	8.685	0.0325	0.06	2.441	MeerLICHT

Table 2.2: HI Catalogue of the Detected Sources

2.6.2 HI Atlas

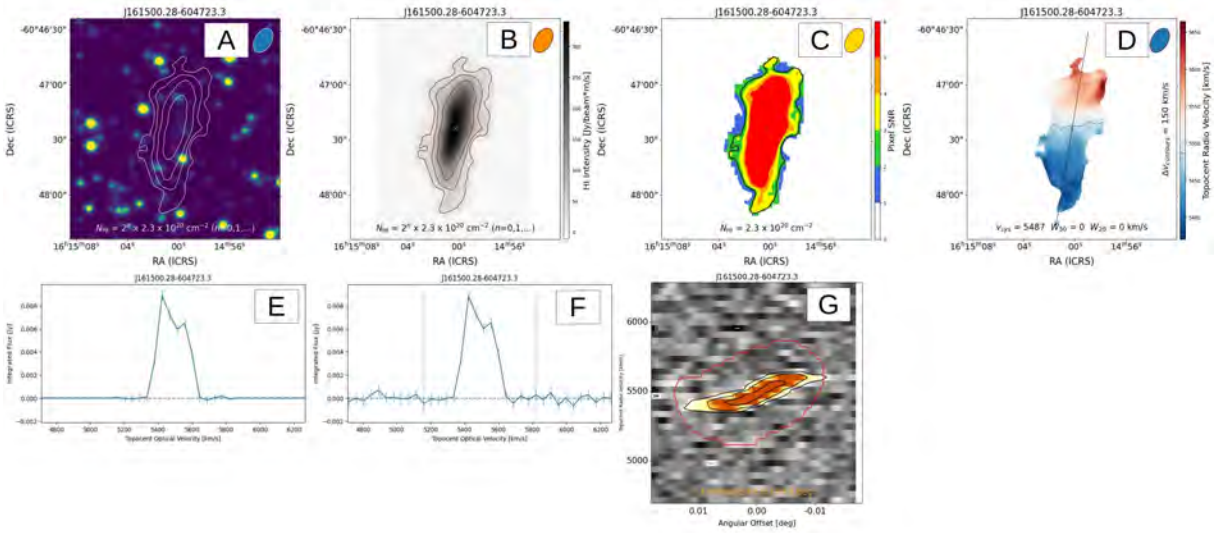

Figure 2.10: An example image of the HI products presented in the Atlas.

The HI Atlas of the detected galaxies is presented in this section. A sample of the Atlas of 25 HI detections is presented as combined images in Figure 2.19. The images were generated using the SoFiA-Image-Pipeline[9] (SIP: © 2022 Kelly M. Hess), and include HI column density contours overlaid on MeerLICHT optical images, total HI maps, pixel-by-pixel SNR maps, position velocity diagrams (pv-diagram) with SoFiA mask, and spectra. SIP generates images by plotting moment maps and cubelets for each detected source from the catalogue file produced by SoFiA-2[10]. The SIP pipeline can be run on the terminal by calling the Sofia-image-pipeline, the catalogue file, and other parameters[11]. Figure 2.10 is an example of the HI output products presented in the Atlas.

Panel A presents HI column density contours overlaid on MeerLICHT optical sky background in the *g*-band. SIP generates column density contours from the spectral maps produced by SoFiA, using the relation between N_{HI} and S_v for a source of constant

[9] https://github.com/kmhess/SoFiA-image-pipeline
[10] https://github.com/SoFiA-Admin/SoFiA-2
[11] https://github.com/kmhess/SoFiA-image-pipeline

T_B;

$$\frac{N_{HI}}{[\text{atoms/cm}^2]} \approx 1.823 \times \int \frac{T_B}{[K]} \frac{dv}{[\text{km/s}]}. \tag{2.6.1}$$

Panel B is the flux intensity map with HI column density contour overlays annotated on the bottom. The colour bar shows HI intensity in Jy/beam*m/s.

Panel C is the pixel-by-pixel SNR map with qualitative colour-bar scaling the signal above the noise ($\sigma = 0.09$ mJy/beam).

Panel D is the velocity field map with the arrow showing the kinematic major axis and the radial velocity annotated.

Panel E is the spectral profile without the noise.

Panel F is the full spectral profile of the gas disk with the noise, and the vertical line shows the borders of the SoFiA detection mask.

Panel G is the pv-diagram made by slicing through the cube along the kinematic major axis of the gas disk indicated in panel D.

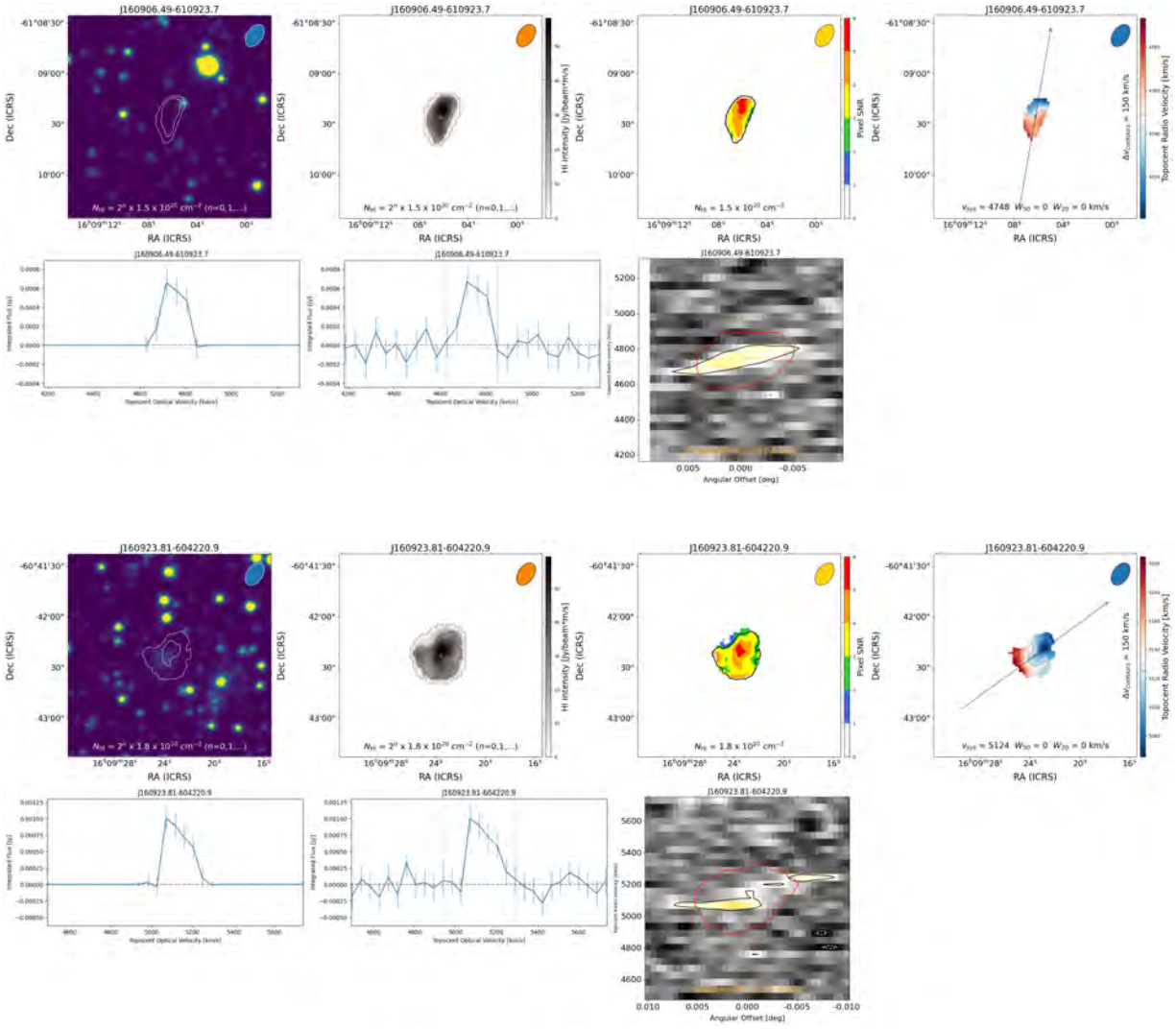

(a) $v_{opt} = 5213$ km/s

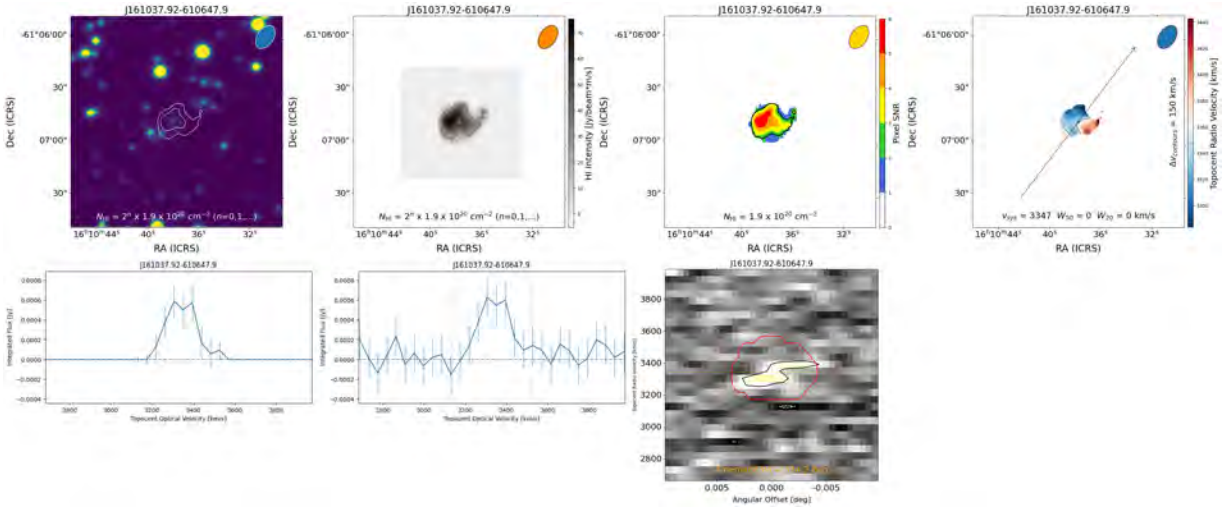

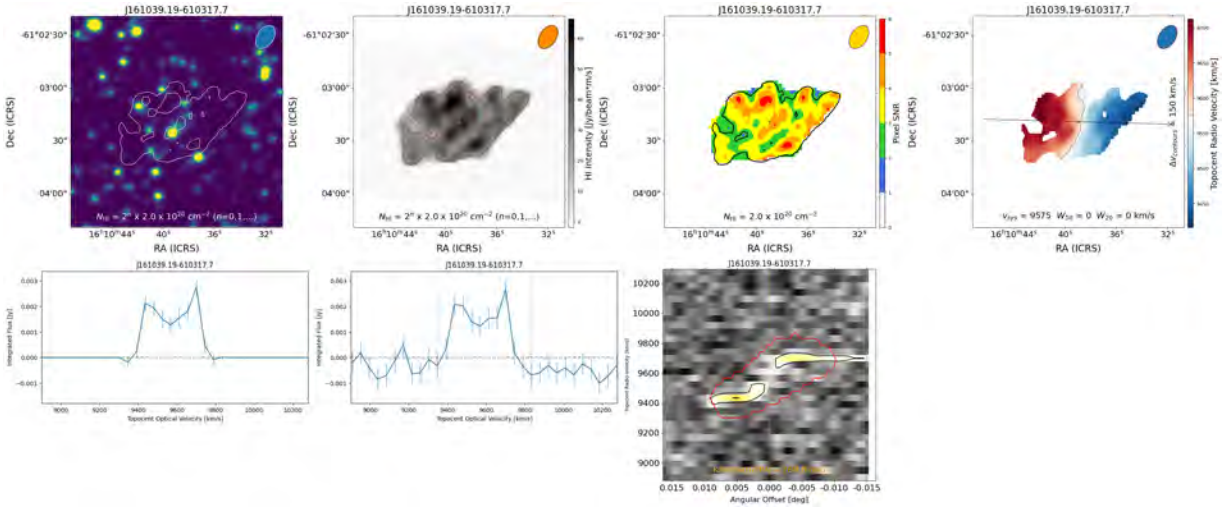
J161039.19-610317.7
RA (ICRS)
Dec (ICRS)
HI intensity [Jy/beam*m/s]
Pixel SNR
Topocent Radio Velocity [km/s]
Angular Offset [deg]

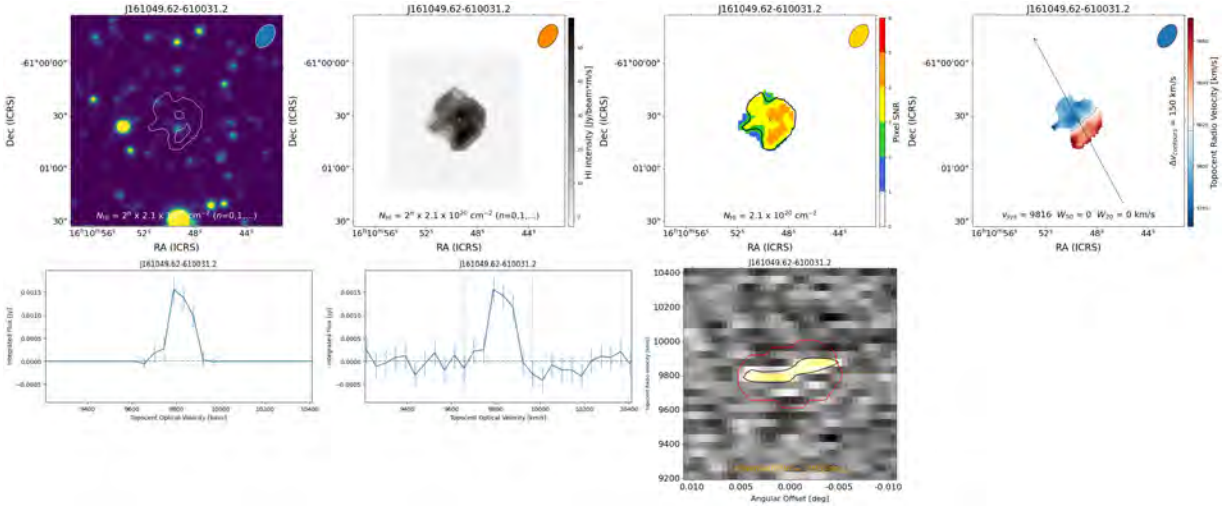
J161049.62-610031.2
RA (ICRS)
Dec (ICRS)
HI intensity [Jy/beam*m/s]
Pixel SNR
Topocent Radio Velocity [km/s]
Angular Offset [deg]

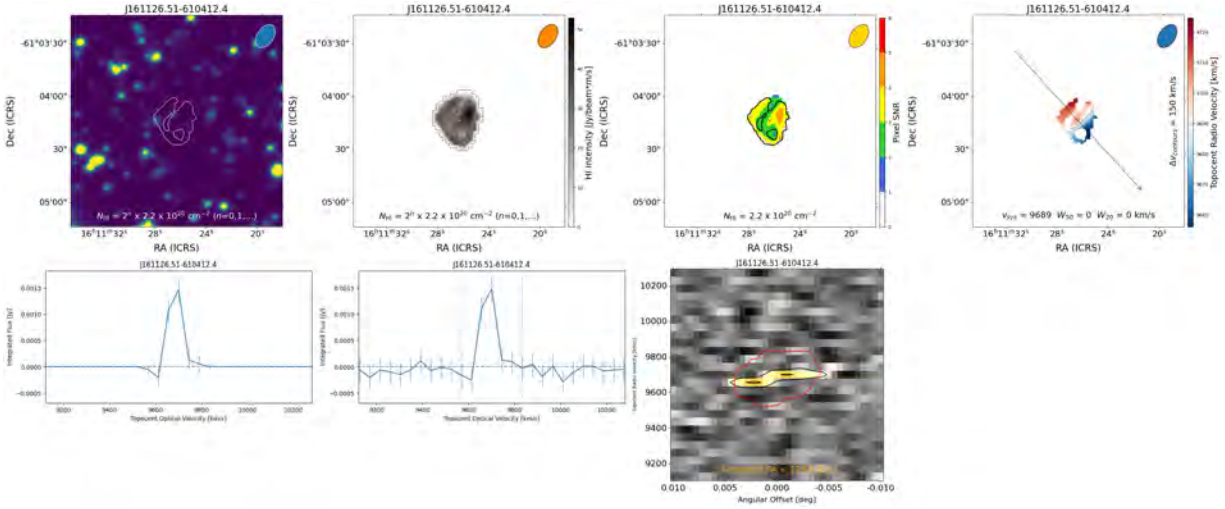
J161126.51-610412.4
RA (ICRS)
Dec (ICRS)
HI intensity [Jy/beam*m/s]
Pixel SNR
Topocent Radio Velocity [km/s]
Angular Offset [deg]

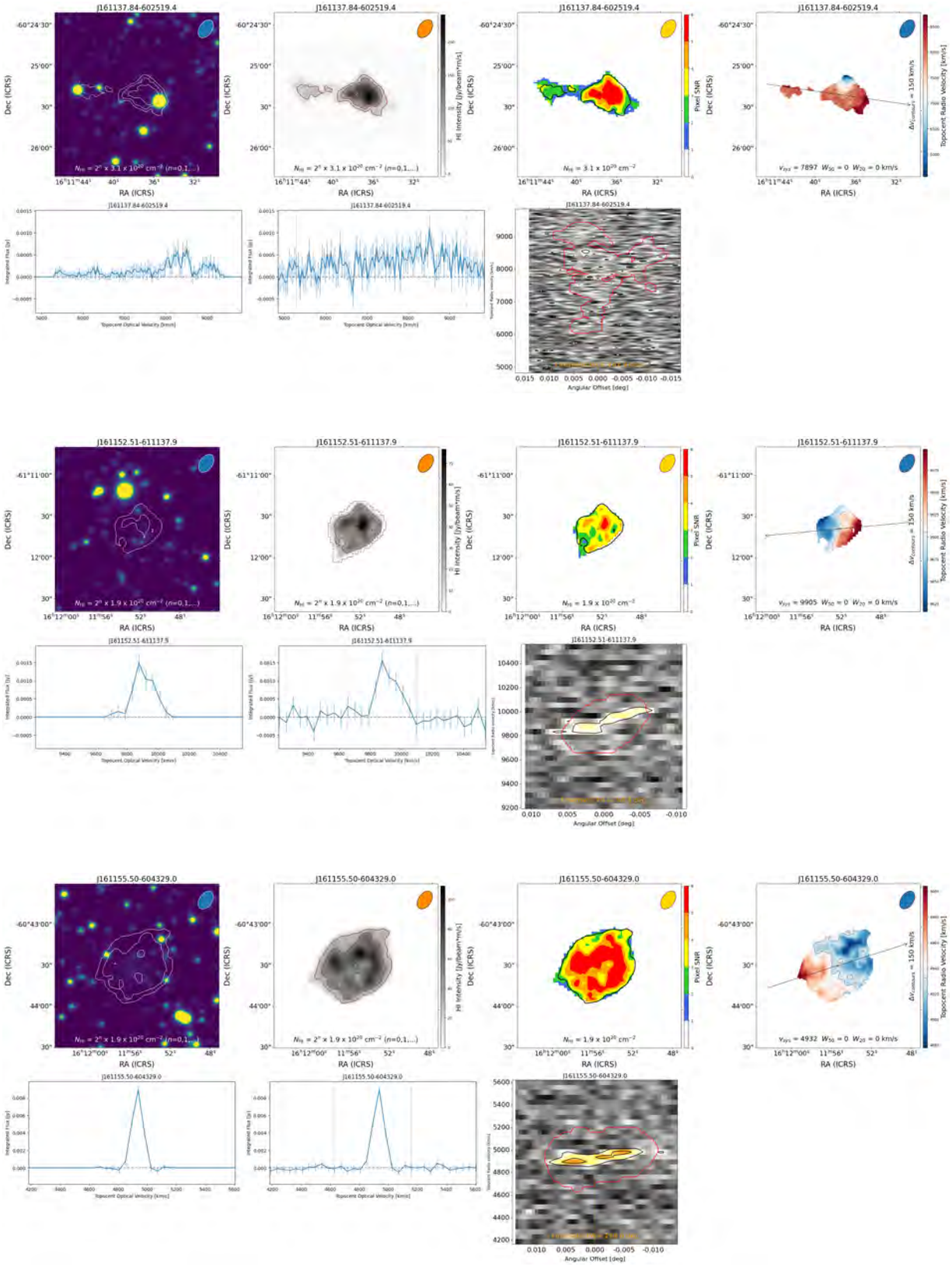
J161137.84-602519.4
J161152.51-611137.9
J161155.50-604329.0
RA (ICRS)
Dec (ICRS)
HI intensity [Jy/beam*m/s]
Pixel SNR
Topocent Radio Velocity [km/s]
Angular Offset [deg]

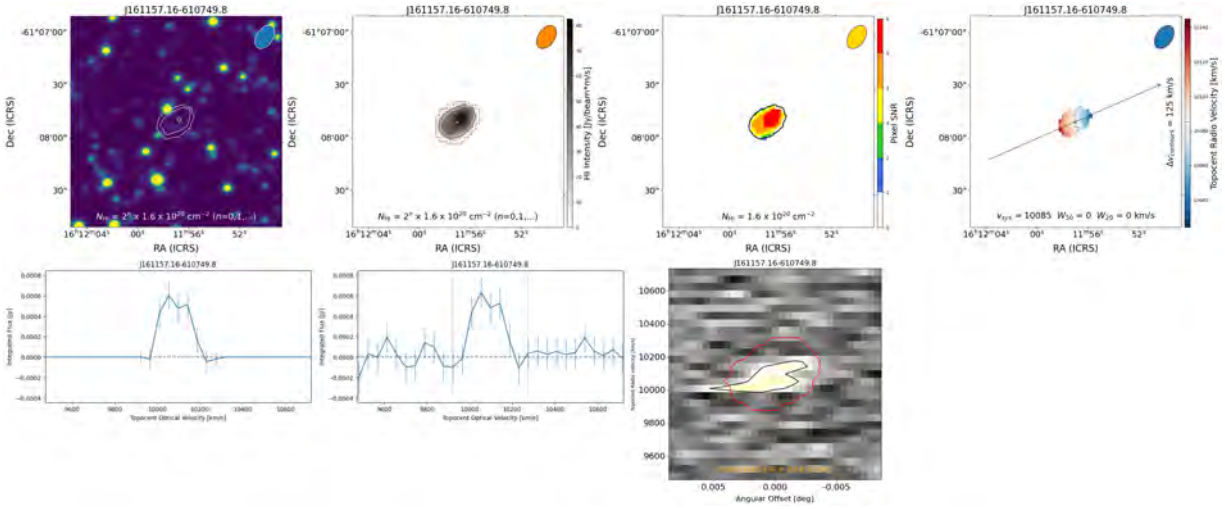
J161157.16-610749.8
Dec (ICRS)
RA (ICRS)
HI Intensity [Jy/beam*m/s]
Pixel SNR
Topocent Radio Velocity [km/s]
Angular Offset [deg]

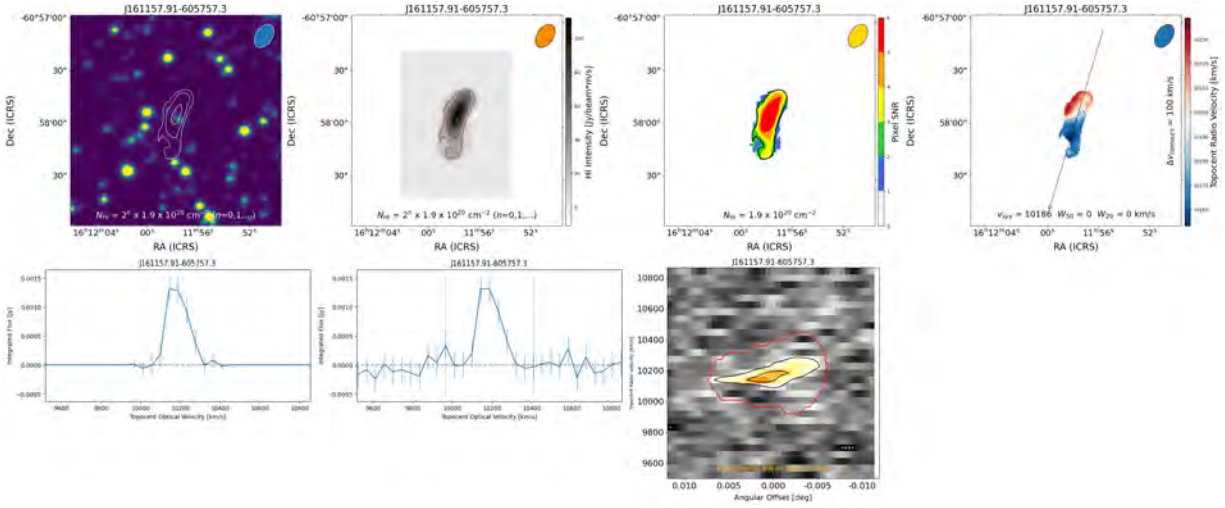
J161157.91-605757.3
Dec (ICRS)
RA (ICRS)
HI Intensity [Jy/beam*m/s]
Pixel SNR
Topocent Radio Velocity [km/s]
Angular Offset [deg]

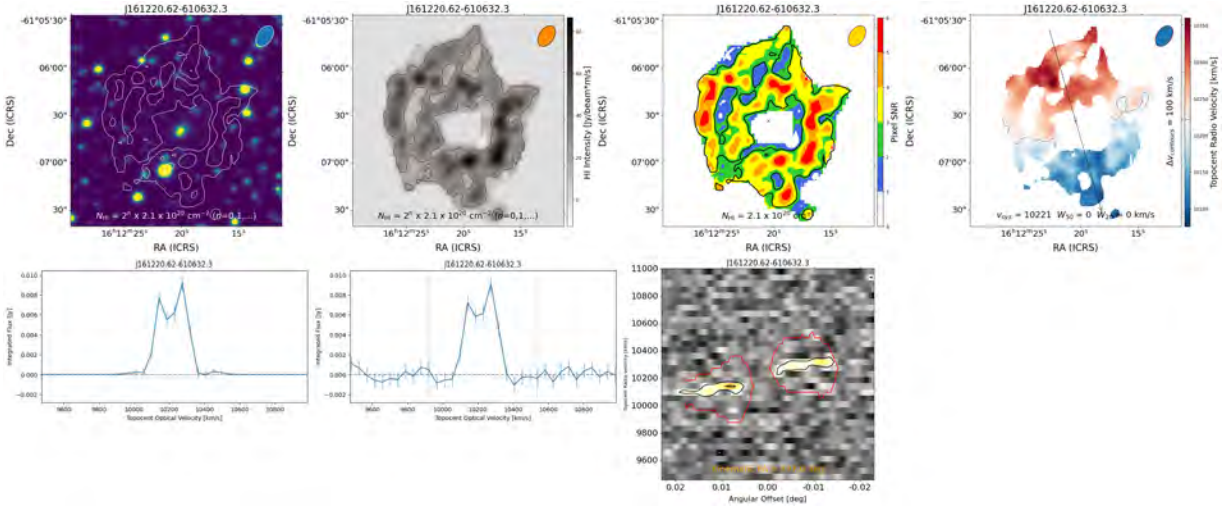
J161220.62-610632.3
Dec (ICRS)
RA (ICRS)
HI Intensity [Jy/beam*m/s]
Pixel SNR
Topocent Radio Velocity [km/s]
Angular Offset [deg]

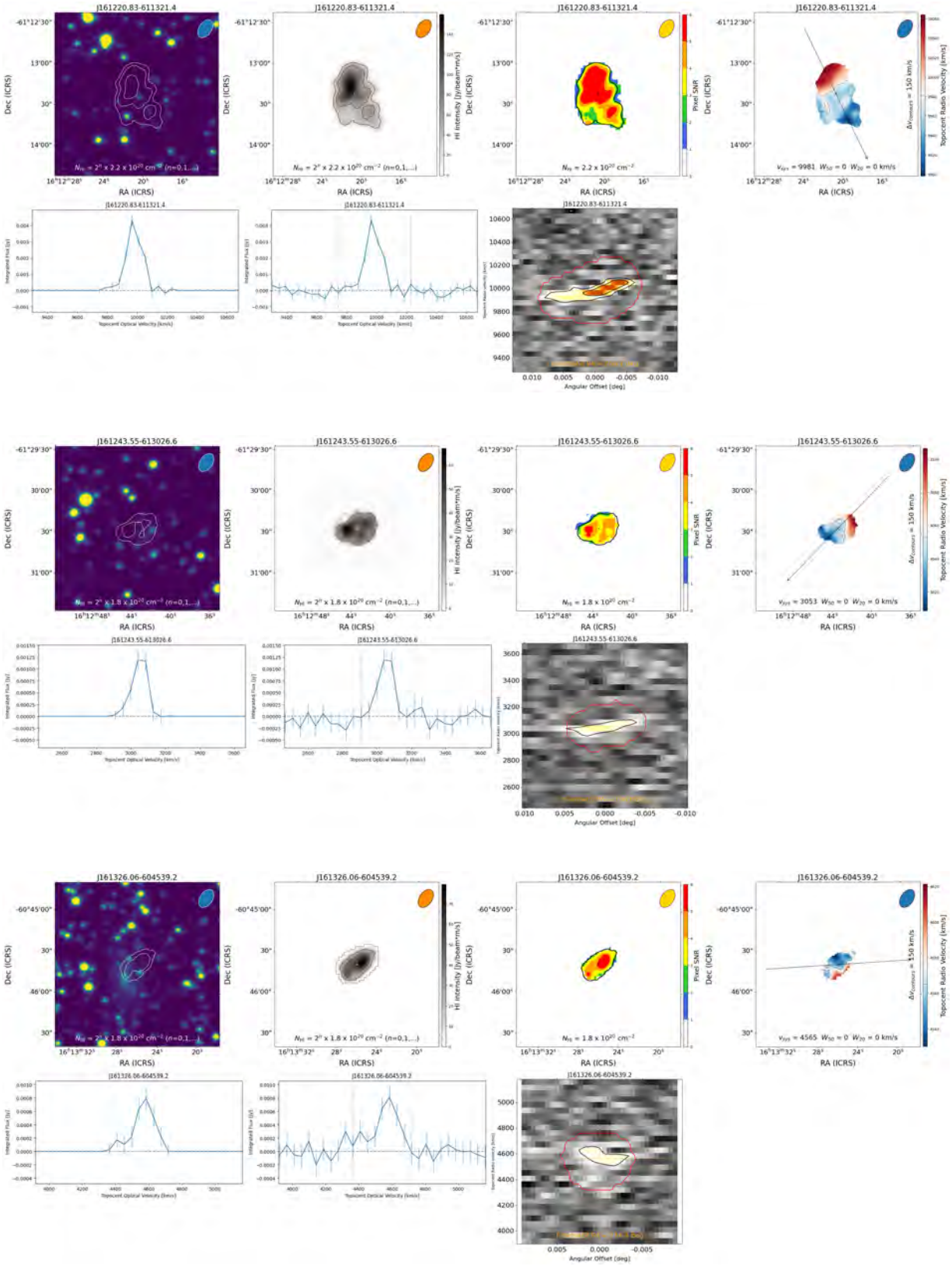
J161220.83-611321.4
J161243.55-613026.6
J161326.06-604539.2
RA (ICRS)
Dec (ICRS)
HI intensity [Jy/beam*m/s]
Pixel SNR
Topocent Radio Velocity [km/s]
Angular Offset [deg]

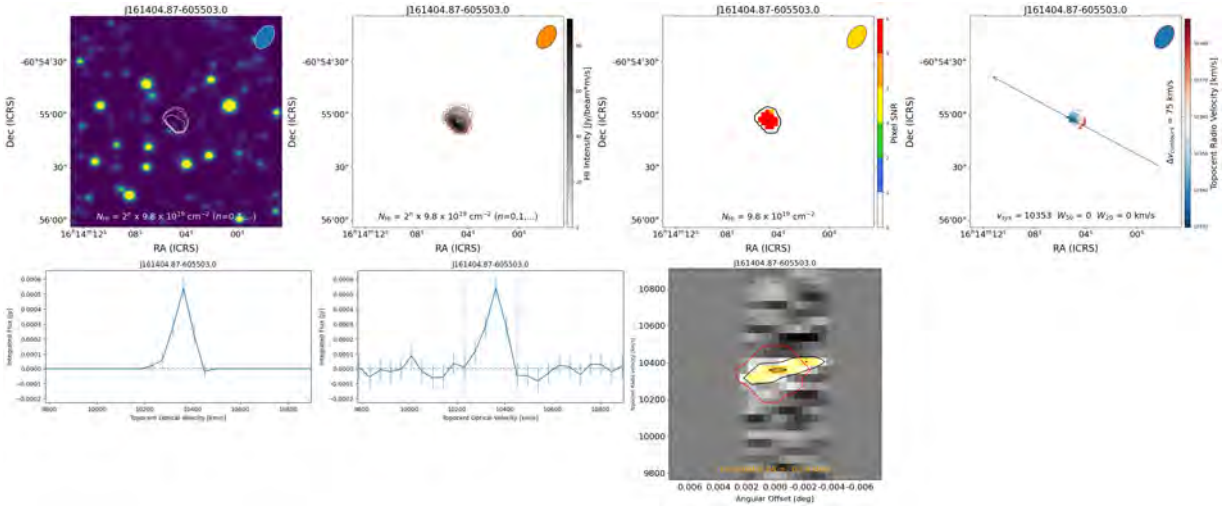
J161404.87-605503.0
Dec (ICRS)
RA (ICRS)
HI Intensity [Jy/beam*m/s]
Pixel SNR
Toposcent Radio Velocity [km/s]
Angular Offset [deg]

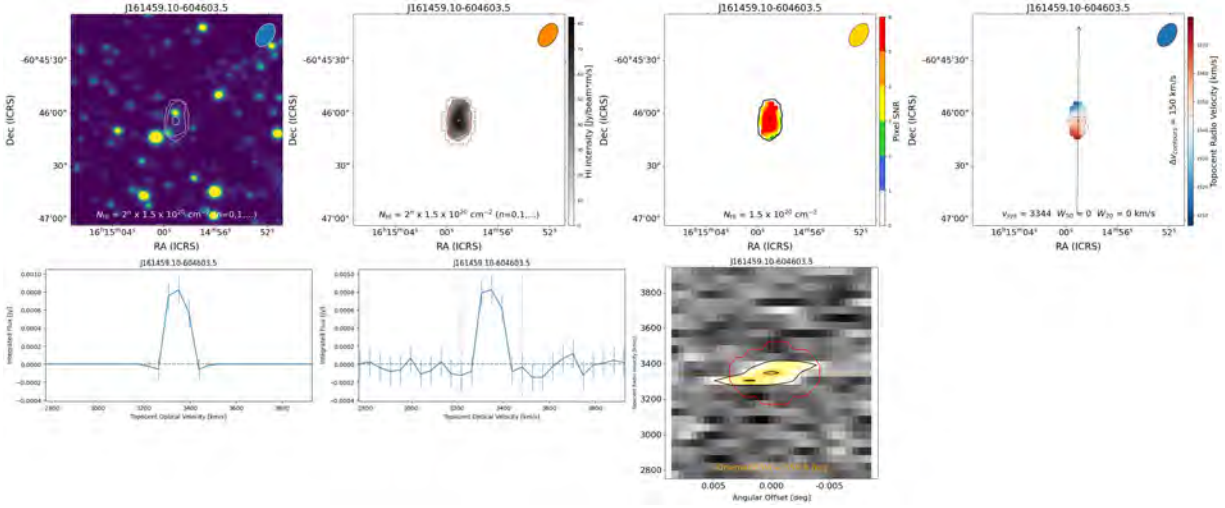
J161459.10-604603.5
Dec (ICRS)
RA (ICRS)
HI Intensity [Jy/beam*m/s]
Pixel SNR
Toposcent Radio Velocity [km/s]
Angular Offset [deg]

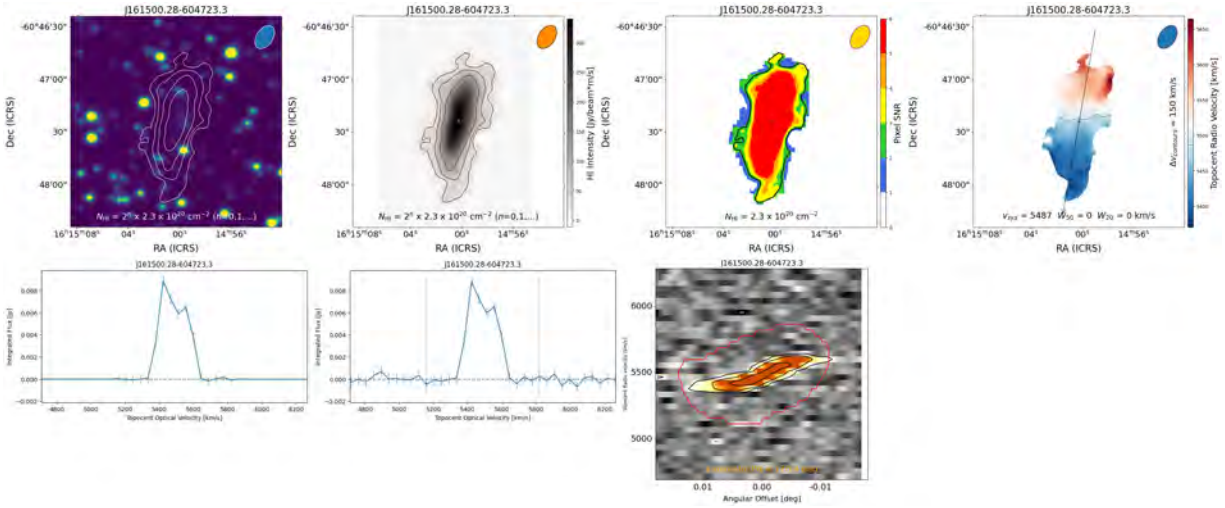
J161500.28-604723.3
Dec (ICRS)
RA (ICRS)
HI Intensity [Jy/beam*m/s]
Pixel SNR
Toposcent Radio Velocity [km/s]
Angular Offset [deg]

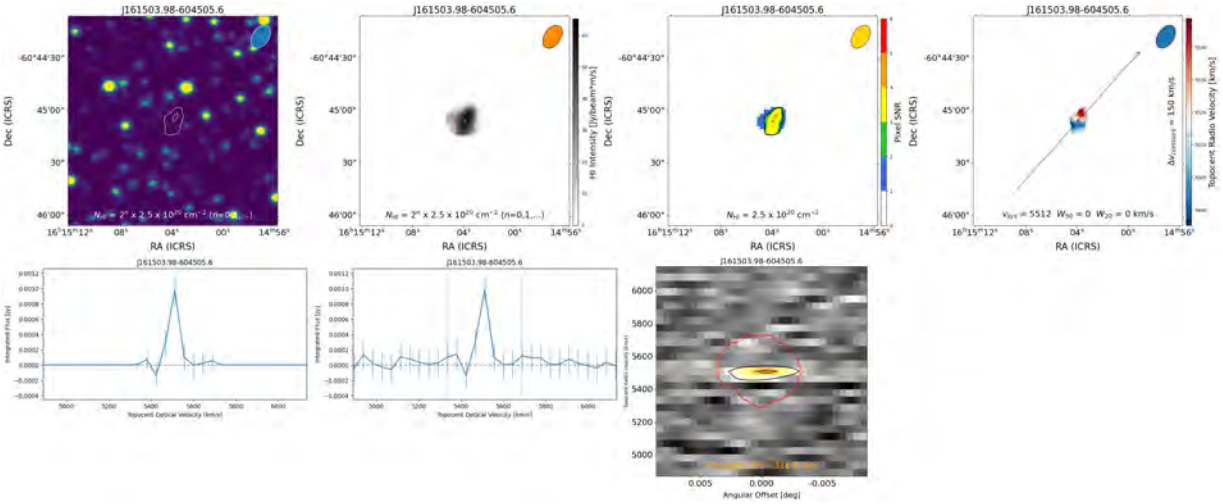
J161503.98-604505.6
Dec (ICRS)
RA (ICRS)
HI Intensity (Jy/beam*m/s)
Pixel SNR
Topocent Radio Velocity [km/s]
Angular Offset [deg]

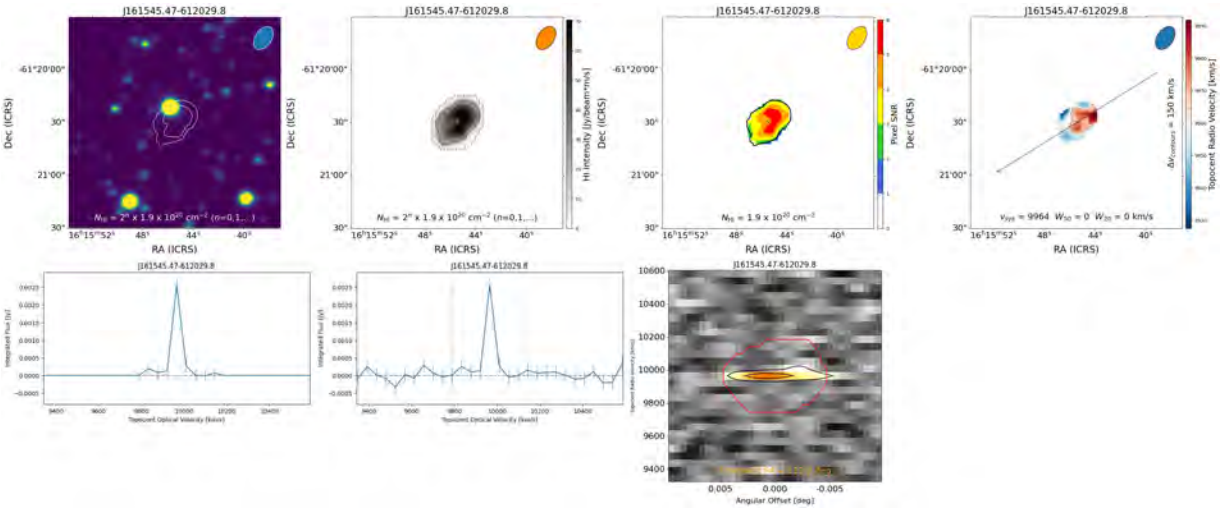
J161545.47-612029.8
Dec (ICRS)
RA (ICRS)
HI Intensity (Jy/beam*m/s)
Pixel SNR
Topocent Radio Velocity [km/s]
Angular Offset [deg]

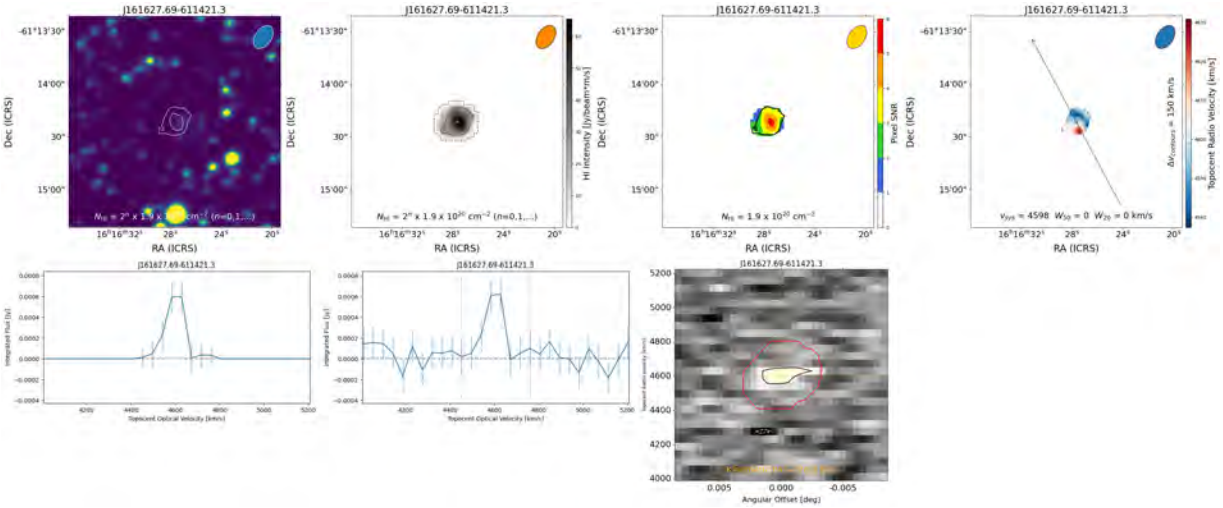
J161627.69-611421.3
Dec (ICRS)
RA (ICRS)
HI Intensity (Jy/beam*m/s)
Pixel SNR
Topocent Radio Velocity [km/s]
Angular Offset [deg]

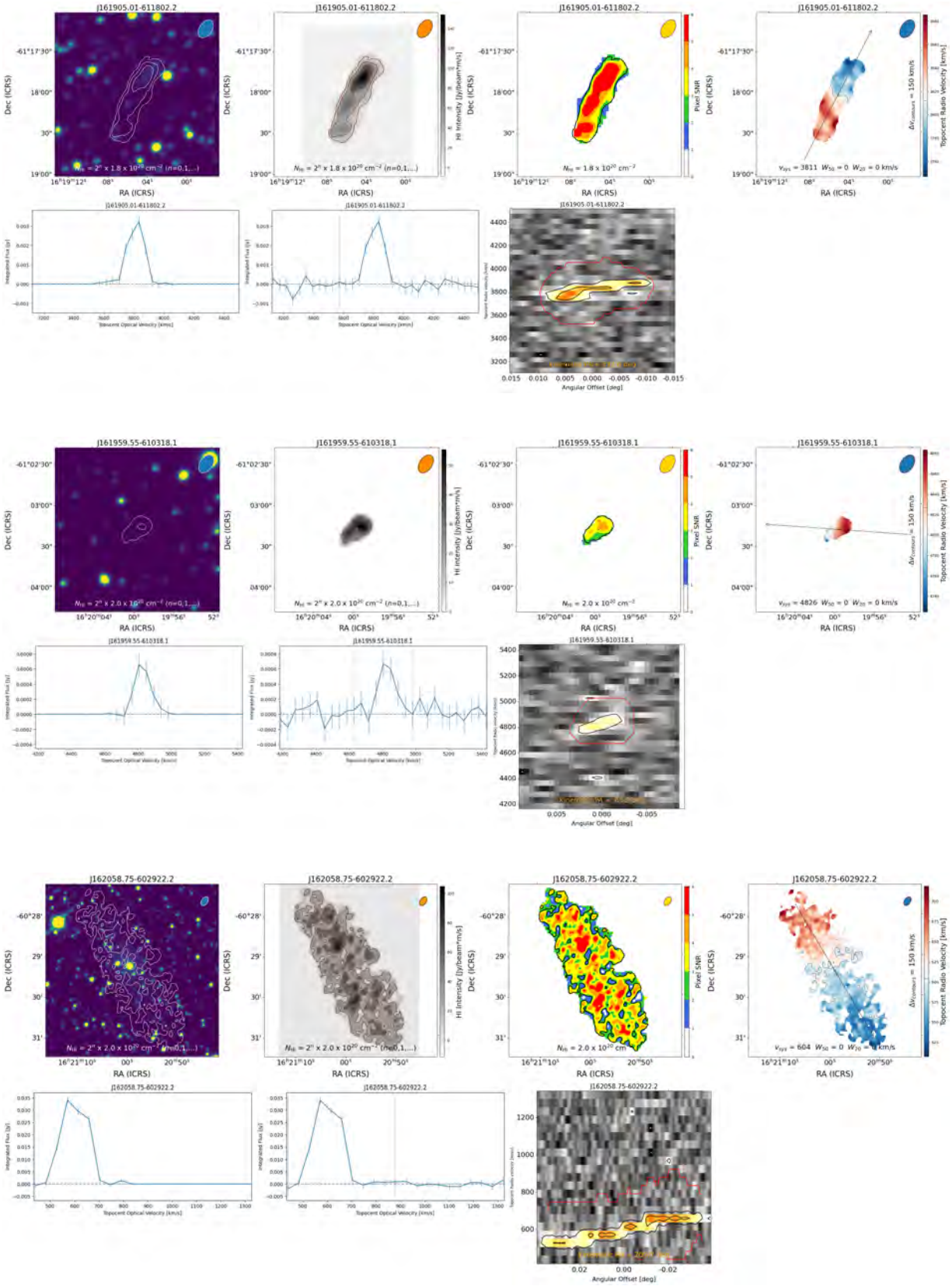
J161905.01-611802.2
J161905.01-611802.2
J161905.01-611802.2
J161905.01-611802.2
Dec (ICRS)
RA (ICRS)
HI intensity [Jy/beam*m/s]
Pixel SNR
Topocent Radio Velocity [km/s]
J161905.01-611802.2
J161905.01-611802.2
J161905.01-611802.2
Angular Offset [deg]
J161959.55-610318.1
J161959.55-610318.1
J161959.55-610318.1
J161959.55-610318.1
J161959.55-610318.1
J161959.55-610318.1
J161959.55-610318.1
Angular Offset [deg]
J162058.75-602922.2
J162058.75-602922.2
J162058.75-602922.2
J162058.75-602922.2
J162058.75-602922.2
J162058.75-602922.2
J162058.75-602922.2
Angular Offset [deg]

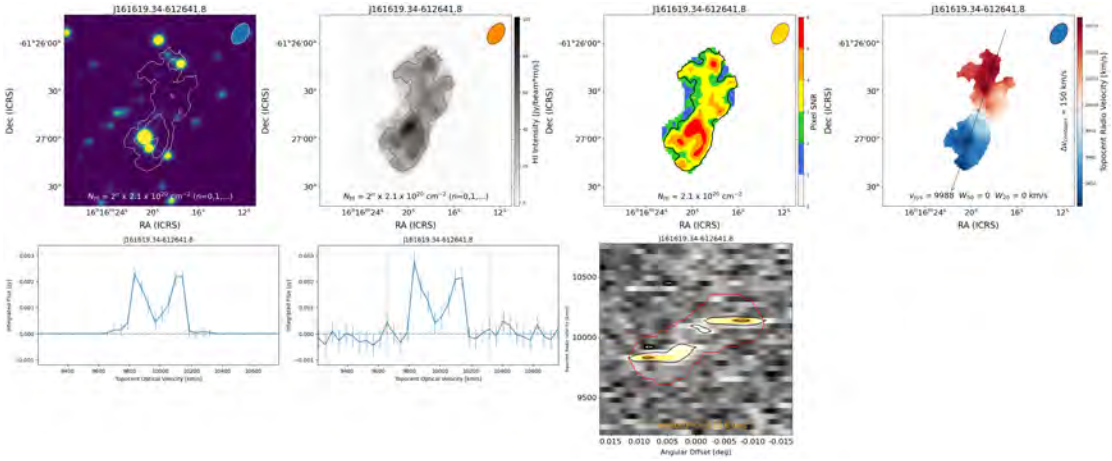

Figure 2.19: The Atlas of all HI detections. Each panel figure is illustrated and described in Figure 2.10. For each detection, the figure presents combined images of column density contours overlaid on MeerLICHT optical sky in the g-band, column density contours overlaid on a moment-0 map, pixel-by-pixel SNR output-imagemap, pv-diagram with SoFiA mask indicating topocent radio velocity change along the colour-scale, galaxy spectral profile with and without the noise and pv-diagram. The contour levels are $N_{HI} = 2^n \times 2.0 \times 10^{20}$ cm^{-2}, n = 0, 1, ...

Chapter 3

HI Properties and Environmental Effects

In the previous chapter, we studied the global HI properties of galaxies detected in the Norma cluster field. The radial velocity range of galaxies in the Norma cluster is $\sim 2096 - 7646$ km/s and the mean radial velocity is $v_{A3627} \sim 4871$ km/s, with a velocity dispersion of $\sigma_{A3627} = 925$ km/s (Woudt et al. 2007; Mutabazi et al. 2014).

MeerKAT 21 cm observations covered a velocity range of $483 - 11,113$ km/s. Cluster members are selected from all HI and optical (Woudt et al. 2007) observations with the criterion that their radial velocities are within the range $\sim 2096 - 7646$ km/s. Based on this condition, a total of 13 HI detections and 130 optical galaxies were determined to be cluster members.

3.1 The distribution of galaxies in the Norma cluster

The radial velocity distribution of HI and optical cluster members is presented in Figure 3.1. The distribution hints at substructuring in optical and HI, peaking at ~ 5281 km/s. This distribution has 2 distinct main HI overdensities. The most prominent is within the velocity range of $\sim 4565 - 5512$ km/s in which 62% of the cluster members are located and peaking at ~ 4870 km/s. The peak in the HI substructure is consistent with that seen in optically detected galaxies. The second population has 31% of cluster members and peaks at a slightly lower velocity of 3230 km/s. This overdensity is likely a group of galaxies infalling into the Norma cluster.

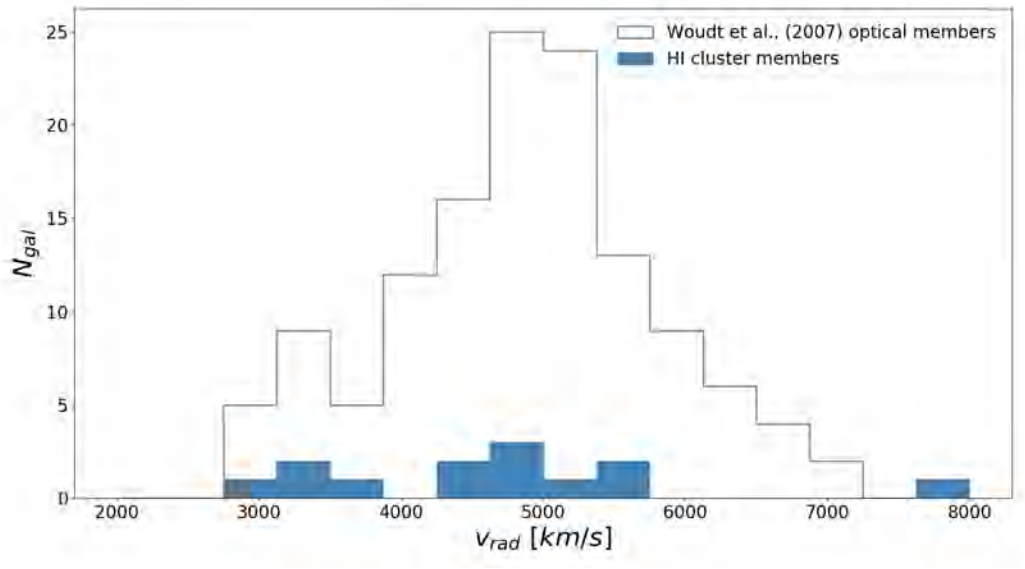

Figure 3.1: The radial velocity distribution of galaxies in the Norma cluster. The blue histograms are galaxies detected in HI, and the black-edge bins are galaxies detected at optical wavelengths.

The spatial distribution of HI cluster members is shown in Figure 3.2. In this figure, the HI detected galaxies and X-ray contours are overlaid on MeerLICHT optical in the g-band. We selected the MeerLICHT optical sky for this study due to the large Point Spread Function (PSF) in IR images. This characteristic leads to lower resolution, potentially causing confusion, especially in the case of probing structures in the location of the GA. From this plot, we find that 69% of the HI galaxies are detected at the outskirts. This leaves the cluster core with only $\sim 21\%$ of the HI detections found just outside the X-ray emission. MeerLICHT galaxies in the optical are very faint due to extinction (see Sect. 2.4). However, there are optically prominent E/S0 in the core, such as the 2 cD galaxies indicated with open purple circles that are visible to inspect from Figure 3.2. The distribution of optical galaxies is elongated along the dominant angle.

As a result of the unresolved overlay observed in Figure 3.2 due to the presence of dust extinction in the optical range, we superimpose moment-0 images of the identified galaxies onto the X-ray emission emanating from the ICM region in Figure A.1, in Appendix A.3. The X-ray image was generated with data from XMM-Newtown[1] (Jansen et al.

[1]https://www.cosmos.esa.int/web/xmm-newton

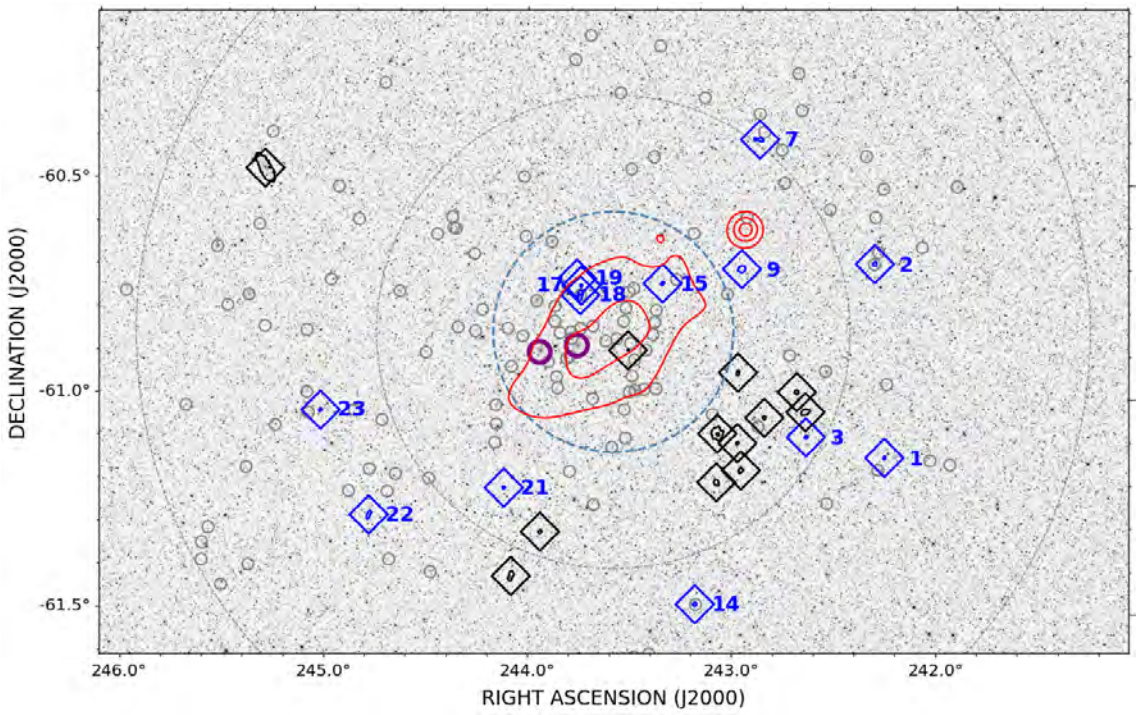

Figure 3.2: The global spatial distribution of HI gas disks, and optical galaxies overlaid on MeerLICHT optical in the g-band. The grey open circles are the optical cluster members. HI cluster members are indicated with blue diamond-shaped markers framing blue column density contours and are labelled according to row numbers in Table 2.2. The HI non-cluster members are indicated with black column density contours and black diamond-shaped markers. HI column density contours are overlaid at levels of 1.5×10^{19} and 3.0×10^{19} atoms/cm^2, while the red X-ray contour levels are 40.00, 69.47 and 98.95 c/s/deg^2. The cluster core is $1/6 \times \mathrm{R_A} = 0.34$ Mpc, indicated by the blue circle. The outer grey dashed circles indicate $1/3 \times \mathrm{R_A}$ and $2/3 \times \mathrm{R_A}$ (Woudt et al. 2007). The cD galaxies, WKK6312 and WKK6269 (PKSB 1610-608), are indicated with purple circles.

2001). In the Figure, the galaxy overlays are the groups in the central region and the background group at $\mathrm{v_{rad}} \sim 10,000$ km/s, located in the South-Eastern region. A strong peak with a flux density of ~ 98.95 c/s/deg^2 can be seen in the central region of the map, where no cluster member was detected in HI. The ICM is elongated along the dominant angle, extending to a radius of ~ 1 deg. This may be the region associated with gas stripping and galaxy transformation due to galaxy-ICM interactions (Bohringer et al. 1996; Woudt et al. 2007). The Norma cluster is the 6^{th} brightest in X-ray according to the ROSAT All Sky Survey (Bohringer et al. 1996), and the X-ray emission shows the distribution of the ICM in the cluster. The core comprises many prominent galaxies

observed in optical wavelengths that are deficient in HI. This pronouncement may indicate ongoing processes transforming galaxies into gas-poor, early-types in the cluster's core.

While no HI galaxies are currently detected within the dense ICM, it is important to note that the galaxies nearest to the dense ICM region are predominantly truncated.

3.2 Substructures in HI

In section 3.1, the X-ray of the cluster ICM shown in the red contours in Figure 3.2 and inferno colourmap in Figure A.1 show that the cluster has not yet reached a dynamically relaxed state. Moreover, in Figure 3.1, it is shown that both HI and optical observations mimic the same trend in the velocity distribution, with hints of subclustering in both cases (section 2.3). In this section, our main objective is to examine the spatial distribution of HI substructures. This is conducted by overlaying the HI galaxies on the substructures already defined using optical Norma galaxies.

Woudt et al. (2007) classify optical galaxies by morphology into either the E/S0 or S/Irr populations and conduct incremental radii analysis with R $<$ 0.67 Mpc, R $<$ 1.35 Mpc and R $<$ 2.02 Mpc. After this, the Dressler-Schectman test was employed to characterize substructures in the Norma cluster. They revealed two main substructures; one comprises the E/S0 population, which is more relaxed and largely populated in the core of the cluster with a radius of R $< 1/3 \times R_A$. On the other hand, the S/Irr population is distributed mostly in the cluster outskirts, but it is elongated along the dominant angle of the X-ray emission. This could imply that the S/Irr population is infalling along the angle of the X-ray emission.

Figure 3.4 illustrates the spatial distribution of substructures, wherein galaxies are categorized based on their radial velocity, enabling a comparative analysis with indications of substructuring observed in the velocity distribution. The red galaxies are those belonging to the main galaxy peak in the HI distribution in Figure 3.1 i.e., $v_{rad} \sim 4565 - 5512$ km/s. Detections in blue are those found in the secondary overdensity in the velocity range $\sim 3053 - 3811$ km/s.

As aforementioned, the dominant substructure comprises mainly early-type galaxies from the optical catalogue. Within this region ($1/6 \times R_A$), only 4 HI detections are

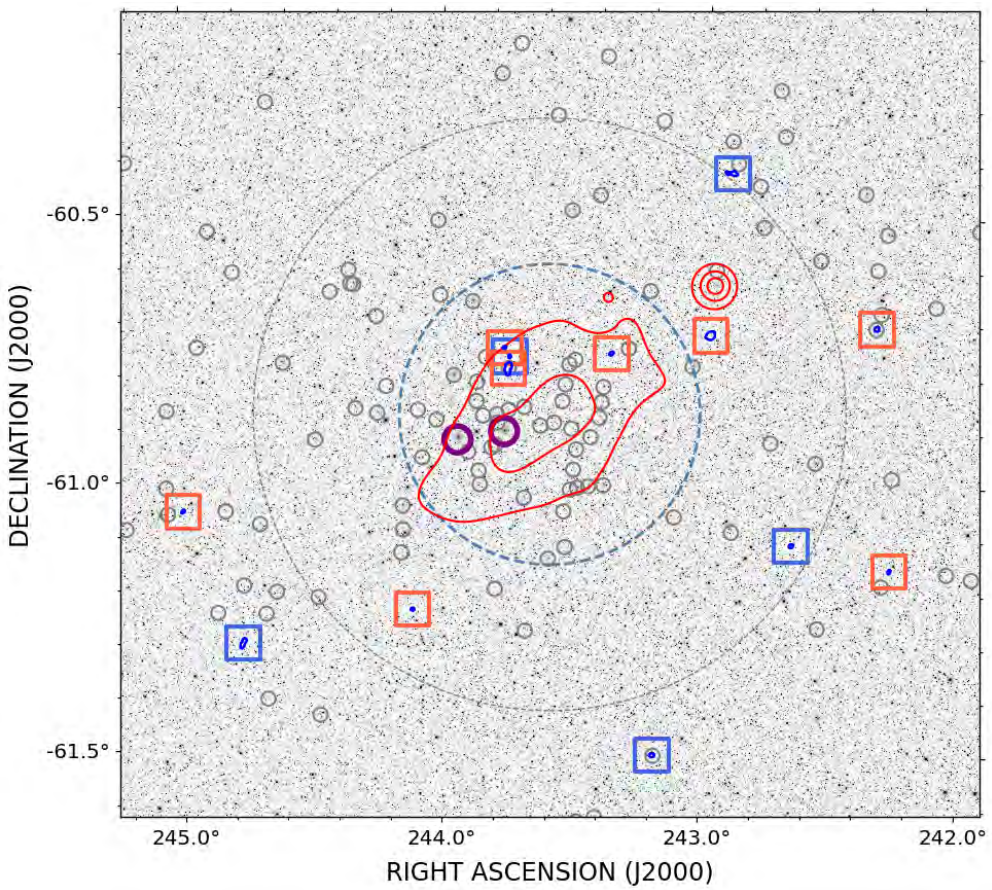

Figure 3.3: The spatial distribution of HI substructures in the Norma cluster produced as in Figure 3.2. The red square-box markers indicate HI detections in the velocity range of $v_{rad} \sim 4565 - 5512$ km/s which corresponds to the main overdensity in the velocity distribution shown in Figure 3.1, while the blue markers indicate galaxies in the low-velocity range of $3053 - 3811$ km/s.

found. Three of these have velocities consistent with the main HI density in the velocity distribution. The 5 detections in the radial velocity range $\sim 3053 - 3811$ km/s are dispersed at the outskirts and elongated similar to the S/Irr optical population (Woudt et al. 2007), while the substructure with most of the HI detections, i.e., the 8 detections in the radial velocity range $\sim 4565 - 5512$ km/s, exhibit a more elongated substructure.

In Figure 3.4, substructures are delineated by HI gas disk morphology, and spatially resolved detections are colour-scaled to A_p. The HI detections in the central regions (black open circles) are symmetric. However, an examination of the HI intensity map also reveals that while symmetric, the HI gas disks are highly truncated. Only one HI gas disk was detected in the centre, indicating a gas deficiency in the core of the

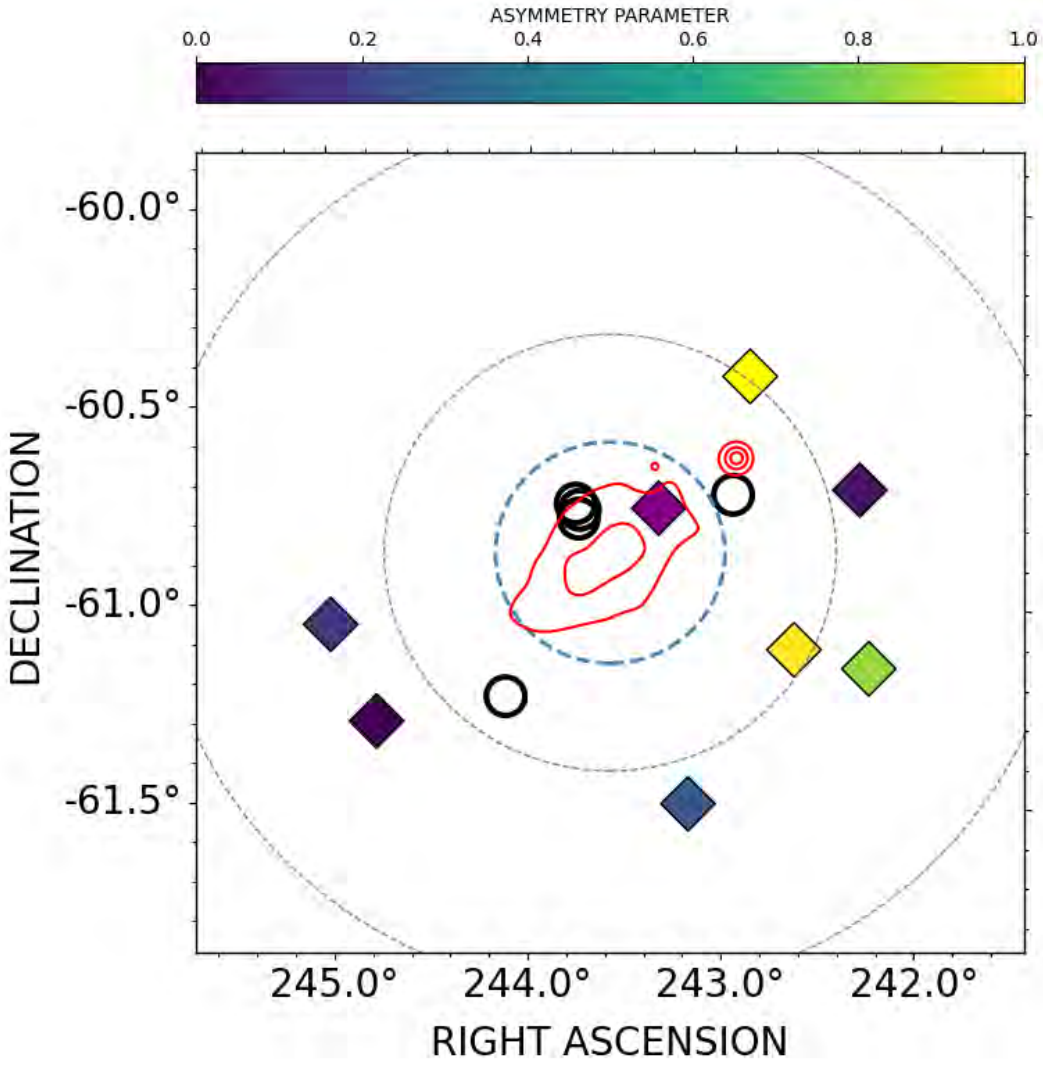

Figure 3.4: The spatial distribution of HI substructures and the X-ray ICM structure in the Norma cluster. Galaxies are illustrated according to the HI morphology. Symmetrical gas disks are indicated with black circle markers located in the central regions. Diamond-shaped markers indicate asymmetrical gas disks colour-scaled to A_p. The blue dashed and dashed grey circles were produced as in Figure 3.2. Asymmetrical gas disks were found to be located on the outskirts.

Norma cluster. On the other hand, HI detections found within the S/Irr substructure at velocities of $3053 - 3811$ km/s, have asymmetries, with A_p ranging from 0.3 to 1.0.

3.3 Environmental effects

3.3.1 The Norma cluster in Phase-Space

In section 3.2 we discussed the HI substructures by morphology as a function of the projected distance from the cluster core. There appears to be an association between the gas asymmetries in galaxies and the projected distance from the cluster centre. A pronounced incident of the asymmetrical galaxies at the outskirts was revealed. Gas disks detected near the cluster centre appear to have the most truncated gas disks.

Studies have shown that long-lasting, pronounced, violent transformations are caused by galaxy-ICM interactions in massive, X-ray-selected galaxy clusters, from shock compression that triggers starbursts to gas removal, for galaxies in-falling into the cluster core (e.g., Ebeling et al. 2014). For example, galaxies in the Virgo cluster were revealed to have HI deficiencies dependent on their radial orbits, and RPS was found to increase the central gas surface density of the affected gas disks (Vollmer et al. 2001b). These studies show that the initial phase of RPS may be responsible for disturbed gas disk morphologies, and it is reasonable to assume such interactions to occur at pericentric distances within the ICM structure. Therefore, tracing and characterizing the orbital trajectories of the detected gas disks is sensible to qualify environmental effects causing the observed asymmetrical morphologies and truncated gas disks.

The position-velocity space diagram (phase-space diagram, PSD) has been applied as a useful tool to qualify environmental effects by examining the projected radius and the line-of-sight (l-o-s) velocity of galaxies in the cluster frame (e.g., Mahajan et al. 2011; Oman et al. 2013; Hernández-Fernández et al. 2014; Jaffé et al. 2015; Ramatsoku 2017; Rhee et al. 2017; Yoon et al. 2017). It has been shown that galaxies can be characterized as either "infalling", "virialized", or part of the "backsplash" population. From these orbital histories, it is possible to assess the active gas-stripping mechanisms within different regions of the diagram.

To achieve this, we first characterize the different stages in the orbital trajectories indicated by the black solid line in the PSD in Figure 3.5 according to the regions highlighted. A cluster accretes matter from $r/R_{200} > 1$, infalling with a speed close to the cluster escape velocity. The galaxy radially orbits around the cluster while experiencing a pull into the central regions. At first infall, the galaxy approaches the cluster core with

an increasing velocity until it reaches its maximum velocity in the cluster centre and decreases in velocity after crossing. The galaxy oscillates back and forth through the cluster centre and back at the outskirts until it settles in the central, virialized region.

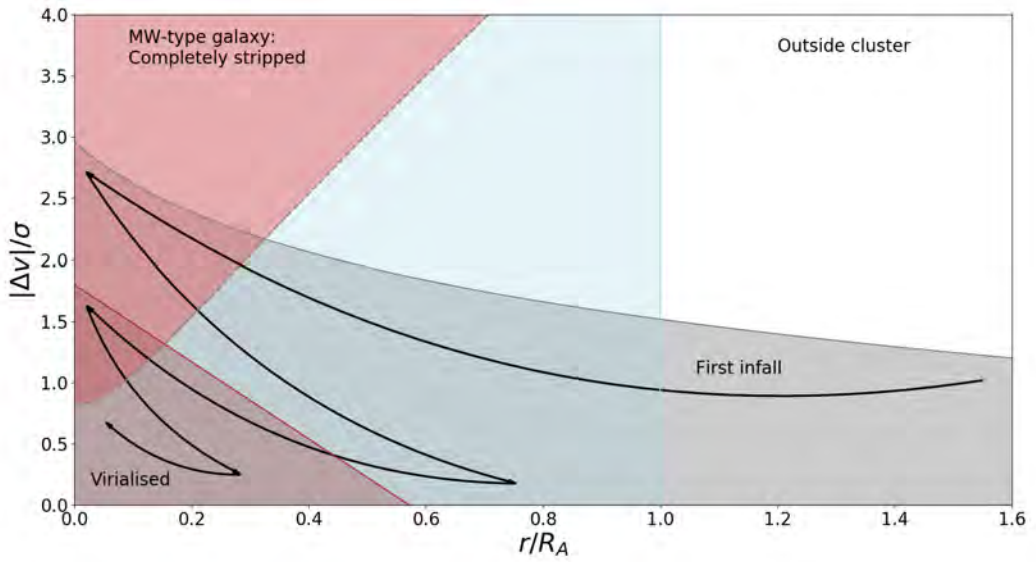

Figure 3.5: Schematic phase-space diagram showing the orbital trajectory of an in-falling galaxy, illustrated by the continuous solid lines. The cluster potential delineated by the escape velocity is shaded in grey, the virialized region is in brown, the stripping region is in red, and the cluster field within the Abell radius is the rectangular region indicated in light blue.

In this section, we explore the location of HI/optical galaxies in the cluster projected phase-space in an attempt to gain further insights into how the inferred orbital histories of galaxies impacted their asymmetrical HI morphologies. For all galaxies detected in HI, we normalized their projected clustercentric distance by the cluster virial radius, R_{200}, in the x-axis (r_{gal}/R_{200}; Quintero et al. 2005). R_{200} is conventionally defined as the virialization radius containing matter at 200 times the background density in an environment at hydrostatic equilibrium. On the y-axis, the l-o-s velocity normalised by the velocity dispersion (Tempel & Tenjes 2006; Oman et al. 2013) was determined using the formulation;

$$\frac{|\Delta v|}{\sigma} = \frac{c(z - z_{cl})}{\sigma_{cl}(1 + z_{cl})}, \tag{3.3.1}$$

where c is the speed of light, z_{cl} is the cluster redshift, z is the galaxy's redshift and σ_{cl} is the cluster velocity dispersion. The Norma cluster is observed at a redshift of

$z_{cl} \approx 0.0162$ and velocity dispersion of $\sigma_{cl} = 925$ km/s (Woudt et al. 2007).

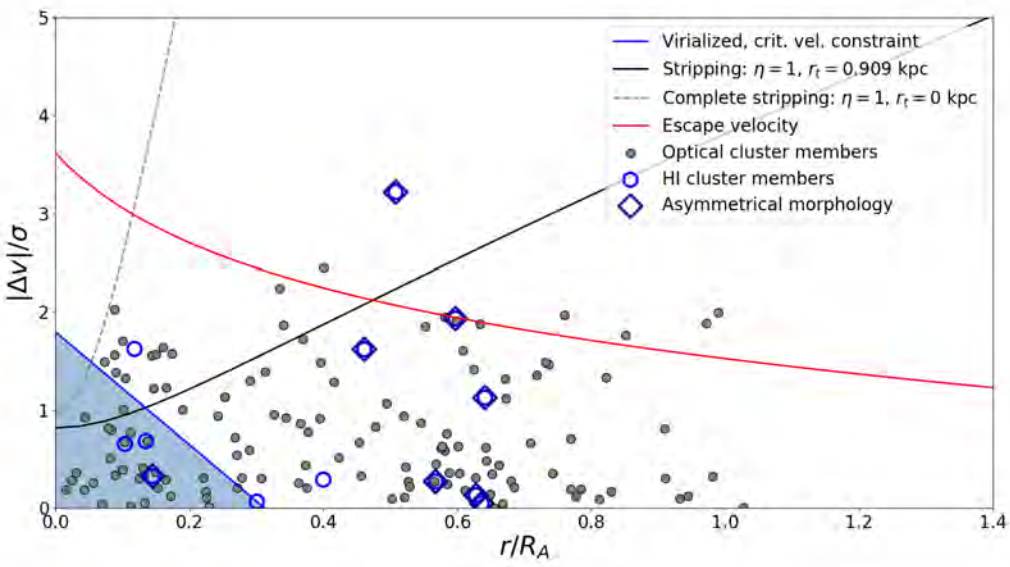

Figure 3.6: Phase-space diagram for optical (black circles) and HI (blue diamonds) galaxies in the Norma cluster. HI gas disks with asymmetrical morphologies are indicated with dark blue diamond-shaped markers. The area shaded in sky-blue is the virialized region. The area above the grey dotted line indicates the region of complete stripping where a MW-type galaxy is stripped out to $r_t = 0$ kpc, and the black line indicates the region where a MW-type galaxy is stripped only to $r_t \sim 0.909$ kpc. The red line indicates the cluster escape velocity. We use the Abell radius from optical studies ($R_A = 2.02$ Mpc) although the spatial distribution of selected HI and optical galaxies only extend out to $2/3 \times R_A$, i.e., $r/R_A < 1$ for all selected galaxies.

Figure 3.6 is the PSD of galaxies in the Norma cluster. Galaxies are accreted from larger radii and become members of the virialized population in the cluster center as processed early-types. This virialized region is shown by the area shaded in sky-blue, based on Equation 2 in Mahajan et al. (2011); i.e.,

$$\frac{v_{crit}}{V_v} = -1.8 + 1.06(r/R_c), \tag{3.3.2}$$

where v_{crit} is the critical radial velocity separating the infalling ($v < v_{crit}$) from the backsplash and virialized populations; and $R_c = 0.184$ Mpc from the β-model (Sivanandam et al. 2010). The term v_{crit} is normalized by the local velocity dispersion of the virialized particles, and $\frac{v_{crit}}{V_v}$ is computed as a function of the clustercentric radius normalized

by the radius of the virialized region. For $r < R_{200}$ the virialized region is predicted by a triangle where the cluster has a dispersion of $\sigma = 0.65 \times \Delta v$ as predicted from hydrodynamical simulations (Mamon et al. 2010; Mahajan et al. 2011).

The red line represents the escape velocity which was projected to the l-o-s velocity by applying the scaling factor of $\sim \sigma_{A3627}/\sqrt{3}$.

The escape velocity is defined as;

$$v_{esc} = \begin{cases} \sqrt{\frac{2GM_{200}}{3R_{200}}K}, & r < R_{200} \\ \sqrt{\frac{2GM_{200}}{3R_{200}s}}, & \text{otherwise} \end{cases}, \tag{3.3.3}$$

where

$$K = g_c \left(\frac{\ln(1+cs)}{s} - \ln(1+c) \right) + 1, \tag{3.3.4}$$

$$s = \frac{r_{3D}}{R_{200}} \sim \frac{\pi}{2} \frac{r}{R_{200}}, \tag{3.3.5}$$

and

$$g_c = \left[\ln(1+c) - \frac{c}{1+c} \right]^{-1}, \tag{3.3.6}$$

and the Norma cluster concentration parameter is $c = 6.2$ (Sivanandam et al. 2010).

Nearly all of the selected cluster members are bound within the escape velocity ($v_{gal} < v_{esc}$). Most HI detections lie within the "infall" region, which suggests that they are entering the cluster for the first time. All of these galaxies have asymmetric morphologies comprising tails in HI. These morphologies could be due to galaxy-galaxy interactions as galaxies fall into the cluster core.

There are 6 HI detections in the virialized region where most optically detected galaxies seem to lie. The virialized population corresponds to the main overdensity in optical and HI velocity distributions in Fig 3.1. HI detected galaxies in the virialized region of the PSD have undisturbed morphologies. However, their HI discs are truncated compared to stellar discs, which indicates that they have spent a long time in the cluster and since lost most of their extraplanar HI and being transformed into galaxies with early-type morphologies. The most likely dominant mechanism that could be responsible for this is RPS.

Therefore, galaxy transformations in the cluster are due to preprocessing by galaxy-galaxy interactions during their transition into the cluster core, as seen by the E/S0 population dominating the core region and eventually by the effects of RPS by the

cluster's ICM, made evident by the gas deficiency and truncated HI gas disks of galaxies in the core region. At the first encounter, galaxies' gas disks become disrupted by the ICM winds. After several encounters, the gas disks are truncated outside-in into symmetrical mass disks of radius r_t.

3.3.2 Galaxy gas stripping

RPS is a gas-only stripping mechanism during galaxy-ICM interactions in the cluster's core. The interaction may occur every time the galaxy encounters the ICM. Each time the galaxy crosses through the cluster centre, it presses against the hot, dense ICM plasma so that the ICM winds push back against the galaxy ISM and truncate the frontal gas disk. The loosely bound gas disk in the galaxy is pushed back, compressed, disrupted, and then stripped (Gunn & Gott III 1972; Jaffé et al. 2018). Steyrleithner et al. (2020) describes two major phases of RPS, such that before the gas is completely stripped, it is first shock-compressed, increasing the SFR. The outer gas disk is then truncated from outside-in to r_t; however if a galaxy survives the instantaneous stripping phase, it loses its gas subsequently due to Kelvin-Helmholtz instabilities occurring at the interface between the gas of the galaxy and that of the ICM (Roediger & Hensler 2005).

The effectiveness of RPS, η, is the ratio of the ICM pressure, P_{ram}, and the restoring gravitational force, Π_{gal}, of the galaxy encountering the ICM (Hernández-Fernández et al. 2014; Jaffé et al. 2015; Ramatsoku 2017; Steyrleithner et al. 2020);

$$\eta = P_{ram}/\Pi_{gal}. \tag{3.3.7}$$

Gunn & Gott III (1972) showed that a spiral galaxy loses its gas when;

$$P_{ram} > \Pi_{gal}, \tag{3.3.8}$$

where

$$\Pi_{gal} = 2\pi G \Sigma_g \Sigma_s, \tag{3.3.9}$$

and

$$P_{ram} = \rho_{ICM} \times v_{gal}^2. \tag{3.3.10}$$

$\Sigma_g = \Sigma_0 e^{-rt(1/R_g)}$ and $\Sigma_s = \Sigma_0 e^{-rt(1/R_s)}$ are the gas and stellar disk surface density profiles respectively, defined by the truncation radius, r_t; and $R_{g,s}$ are scale lengths of

the gas and stellar disks, respectively. The gas and stellar central surface density of the galaxy are $\Sigma_{0,g} = \frac{M_g}{2\pi R_g^2}$ and $\Sigma_{0,s} = \frac{M_s}{2\pi R_s^2}$, respectively (Jaffé et al. 2015).

The ICM gas density is measured based on the standard β-model profile (Cavaliere & Fusco-Femiano 1976);

$$\rho_{ICM} = \rho_0 \left[1 + \left(\frac{r_{3D}}{R_c}\right)^2\right]^{-3\beta/2}, \tag{3.3.11}$$

where ρ_0 is the central ICM density, R_c is the radius of the cluster core from the β-profile and r_{3D} is the radius scaled with the projected r of the particle, i.e., $r_{3D} \sim \frac{\pi}{2} r$ (Jaffé et al. 2015).

We use an MW-type galaxy (Jaffé et al. 2015) to estimate the region in PSD where we would expect the gas disk of this type to be completely stripped, i.e., $r_0 = 0$, in the Norma cluster. The stellar (M_s) and gas (M_g) disk mass of a MW-type galaxy are 4.6×10^{10} $M_\odot$ (Bovy & Rix 2013) and $0.06 \times M_s$ (Sancisi et al. 2008), respectively. The stellar (R_s) and gas (R_g) scale lengths are 2.15 kpc (Bovy & Rix 2013) and $1.7 \times R_s$ kpc (Cayatte et al. 1994), respectively. From the β-model, the Norma cluster has

$\rho_{ICM} = 4.82 \times 10^{-24}$ kg/m^3, $\beta = 0.555$ and $r_c \sim 184$ kpc. The red-shaded area in Figure 3.5 represents the region where a MW-type galaxy gas disk is truncated to $r_t = 0$ kpc. The HI detection limit at the distance to the cluster is $M_{HI,lim} \sim 7.25 \times 10^7$ $M_\odot$, which was calculated for a galaxy of linewidth 200 km/s at the 5σ rms noise level. By computing mass fractions ($f = M_{HI}/M_g$) into the equation (from Jaffé et al. 2015);

$$f = 1 + e^{-\frac{r_r}{R_d}} \left(-\frac{r_r}{R_d - 1}\right), \tag{3.3.12}$$

we get $r_t = 0.909$ kpc.

Galaxies encounter the ICM during the first infall already preprocessed at the outskirts, given their asymmetrical morphologies and the fact that the Norma cluster is an actively merging cluster of galaxies. However, infalling galaxies exhibit asymmetrical morphologies, and virialized galaxies exhibit truncated gas disks, and this means that RPS plays a more significant role in removing ISM gas.

3.4 Gas removal and implications on star formation

Stellar masses are a crucial component for probing internal formation history, morphology and chemical enrichment of galaxies as well as, indirectly, environmental effects

(Hughes et al. 2013; Ibarra-Medel et al. 2016; Belokurov & Evans 2022). This is because stars are formed from dense, cold, shock-compressed molecular gas. This shock compression may be induced by external environmental interactions or major events such as mergers, mass accretion, and even during the gas compression phase of RPS (Courteau et al. 2014; Catinella et al. 2018; Glover & Clark 2012; Blitz & Rosolowsky 2006; Bigiel et al. 2008; Leroy et al. 2008; Krumholz et al. 2009a Krumholz et al. 2009b). Therefore, SF activity and quenching are directly regulated by external interactions, internal dynamics, and how much HI gas is available (Guo et al. 2021). Analysis of stellar and HI masses and their respective mass fractions provides valuable insights into the current SF history (SFH) and the interactions within the surrounding environment.

This section investigates how much of the HI content remains in the detected Norma galaxies given the environmental effects evaluated in section 3.3. This is done by comparing HI mass fractions with those of galaxies in the field. This way, we can examine gas deficiency (DEF_{HI}) and its implications on SFR. This requires ancillary data for physical parameters such as stellar masses ($M_\star$) and SFR.

The necessary ancillary data were obtained from the Wide-field Infrared Survey Explorer (WISE) through private communication with Professor Thomas Jarrett[2]. They are listed in Table 2.2. WISE is a NASA-funded space-based infrared telescope which completed its primary mission to survey the entire sky in the mid-infrared bands at W1 $\sim$ 3.4 μm; W2 $\sim$ 4.6 μm; W3 $\sim$ 12 μm; and W4 $\sim$ 22 μm; wavelengths with minimum 5σ sensitivities of 0.08 mJy, 0.11 mJy, 0.8 mJy, and 6 mJy, respectively (Mainzer et al. 2005; Wright et al. 2010). The imaging bands are sensitive to stellar population and ISM processes, which can be used to study the past-to-present SFH (Jarrett et al. 2012). Objects classification ranges from cool asteroids (Masiero et al. 2014), brown dwarfs (Mainzer et al. 2011), planetary nebulae (Ressler et al. 2010), to the most luminous galaxies in the universe (Eisenhardt et al. 2012). WISE is thus a suitable survey for obtaining information on the stellar properties of galaxies in the Norma cluster.

HI mass fractions were examined by comparing the Norma HI detected galaxies with a sample of galaxies in the field obtained from the extended GALEX Arecibo SDSS Survey (xGASS[3]; Catinella et al. 2018). This field sample comprises deep HI observations, targeting a stellar mass regime dominated by star-forming disks. The sample contains

[2]http://www.ast.uct.ac.za/ast/staff/thomas-jarrett

[3]https://xgass.icrar.org/data.html

1179 galaxies with stellar mass range $10^9 \leq M_\star/M_\odot \leq 10^{11.5}$ at $0.01 \leq z \leq 0.05$, and homogeneously measured optical and SF properties. It has a gas fraction limit of $0.02-0.1$, from galaxies with higher stellar masses ($\log(M_\star/M_\odot) > 9.7$) to galaxies with smaller stellar masses in which they set a constant gas limit of $\log(M_{HI}/M_\odot) = 8$. xGASS is a distinctively convenient gas fraction-limited survey, essential to interpret variations of gas content as a function of galaxy properties.

3.4.1 HI Deficiency

An examination of HI deficiency in the galaxies detected in the Norma cluster is conducted by determining the amount of HI content that was removed due to interactions with the Norma cluster. This is done by comparing the measured HI mass fractions of Norma galaxies with the published mass fractions of a field sample from xGASS.

HI gas mass fraction is defined as in McGaugh & De Blok (1997); i.e.,

$$f_{HI} = \frac{M_{HI}}{M_\star}. \tag{3.4.1}$$

The HI mass fraction as a function of the stellar mass is presented in Figure 3.7, where xGASS and Norma cluster HI detections are plotted. A linear regression was fitted through the xGASS data, and the resulting relation was found to be

$$\log(f_{HI}) \approx -0.606 \times \log(M_\star) + 5.44, \tag{3.4.2}$$

which is consistent with the HI gas mass fraction correlation by Catinella et al. (2018), defined using ordered pairs of weighted averages ($< \log(f_{HI}) >$) for each stellar mass average ($< x >$), where $x = \log(M_\star)$ for number N of galaxies in bin (Table 1 in Catinella et al. 2018). The ordered pairs of weighted averages are indicated by the black circle markers in the figure.

Norma cluster members are classified as having either asymmetrical (diamond-shaped markers) or symmetrical gas disk morphology. A total of 10 cluster members are $0.8-1.2$ dex below the general field population and, therefore, are HI-deficient. Only 2 HI detections are on the line of best fit along the scaling relation of xGASS galaxies, within the limits of their physical parameters, and can be classified as the only "normal" galaxies in the HI sample. As seen in this plot, there is a strong correlation between HI

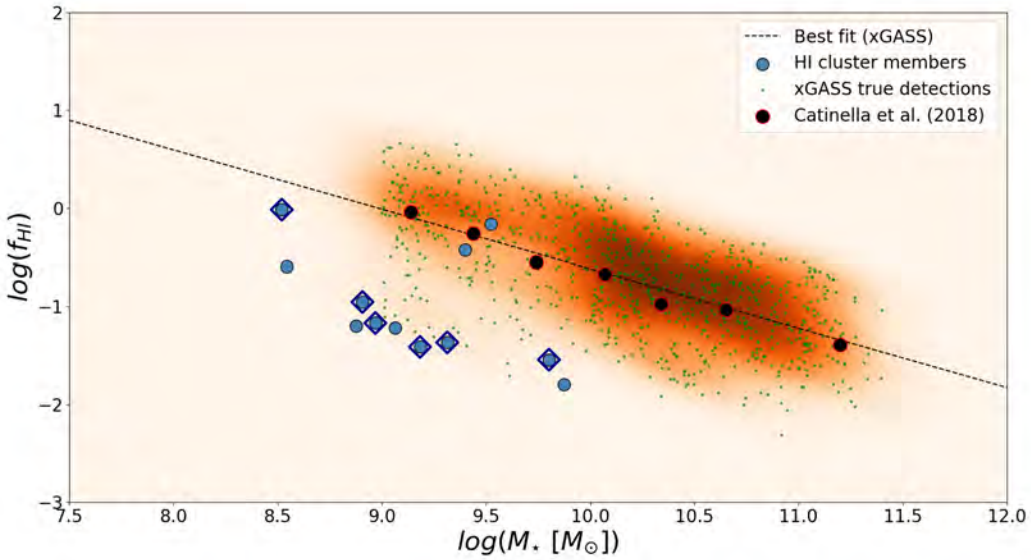

z

Figure 3.7: HI mass fractions of the detected gas disks in the Norma cluster are plotted alongside field galaxies from xGASS. HI cluster members are plotted in blue markers, and those with asymmetrical morphologies are indicated with blue diamond-shaped markers. The density distribution was generated from xGASS galaxies, and the line of best fit is drawn.

deficiency and galaxy HI morphology, such that the HI-deficient galaxies all appear to have asymmetrical morphologies.

3.5 Star formation rates

As discussed in section 3.3, RPS appears predominantly to have been the process responsible for asymmetrical morphologies and now the observed gas deficiency.

Gas-rich spirals grow by intrinsically building their disks through SF processes, which involve consuming HI gas, converting it into HII, combined with interstellar dust in dense cool molecular clouds. These SF processes (star-bursts to low SFR over periods of time) eventually result in IR-luminous galaxies with prominent bulges (Cluver et al. 2014; Rafieferantsoa & Davé 2018; Jarrett et al. 2019). It is not clear whether it is gas consumption during SF coupled with starvation as well as external stripping mechanisms (Bekki et al. 2002; Fumagalli & Gavazzi 2008; Boselli et al. 2009; Trussler et al. 2020),

or the shutdown of the supply of cold gas during outflows driven by AGN feedback (strangulation: e.g., de Gouveia Dal Pino et al. 2018; Cicone et al. 2018 de Gouveia Dal Pino et al. 2018; Shin et al. 2019), or a combination of these parameters that trigger the decline of SF activity (Gabor et al. 2010; Combes 2018; Hopkins et al. 2008; Kormendy et al. 2009). It has been shown that the shut-down of SF activity due to environmental interactions is efficient at $z < 1$ for all galaxy masses (Lee & Cosmos Team 2015).

In subsection 3.4.1, we demonstrated that most of the HI detected galaxies in the Norma cluster are HI-deficient compared to the field galaxies. We previously discussed in section 3.3 that RPS appears to be the dominant process driving this deficiency. In this section, we will study the SF activity under the environmental effects of the Norma cluster.

3.5.1 Colour properties of HI detections

WISE imaging bands were used to determine the detected galaxies' SF properties qualitatively. This is because these bands are sensitive to the byproducts of SF activity in molecular clouds, which can be used to indirectly study both SFH and current SFRs (Jarrett et al. 2013; Jarrett et al. 2017).

The W1 band is the most sensitive to stellar light and is used to characterize stellar generations (reaching depths of $z \sim 0.5$), while the W2 band is sensitive to hot dust and can be used to characterize cool to warm dusty ISM. Both bands are not affected by extinction and predominantly trace the continuum emission from evolved stars (Pahre et al. 2004; Jarrett et al. 2011; Meidt et al. 2012). Galaxies with warm AGN emission can be detected at $\mathrm{W1} - \mathrm{W2} \geq 0.8$ mag (Stern et al. 2012a; Stern et al. 2012b), while some Seyferts lie below this line (Jarrett et al. 2011; Stern et al. 2012b). Stars lie at even lower $\mathrm{W1} - \mathrm{W2}$.

$\mathrm{W2} - \mathrm{W3}$ describes sources according to their physical properties and can draw the distinction between warm and cool clouds. Star-forming galaxies have higher $\mathrm{W2} - \mathrm{W3}$ (Cluver et al. 2014). The $\mathrm{W2} - \mathrm{W3} < 1.5$ mag colour regime describes early-type spheroids, characterized by notable bulges with older stellar generations dominating the mid-IR emission, which makes these galaxies massive and bright in mid-IR, with very little efficiency in current SF activity (Jarrett et al. 2013; Jarrett et al. 2017; Jarrett et al. 2019). Objects with $\mathrm{W2} - \mathrm{W3} \sim 1.5 - 3$ mag are intermediate disks. These sources have the largest spread in surface brightness and are intermediate between the

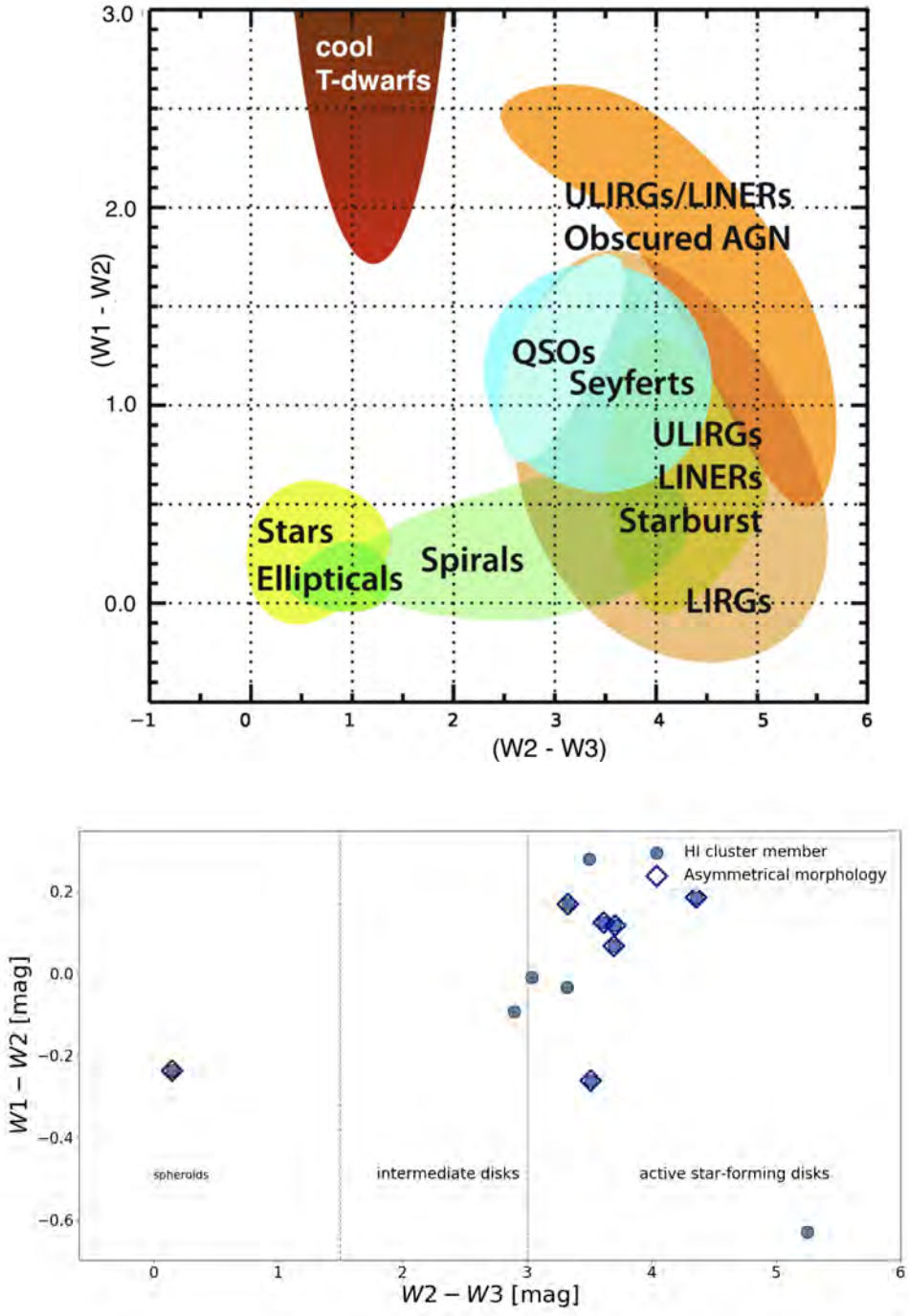

Figure 3.8: WISE colour–colour diagram on the top panel mapping regimes of different classes of objects (Banfield et al. 2015; Wright et al. 2010) and the WISE colour-colour plot for the detected HI gas disks on the bottom panel, delineating galaxies into passive-SF spheroids, intermediate and active SF disks (Jarrett et al. 2011).

passive and star-forming galaxies. Active star-forming disks have W2 − W3 ≥ 3 mag.

In Figure 3.8 the WISE colour-colour diagram in the top panel shows the different

regimes of different classes of objects, and in the bottom panel Norma cluster HI detections are plotted in the WISE colour-colour diagram, with the vertical lines dividing between the quiescent spheroids, intermediate disks, and the active star-forming disks.

In the sample, only one galaxy is a quenched spheroid, and only one is an intermediate disk. A total of 10 ($\sim 83\%$) cluster members detected in HI fall in the active star-forming regime, and these are the brightest, late-type star-forming disks, with dust and some HI content still remaining, and continue building their stellar disks.

As shown in Figure 3.8 most of the HI detections are in the range $W2 - W3 \sim 2.89 - 5.25$ mag (mean $W2 - W3 = 3.66$ mag). These detections have dusty molecular surfaces. The observed stellar light from such dusty surfaces gets absorbed and re-emitted by dust to obscure the optical light. This class of dusty star-forming galaxies (DSFGs) is normally expected to undergo periods of intense SF (Martis 2020).

3.5.2 The gas content and star formation of main sequence galaxies

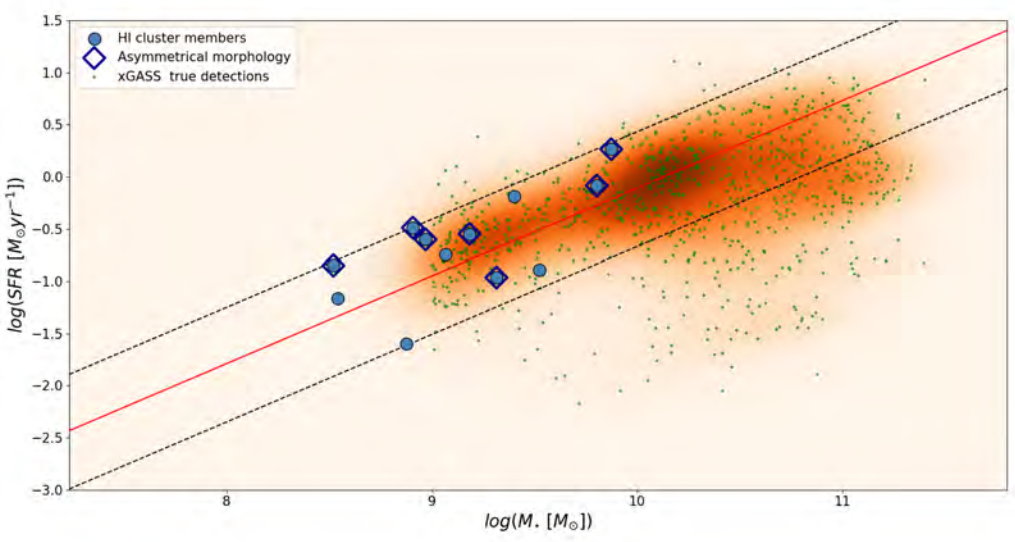

Figure 3.9: The star formation rate as a function of stellar mass. The red linear regression line was generated for xGASS galaxies and is defined by $\log(\mathrm{SFR}) = 0.84 \times \log(\mathrm{M}_\star) - 8.51$. The black dotted lines indicate the spread from the red linear regression line, which is $\log(\mathrm{SFR}/\mathrm{M}_\odot \mathrm{yr}^{-1}) \sim 0.6$.

Since most of the cluster members are active star-forming disks, regardless that they

appear to be HI-deficient, it is fitting to quantify their SF efficiency by comparing their SFR with those of the field galaxies in the control sample (xGASS). This is presented in Figure 3.9. In this plot, SFR is presented as a function of stellar mass. The xGASS galaxy number density distribution presents a strong positive correlation between SFR and stellar masses in that the higher the stellar mass, the higher the SFR of galaxies at a given stellar mass. Norma cluster HI detections follow this positive trend, with most ($\sim 83\%$) of the detections showing a slight offset towards higher SFR than the average xGASS population. There are 4 galaxies at low stellar masses ($\log(M_\star/M_\odot) < 9$). These lie outside the stellar mass range of the control and cannot be used in the comparison. However, they do not change the general trend seen. Moreover, there appears to be a correlation for the HI detections that are slightly offset from this average xGASS population since they also show signs of asymmetries. A total of 10 ($\sim 83\%$) HI detections have higher SFR in the distribution, and asymmetrical gas disks make up this population along the inclination.

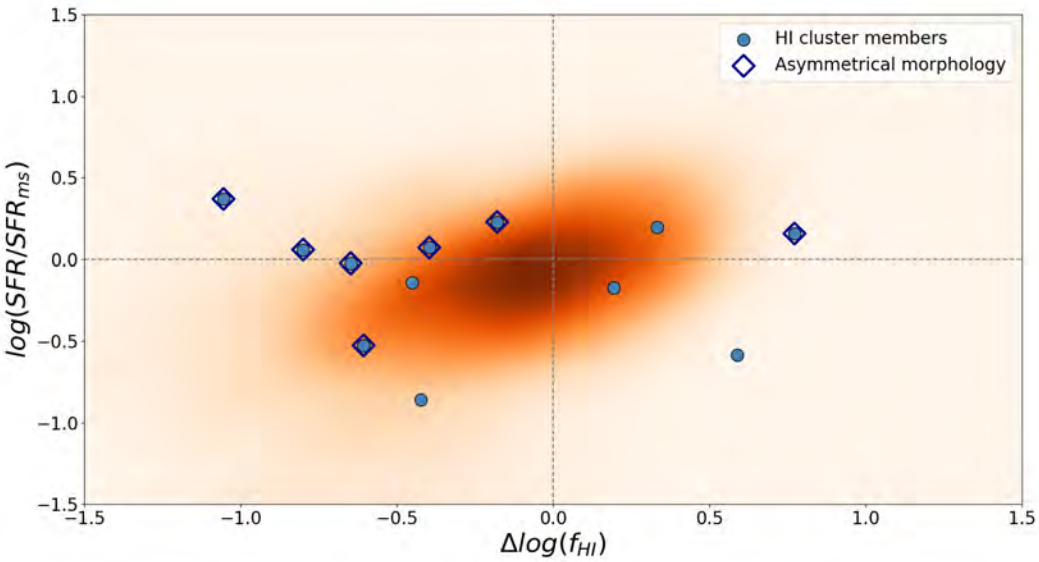

Figure 3.10: Star formation efficiency of Norma cluster galaxies in comparison to main sequence galaxies (SFR/SFR_{ms}), is plotted against HI gas fraction deviation from the xGASS scaling relation for galaxies in the field ($f_{HI}/f_{HI,ms}$). The orange density maps are xGASS field galaxies. As before, asymmetrical gas disks are indicated with diamond markers.

In Figure 3.9, we found that stellar mass is the primary parameter that determines SF and, to some extent, the gas properties of galaxies. Therefore, it is essential to take it into consideration when examining galaxies with a wide range of stellar masses, such as those in the Norma cluster. In Figure 3.10 we examine SFR/SFR_{ms} as a function of $f_{HI}/f_{HI,ms}$.

The deviation of the observed SFR from the SFR of main sequence galaxies (SFR_{ms}) is computed from the equation;

$$\log(SFR/SFR_{ms}) = \log(SFR) - \log(SFR_{ms}), \tag{3.5.1}$$

where SFR_{ms} is defined by Saintonge et al. (2016) as;

$$SFR_{ms} = -2.332 \times x + 0.4156 \times x^2 - 0.01828 \times x^3, \tag{3.5.2}$$

where $x = \log(M_\star)$. Similarly, the deviation of the observed mass fractions from mass fractions of main sequence galaxies is derived from the following;

$$\Delta\log(M_{HI}/M_\star) = \log(M_{HI}/M_\star) - \log(M_{HI}/M_\star|_{ms}), \tag{3.5.3}$$

where $\log(M_{HI}/M_\star|_{ms})$ is computed from the line of best fit in Figure 3.7 as;

$$\log(f_{HI}|_{ms}) \approx -0.6060 \times \log(M_\star) + 5.4438. \tag{3.5.4}$$

In Figure 3.10, the xGASS population is positioned around the point of origin, however, slightly exhibiting a positive correlation. This means field galaxies with excess SFR at their stellar mass appear to have an excess amount of HI and vice verse. The Norma cluster HI detections appear to be mostly concentrated in the second quadrant, showing deficiency in gas fractions and excess SFR from predictions at their stellar masses. They are HI-deficient but show enhanced SFR for their stellar mass. This is uncommon in the field where only a small percentage ($\sim 15\%$) are in this quadrant.

There appears to be a correlation between HI morphology and enhanced SFR for galaxies that are experiencing RPS for the first time. It seems that when galaxies enter the cluster for the first time, they show enhanced SFR for their HI content. This could be due to gas compression during the initial phase of RPS. This has been observed in massive galaxy clusters similar to the Norma cluster, such as the massive and rich Coma cluster with similar characteristics as the Norma cluster (e.g., Kenney et al. 2015; Gavazzi et al. 2018; Chen et al. 2020; Roberts & Parker 2020a; Lee et al. 2022a; Molnár et al. 2022).

For example, in Molnár et al. (2022), they find that $\sim 75\%$ of HI-selected Coma galaxies have simultaneously enhanced SFR and are HI-deficient compared to field galaxies of the same stellar mass. RPS may trigger this before quenching. Roberts & Parker (2020b) compared a sample of 41 ram-pressure stripped candidates in the Coma cluster to an isolated field sample from the SDSS catalogue (Roberts & Parker 2017). They found that ram-pressure stripped candidates in the Coma cluster on the first infall towards the cluster centre show evidence for morphological asymmetry and enhanced SFR. In Upadhyay et al. (2021), they use a sample of 11 high-SNR early-type galaxies around the Coma cluster and find that galaxies in the sample are likely to have formed nearly all of their stellar mass by the time of their first pericentric passage and that it is likely that these galaxies quenched within 1 Gyr after, losing substantial amounts of gas in the process. These results are consistent with studies by Chen et al. (2020), who use high spatial resolution VLA HI and 1.4 GHz continuum data on 20 ram-pressure stripped galaxies in the Coma cluster. In Lee et al. (2022b), they find that "starburstiness" ($\mathrm{SFR/SFR_{ms}}$) of ram-pressure stripped jellyfish galaxies show positive correlations with cluster velocity dispersion, ICM density, and strength of RPS. This may mean that such occurrences are more likely to occur in massive, X-ray bright clusters.

The results in this work are consistent with the preceding studies. It would seem that ram-pressure-stripped galaxies are characterized by the gas being pushed on one side during the initial phase and eventually stripped by the ICM. SF is likely enhanced at the initial phase.

Chapter 4

Summary

In this chapter, we summarise the main results of the study conducted in the thesis.

This project aimed to use the properties of the HI gas to study galaxy evolution in the dense environments of the Norma cluster. The Norma cluster has remained mainly unexplored due to its location at low galactic latitudes. This project was conducted to (i) examine pre-processing from an HI perspective as a function of galaxies' location within the cluster, in which we use deep MeerKAT HI data in combination with ancillary data from WISE; (ii) search for HI tails in spatially resolved HI detections to quantitatively characterise and study the detailed morphologies of HI in galaxies as a function of their distance from the cluster centre; (iii) probe SF efficiency in the harsh Norma cluster environment, thereby investigating SFR and its connection to HI consumption.

4.1 MeerKAT observations of the Norma galaxy cluster

An HI study of the Norma cluster was conducted using data from MeerKAT. The Norma galaxy cluster is located in the core of the GA, near the galactic plane at $(\mathrm{RA}, \mathrm{Dec}) \sim (243.59°, -60.88°)$, with an Abell radius of $\mathrm{R_A} = 2.02$ Mpc. It is a rich, massive and nearby cluster at 67 Mpc (using $\mathrm{H_0} = 73$ km/s/Mpc) with a dynamical mass of $\mathrm{M_{dyn}} \sim 1 - 1.1 \times 10^{15}\ \mathrm{h_{73}^{-1} M_\odot}$, at a redshift of $cz_{\mathrm{A3627}} \sim 4871$ km/s in the radial velocity range of 2096 km/s $< \mathrm{v_{A3627}} <$ 7646 km/s, and exhibits a velocity dispersion of $\sigma_{\mathrm{A3627}} \sim 925$ km/s.

To complete multi-wavelength (optical, X-ray, NIR) studies of this massive structure, the Norma cluster was observed in HI for three reasons. First, the gas disk of a galaxy is

far more extended and loosely bound than the stellar disk, making it more sensitive to environmental effects. Secondly, HI is the gas reservoir which cools into molecular clouds where SF activity occurs (at a high column density of 10^{22} cm^{-2}). So, the amount of HI supply may ultimately set the rate of SF activity. Lastly, the Norma cluster is located behind the MW galaxy, where there is obscuration due to large clouds of interstellar cosmic dust, which makes it hard to observe galaxies in optical wavelengths. The HI emission line has properties that make it useful to detect gas-rich galaxies behind the MW since dust is transparent at this long radio wavelength.

The Norma cluster was observed in HI in the L-band with the MeerKAT telescope. The MeerKAT HI datacube used has 243 spectral channels that are ~ 44.1 km/s wide, with a velocity range of $483 - 11,113$ km/s. The field of view is $\sim 2^\circ \times 2^\circ$, with a pixel scale of $2''$. The noise in the cube is $\sigma = 0.09$ mJy/beam. The beam size is $\sim 14.64'' \times 9.28''$ and the position angle is PA $= 146$ deg. This enabled the detection of HI gas disks in the cluster to an HI mass limit of $M_{HI,lim} = 7.25 \times 10^7$ $M_\odot$, assuming galaxy linewidth of 200 km/s at 5σ. The source finding application (SoFiA) was used to search for HI line emission in the cube. A total of 31 sources were detected in HI. Of these, 25 were verified as real detections based on visual inspection.

The properties extracted from these detections include HI masses in the range $\log(M_{HI}/M_\odot) \sim 7 - 10$, and linewidth range $w_{50} \sim 66 - 1080$ km/s. Galaxies were detected within a velocity range of $\sim 604 - 10,353$ km/s. Their velocity distribution showed 3 main overdensities, two associated with the Norma cluster at $\sim 2000 - 8000$ km/s, and the other in the background at $\sim 10,000$ km/s. Of the galaxies detected, 9 (36%) were found to have at least one optical counterpart from previous surveys.

We computed A_p for galaxies that are spatially resolved across the major axis in the column density map and exhibit an HI sensitivity of $N_{HI} \sim 1.5 - 3.1 \times 10^{20}$ cm^{-2}, corresponding to SNR in the range $2 - 3\sigma$ in the outer regions of the HI disk. The A_p parameter could not be measured reliably for galaxies with low spatial resolution. We used the spectral profiles' skewness and kurtosis to estimate these galaxies' asymmetry. A total of 13 galaxies have asymmetrical morphologies with 9 measured from A_p and 4 from their spectral profiles.

4.2 HI properties of the Norma cluster

A total of 130 optical and 13 HI galaxies were selected as cluster members within the field $2/3 \times R_A$ and the velocity range of $\sim 2000 - 8000$ km/s. The distribution revealed two overdensities in the velocity range encompassed by the Norma cluster, suggesting the presence of substructures within the cluster's volume.

The detected galaxies span the entire mass range $\log(M_{HI}/M_\odot) \sim 7.6 - 10$, with HI mass mean of ~ 8.6 (in log scales). Most detections with higher HI masses $(\log(M_{HI}/M_\odot) \geq 7.8)$ were detected at $v_{rad} \sim 10,000$ km/s. All but one detection have "normal" linewidths in the range $w_{50,corr}) \sim 66 - 392$ km/s. However, all the spirals have the widest linewidths ($w_{50,corr} \sim 240 - 392$ km/s); 78% of the ellipticals (E, E5) have narrow linewidths in the range $w_{50,corr} \sim 66 - 161$ km/s, followed by three lenticulars (S0 and SA0) with linewidths in the range $w_{50,corr} \sim 153 - 199$ km/s. The irregulars and peculiars (Irr and Pec) have linewidths in the range $w_{50,corr} \sim 147 - 237$ km/s.

The spatial distribution of 13 HI and 130 optical, together with the elongated ICM structure in X-ray, confirm the elongated substructure revealed from optical studies. The spatial distribution reveals that $\sim 69\%$ of HI gas disks are positioned at the outskirts. The density in the distribution of optical galaxies increases towards the central region, where fewer galaxies were detected in HI. Moreover, galaxies in the central regions are predominantly ellipticals and lenticulars with intermediate to narrow linewidths.

This HI deficiency in the cluster's core strongly indicates that some gas removal process has occurred. The possible gas removal mechanism could be preprocessing at the outskirts and/or RPS, given that no HI detections were found where a strong peak in the X-ray can be seen. Furthermore, detections with asymmetrical morphologies are distributed just outside the mapped ICM, while the detections with truncated gas disks (narrow linewidths) are located in the central regions.

4.3 Environmental effects

There were hints of gas deficiency when investigating HI products as a distance function to the cluster centre. We used the PSD to trace orbital histories along "infall", "stripping", "backsplash", and "virialised" regions to gain hints into how the cluster en-

vironment shaped the detected galaxies.

Most of the HI detections are in the gravitational potential ($v_{gal} < v_{esc}$) of the Norma cluster. They lie within the "infall" region, suggesting they are entering the cluster for the first time. These galaxies have asymmetric morphologies comprising tails in HI. These morphologies could be due to galaxy-galaxy interactions as galaxies fall into the cluster core. There are 6 ($\sim$ 46%) gas disks detected in the virialized region where most optically detected galaxies seem to lie. The virialised population identifies with the substructure in the central region. The substructure appears to have undisturbed morphologies. However, their gas disks are truncated compared to stellar discs, which indicates they are at advanced stages of gas removal.

From this, we infer that, although infalling galaxies likely reach the cluster core after being preprocessed by galaxy-galaxy interactions, RPS predominantly transforms HI gas disk morphology, eventually causing asymmetrical mass distribution ("lopsidedness") in the gas disk at the first encounter. This is because, during galaxy-ICM interaction and before the gas is completely stripped, it is first pushed to one side and becomes shock-compressed. The outer gas disk is then truncated from outside-in to r_t when the galaxy is eventually virialised.

4.4 Gas deficiency and enhanced star formation efficiency

We investigated how the environment could have affected the SF activity of the detected galaxies. We first start by examining how much HI content remains in the galaxies given the gas removal effects they have experienced. Later, we examine their SF efficiency (SFR/SFR_{ms}) as a function of "how much gas was lost" ($f_{HI}/f_{HI,ms}$). This is conducted with WISE data for measurements of stellar masses, SFR and the WISE colours ($W1 - W2$ and $W2 - W3$).

To investigate galaxies' remaining gas content, we assess HI mass fractions as a function of stellar mass and compare Norma detections with 1179 field galaxies from the xGASS sample. We show that $\sim$ 69% of cluster members are HI-deficient by $0.8 - 1.2$ dex. Furthermore, there is a strong correlation between gas disk morphology and gas deficiency since all HI cluster members with asymmetrical morphologies have the same gas deficiency of $0.8 - 1.2$ dex.

In studies of SF activity under the environmental conditions of the Norma cluster, different classes of objects can be easily divided when plotted with W1 − W2 as a function of W2 − W3. Therefore use the WISE colour-colour diagram to delineate between star-forming and non-star-forming disks, dusty and stellar disks, and between early-types and late-types. In the WISE colour-colour diagram, we show that $\sim$ 83% of cluster members detected in HI fall in the active star-forming disks regime and that $\sim$ 86% of them have asymmetrical morphologies. These are the brightest, late-type galaxies, with star-forming gas and dust to continue building their disks and stellar bulges.

To investigate how the SFR proceeded given the remaining HI content, we report that both xGASS and Norma cluster detections show the same positive correlation and $\sim$ 86% of the asymmetrical gas disks have higher SFR in the distribution.

Finally, we plot the SFR deviation of the observed Norma cluster galaxies from HI scaling relations (SFR/SFR_{ms}) as a function of HI gas fraction deviation of the observed Norma cluster galaxies from main sequence galaxies ($f_{HI}/f_{HI,ms}$). We realise that asymmetrical galaxies are found to have low HI fractions but excess SFR. This indicates that their SF is enhanced given the HI content. We argue that these results may be due to encounters with the harsh ICM environment. Such results were recently observed in the Coma cluster, which is of similar mass and size to the Norma cluster. However, an open question still remains: Is the enhanced SFR due to RPS found in all clusters or just the massive ones?

Serra et al. (2023) found that RPS is more effective when galaxies are preprocessed through gravitational interactions at the outskirts. Using the MeerKAT Fornax Survey with significantly high angular resolution compared to previous observations, they found six late-type spiral galaxies exhibiting long, one-sided HI tails radially oriented with the ICM wind, suggesting the effects of RPS after preprocessing. The tidal-then-ram pressure mechanism provides a plausible explanation for the observed properties of the HI asymmetries in the Norma cluster.

Two points are worth noting: (i) a few galaxies in the central region of the cluster seem to have small HI disks and are relatively not HI-deficient. We assume the gas may have been compressed due to several environmental interactions. (ii) Assuming that the galaxies in the region $\sim$ 3000 km/s are at the Hubble distance, they are not in the in-fall region but more than 15 Mpc from the cluster centre. This group may truly be a

foreground group. Therefore, the asymmetries would more likely be due to gravitational interactions than RPS.

In that case, the distance to the cluster should be used for HI masses, making them less HI-deficient. This would depict a scenario in which galaxies approach the centre, initially developing asymmetric tails and enhanced SFR and only later becoming HI-deficient. Thus indicating environmental pre-processing in action.

Chapter 5

Future prospects

5.1 The Norma cluster future research prospects

The Norma cluster presents an exciting opportunity for future research that goes beyond the scope of this thesis. By conducting deep, high-resolution MeerKAT observations in combination with multi-wavelength data, including resolved optical images, CO emission and X-ray, more detailed studies can be done on intriguing individual cluster members and the background group at $v_{rad} \sim 10,000$ km/s. These potential investigations could add to our understanding of galaxy evolution, cluster dynamics, and environmental effects on galaxies within and around the Norma cluster.

5.1.1 Peculiar velocities

The key to conducting comprehensive HI studies of galaxy dynamics in the Norma cluster lies in obtaining redshift-independent distance measurements achieved through distance indicator relations such as the IR Tully-Fisher relation (Tully & Fisher 1977). The IR Tully-Fisher distance estimator is a technique used to estimate the distances to galaxies based on the correlation between their IR luminosity and the observed velocity width at 20% of the peak flux (w_{20}) of HI emission. In the IR Tully-Fisher relation, the absolute magnitude in the NIR K-band (M_K) is related to w_{20} of the HI emission line as follows:

$$M_K = a + b \times \log(w_{20}), \tag{5.1.1}$$

where a and b are the constants that depend on the specific dataset and calibration used. The IR Tully-Fisher relation is derived from the understanding that the intrinsic

brightness of a spiral galaxy in the NIR is related to its rotational velocity, which can be approximated using the velocity width of the HI emission line. The method provides a relatively straightforward way to estimate the distances to spiral galaxies without relying on individual stars or other distance indicators. One of the advantages of the IR Tully-Fisher distance estimator is that it is less affected by dust extinction compared to optical distance indicators, which can be particularly advantageous when studying galaxies that are heavily obscured by dust.

5.1.2 Preprocessing

Using the deep MeerKAT HI data in combination with ancillary data (WISE) offers the opportunity to study the effects of galaxy pre-processing on the HI properties when studied as a function of galaxies' location within the cluster. Exploring their kinematics and spatial distribution could provide valuable information about the cluster's impact on individual galaxies. Deep, spatially, and spectrally resolved observation would allow us to study the gas kinematics of the galaxies. This could be combined with the kinematics of the stellar components of the galaxies. Combining the two would offer insights into the pre-processing of the galaxies before infalling into the cluster, particularly the tidal-then-ram pressure scenario.

5.1.3 Ram-pressure stripping: a multi-wavelength approach

To conduct a more definitive examination of the dominance of RPS in galaxy clusters, we need HI observations and matching X-ray, optical, and infrared observations from the least to the most massive X-ray bright nearby clusters. Multi-wavelength imaging of sources in such cluster catalogues should also be conducted to characterize their morphology in the optical, quantify asymmetries in the ISM gas disk, and quantify scale lengths of the gas disk compared to the stellar disk. Multi-phase observations of tails in such samples will also need to be observed to test for shock fronts, one-sided SF, HI asymmetry and deficiency, and all other signatures of ram-pressure stripped galaxies, to examine SF efficiency (SFR/SFR_{ms}) and characterize gas compression phase from stripping phase as a function of orbital histories. SF history of ram-pressure stripped galaxies needs to be examined during preprocessing in the field, first infall into pericentric orbit and backsplash. Surveys such as the MeerKAT Galaxy Cluster Legacy

Survey (MGCLS; Knowles et al. 2022), which is a MeerKAT L-band ($900 - 1670$ MHz) observations of 115 galaxy clusters, are ideal for such future studies in this field.

Appendix A

Appendix

A.1 HI channels maps

We plot channel maps of the Norma HI datacube in Figure A.1. The channel maps are shown at every ninth channel. The blanked region seen in the centre of the cube is due to an incomplete continuum of the strong radio galaxies ESO137-006 and the head-tail ESO137-002 (see Ramatsoku et al. 2020).

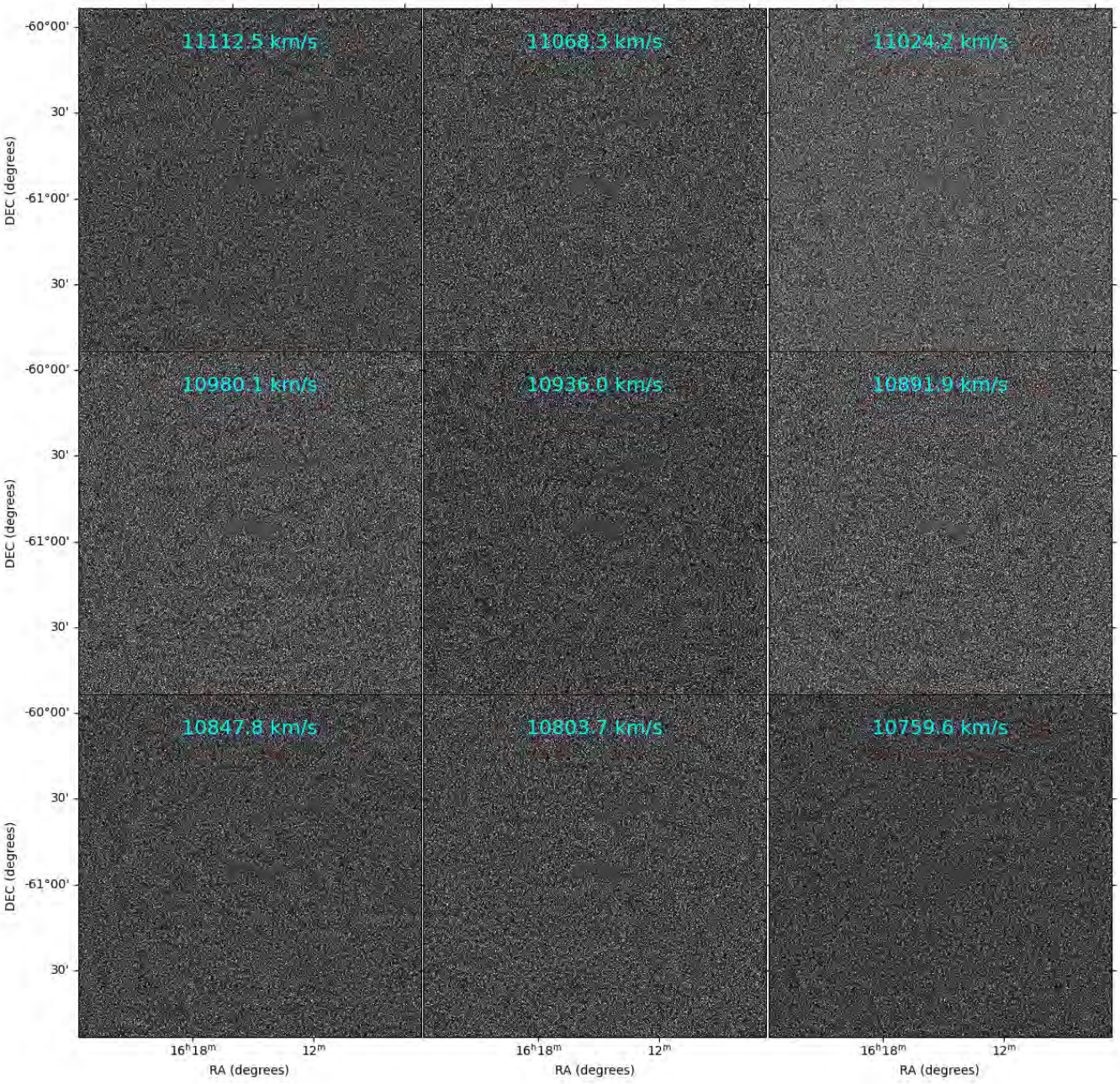
11112.5 km/s
11068.3 km/s
11024.2 km/s
10980.1 km/s
10936.0 km/s
10891.9 km/s
10847.8 km/s
10803.7 km/s
10759.6 km/s
-60°00'
30'
-61°00'
30'
DEC (degrees)
16h18m
12m
RA (degrees)

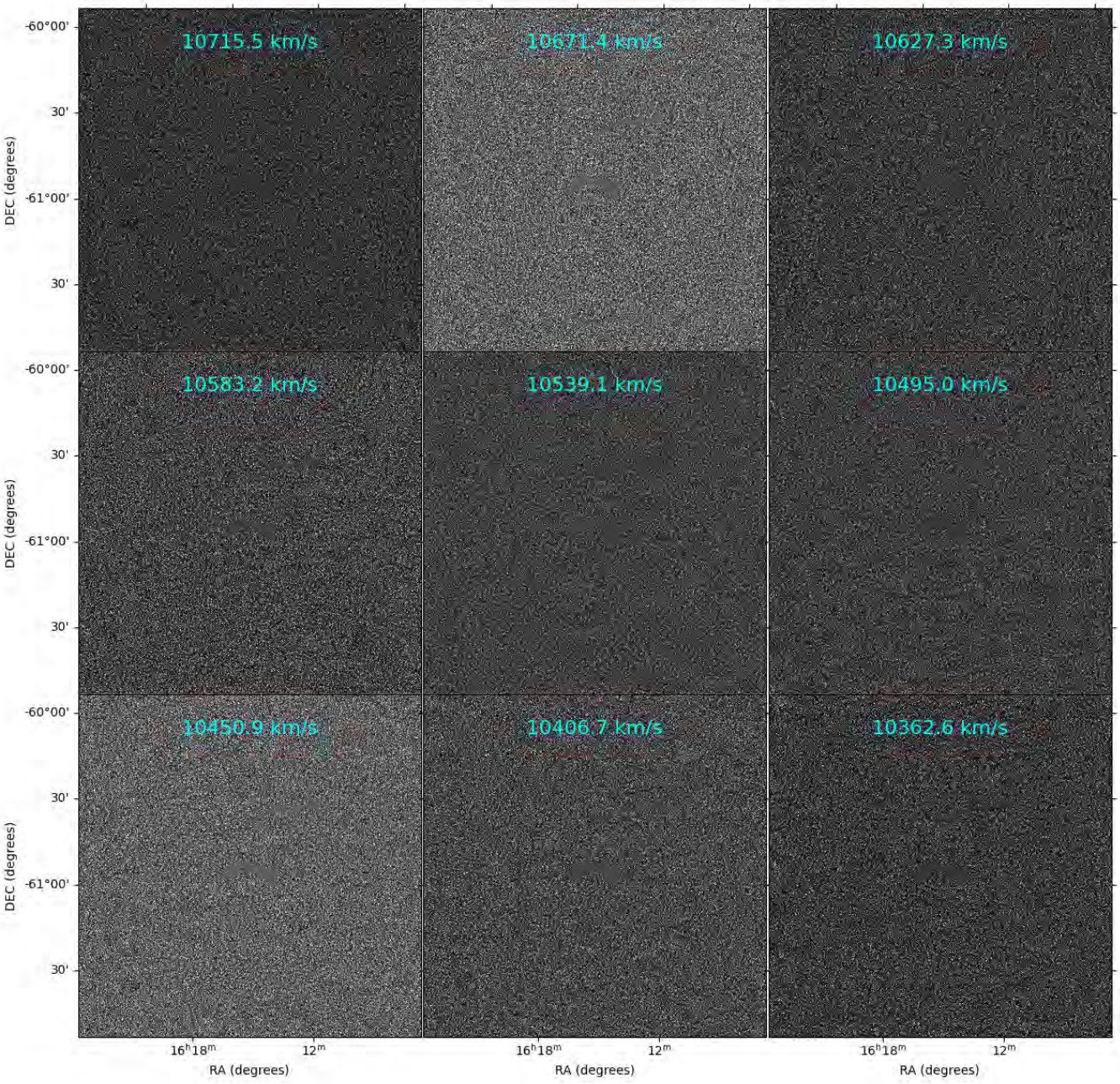
10715.5 km/s
10671.4 km/s
10627.3 km/s
10583.2 km/s
10539.1 km/s
10495.0 km/s
10450.9 km/s
10406.7 km/s
10362.6 km/s
-60°00'
30'
-61°00'
30'
DEC (degrees)
16h18m
12m
RA (degrees)

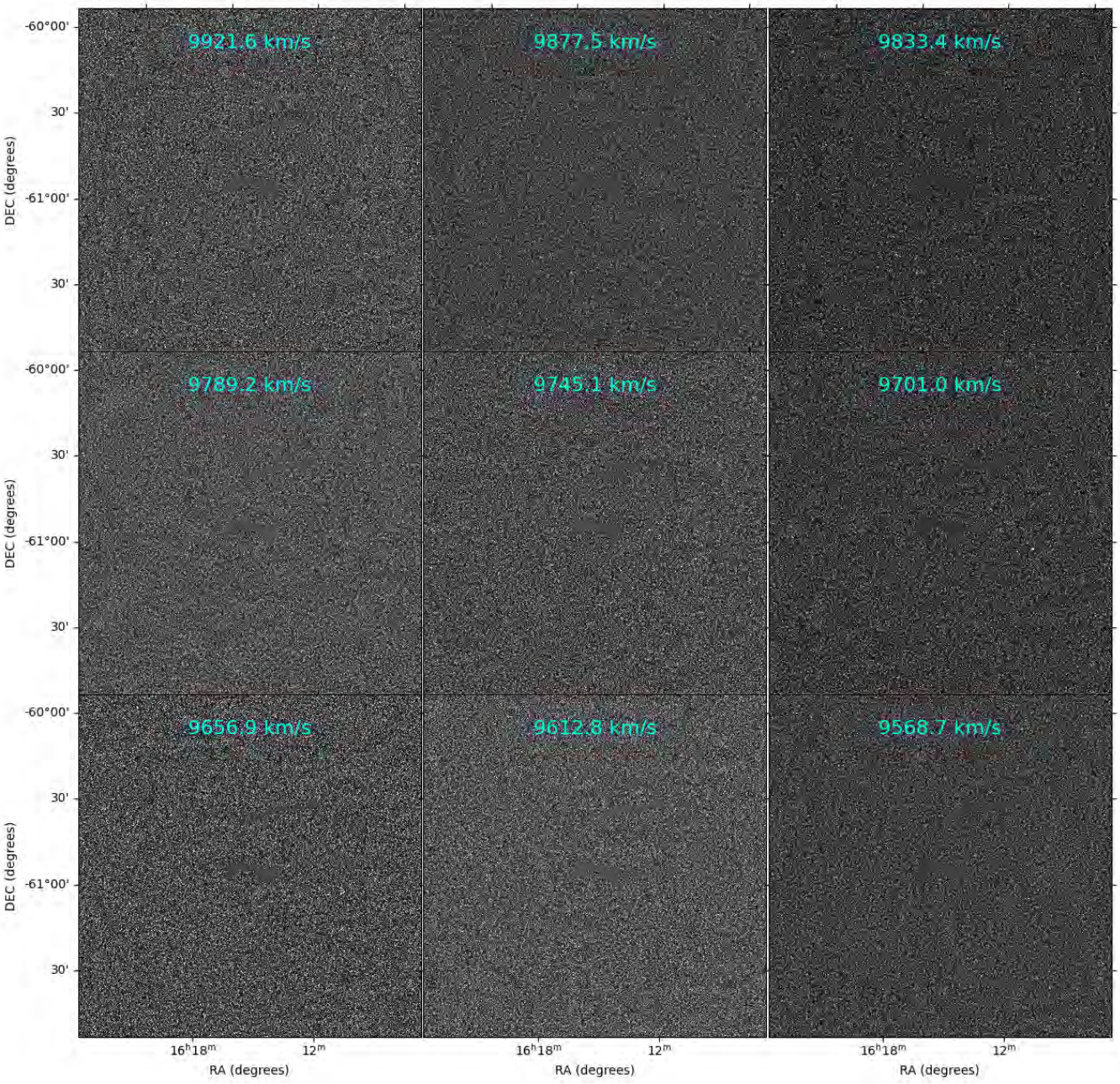
9921.6 km/s
9877.5 km/s
9833.4 km/s
9789.2 km/s
9745.1 km/s
9701.0 km/s
9656.9 km/s
9612.8 km/s
9568.7 km/s
-60°00'
30'
-61°00'
30'
DEC (degrees)
16h18m
12m
RA (degrees)

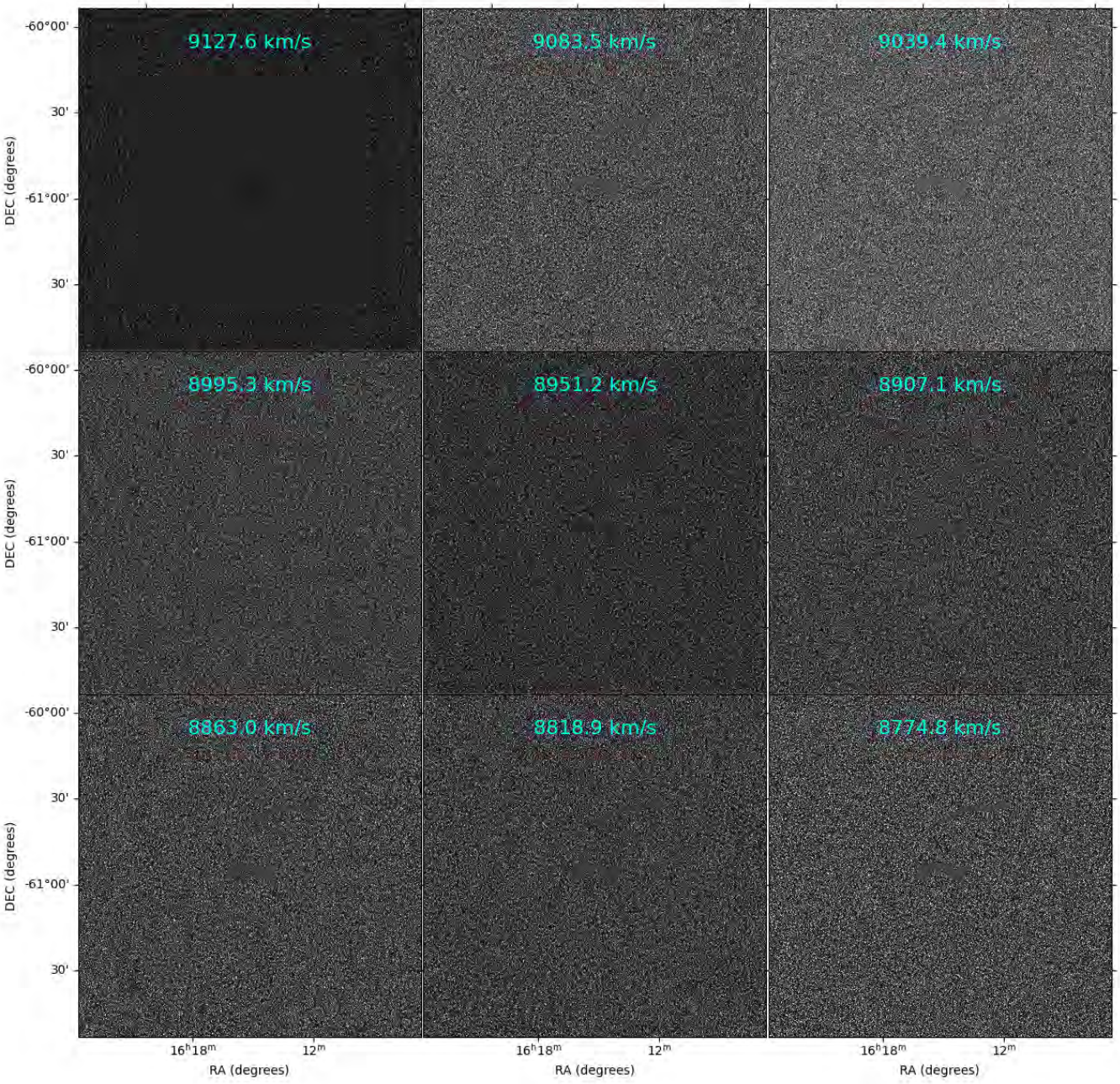
9127.6 km/s
9083.5 km/s
9039.4 km/s
8995.3 km/s
8951.2 km/s
8907.1 km/s
8863.0 km/s
8818.9 km/s
8774.8 km/s
-60°00'
30'
-61°00'
30'
DEC (degrees)
16h18m
12m
RA (degrees)

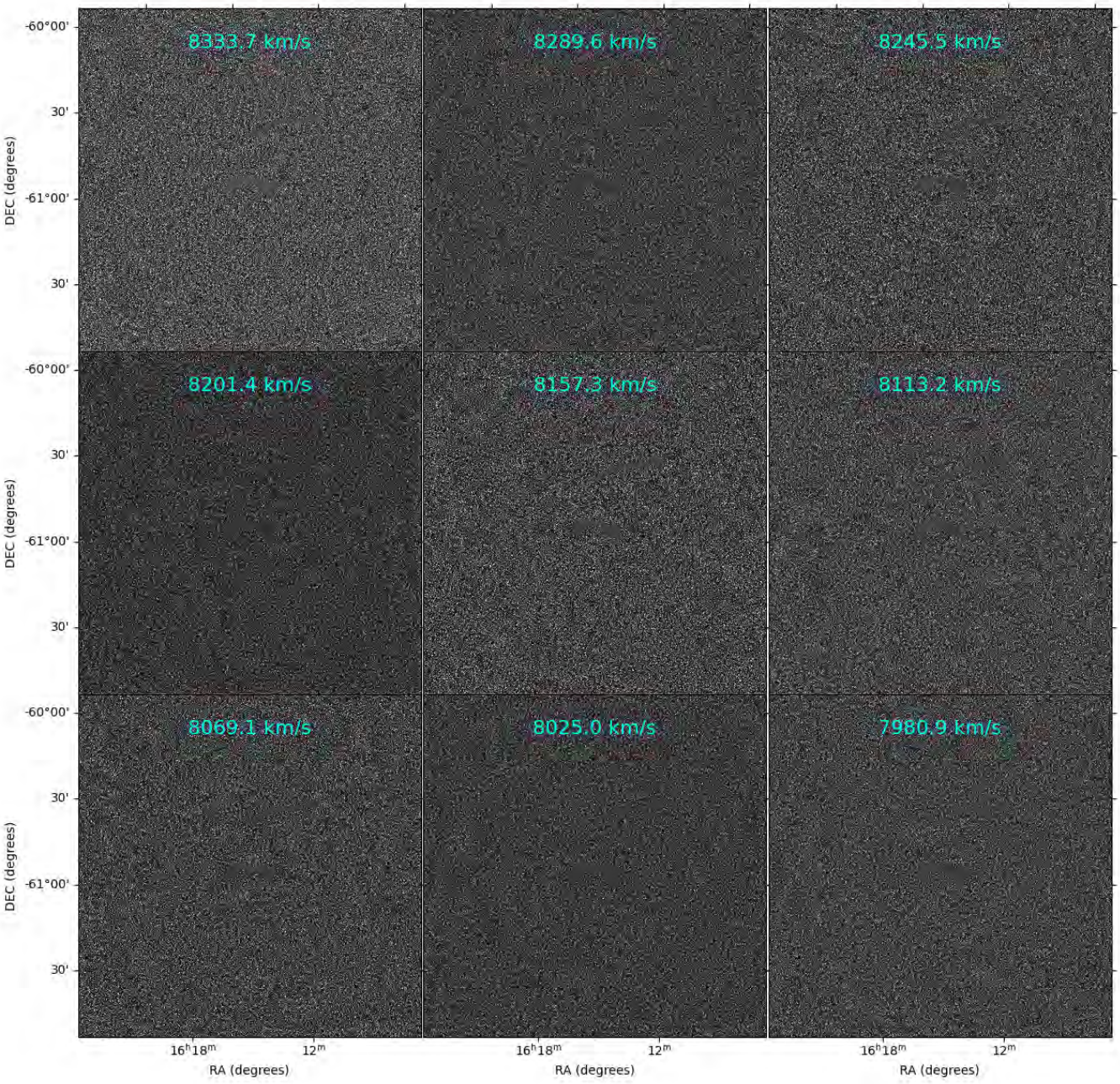
8333.7 km/s
8289.6 km/s
8245.5 km/s
8201.4 km/s
8157.3 km/s
8113.2 km/s
8069.1 km/s
8025.0 km/s
7980.9 km/s
-60°00'
30'
-61°00'
30'
DEC (degrees)
16h18m
12m
RA (degrees)

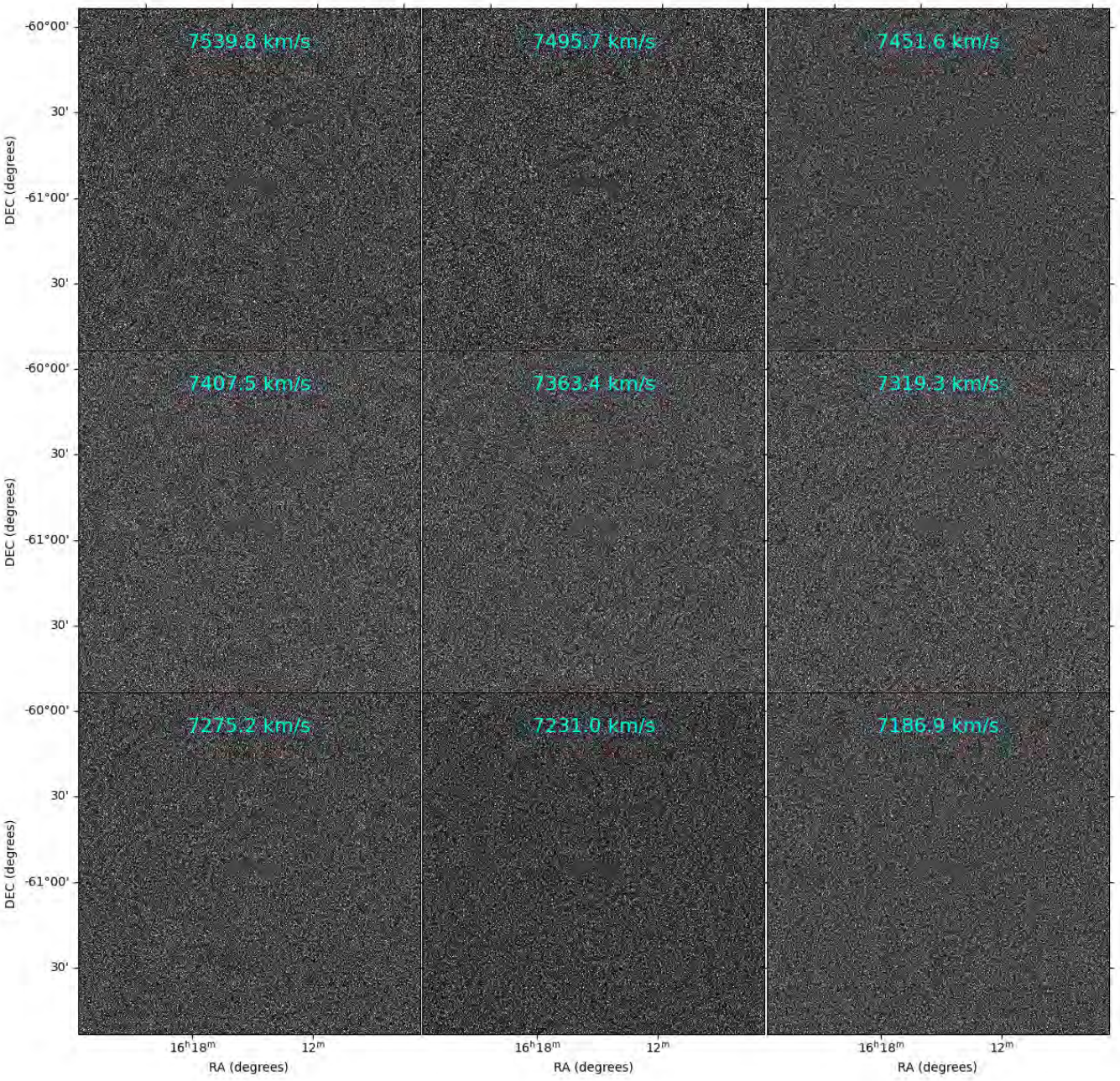
7539.8 km/s
7495.7 km/s
7451.6 km/s
7407.5 km/s
7363.4 km/s
7319.3 km/s
7275.2 km/s
7231.0 km/s
7186.9 km/s
-60°00'
30'
-61°00'
30'
DEC (degrees)
16h18m
12m
RA (degrees)

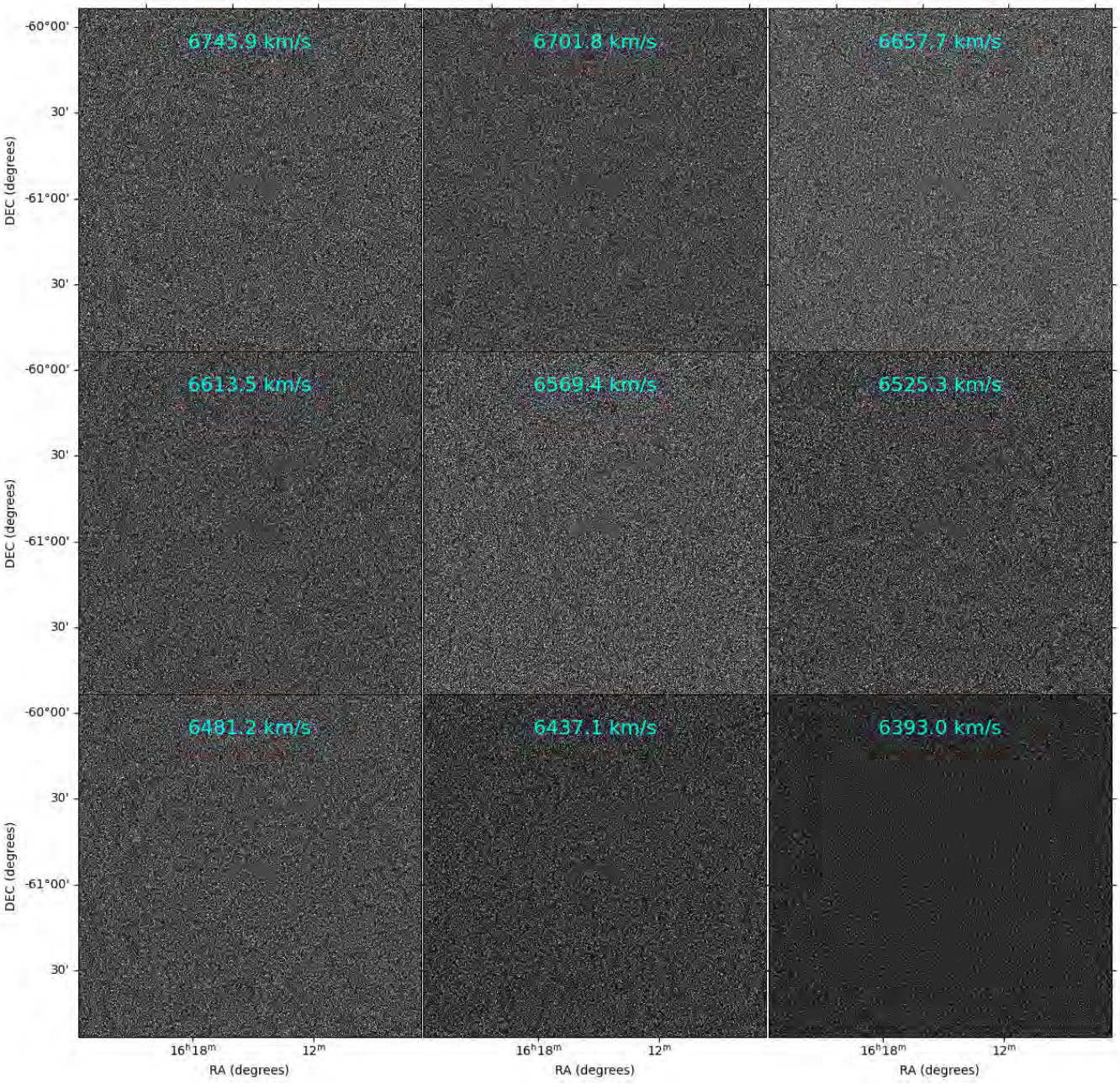
6745.9 km/s
6701.8 km/s
6657.7 km/s
6613.5 km/s
6569.4 km/s
6525.3 km/s
6481.2 km/s
6437.1 km/s
6393.0 km/s
DEC (degrees)
-60°00'
30'
-61°00'
30'
16h18m
12m
RA (degrees)

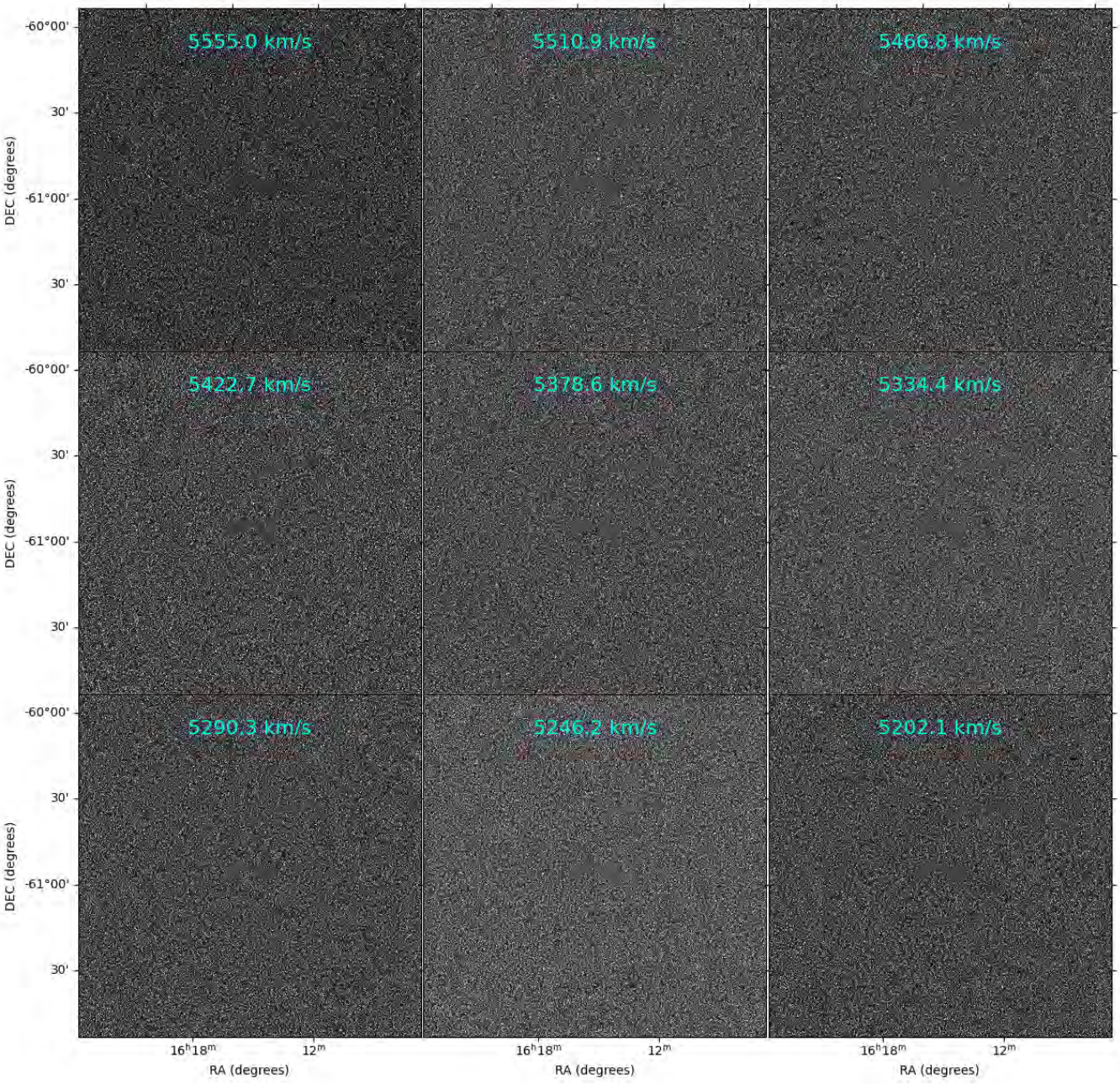
5555.0 km/s
5510.9 km/s
5466.8 km/s
5422.7 km/s
5378.6 km/s
5334.4 km/s
5290.3 km/s
5246.2 km/s
5202.1 km/s
-60°00'
30'
-61°00'
30'
DEC (degrees)
16h18m
12m
RA (degrees)

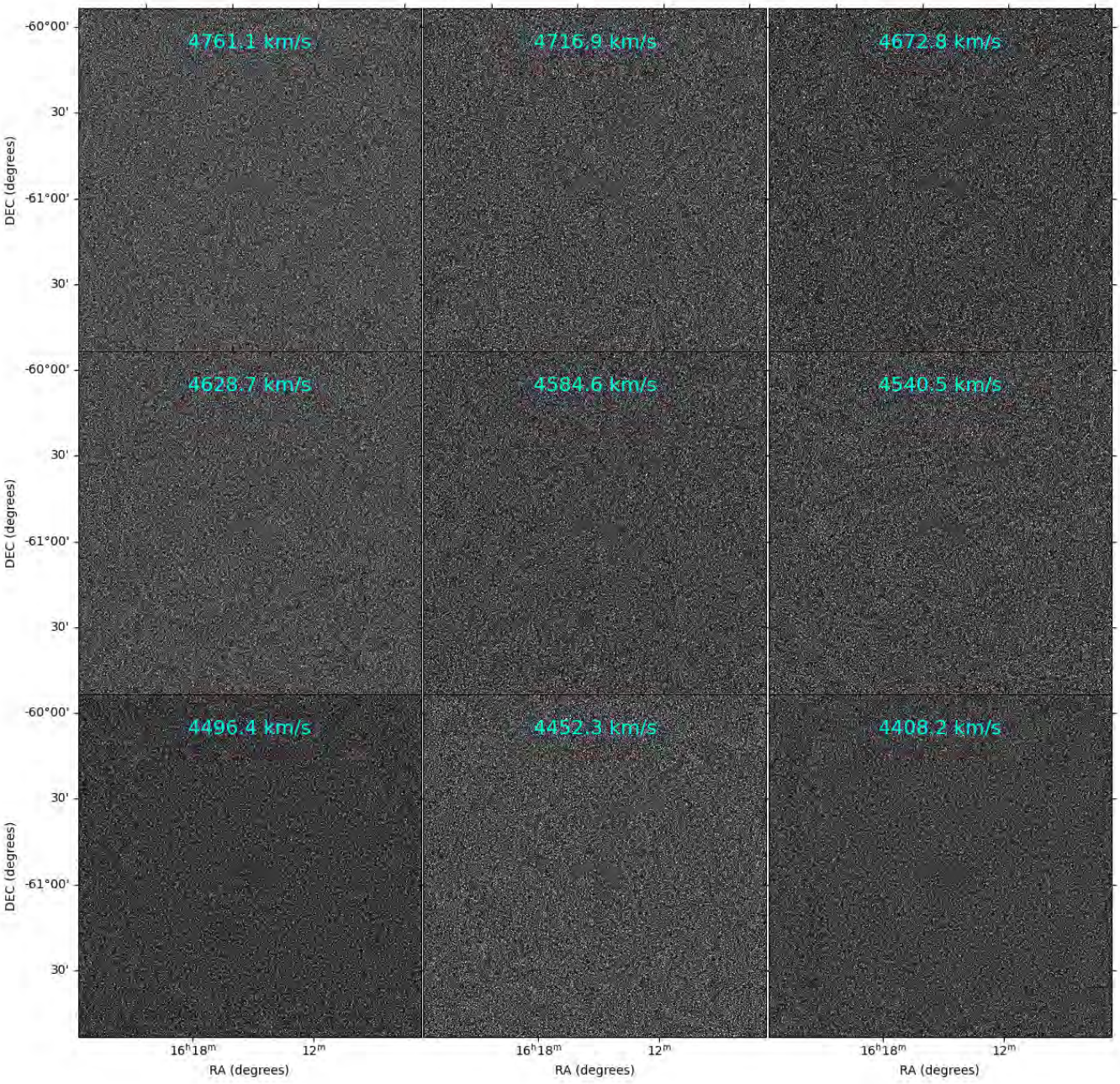
4761.1 km/s
4716.9 km/s
4672.8 km/s
4628.7 km/s
4584.6 km/s
4540.5 km/s
4496.4 km/s
4452.3 km/s
4408.2 km/s
-60°00'
30'
-61°00'
30'
DEC (degrees)
16h18m
12m
RA (degrees)

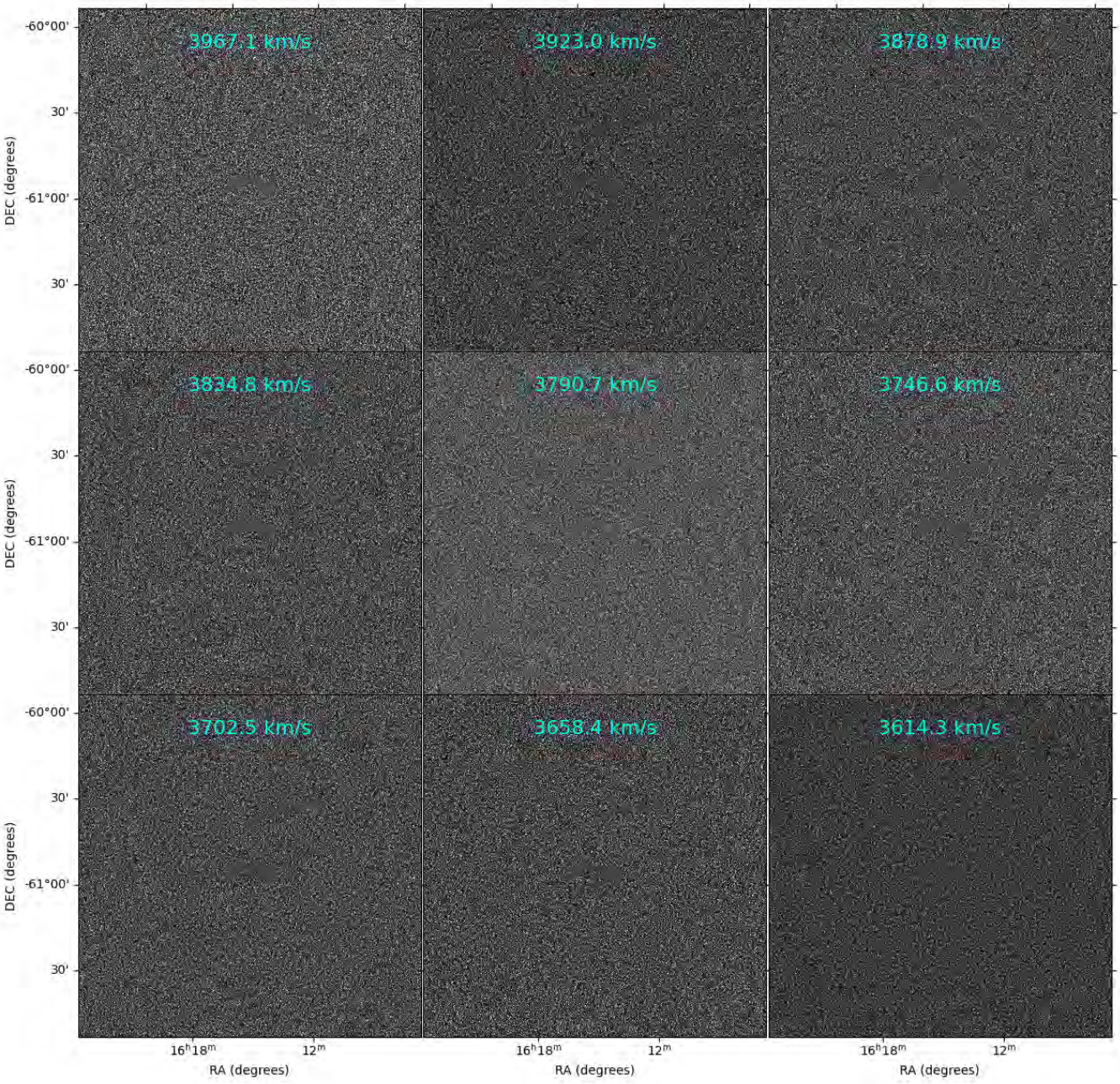
3967.1 km/s
3923.0 km/s
3878.9 km/s
3834.8 km/s
3790.7 km/s
3746.6 km/s
3702.5 km/s
3658.4 km/s
3614.3 km/s
-60°00'
30'
-61°00'
30'
DEC (degrees)
16h18m
12m
RA (degrees)

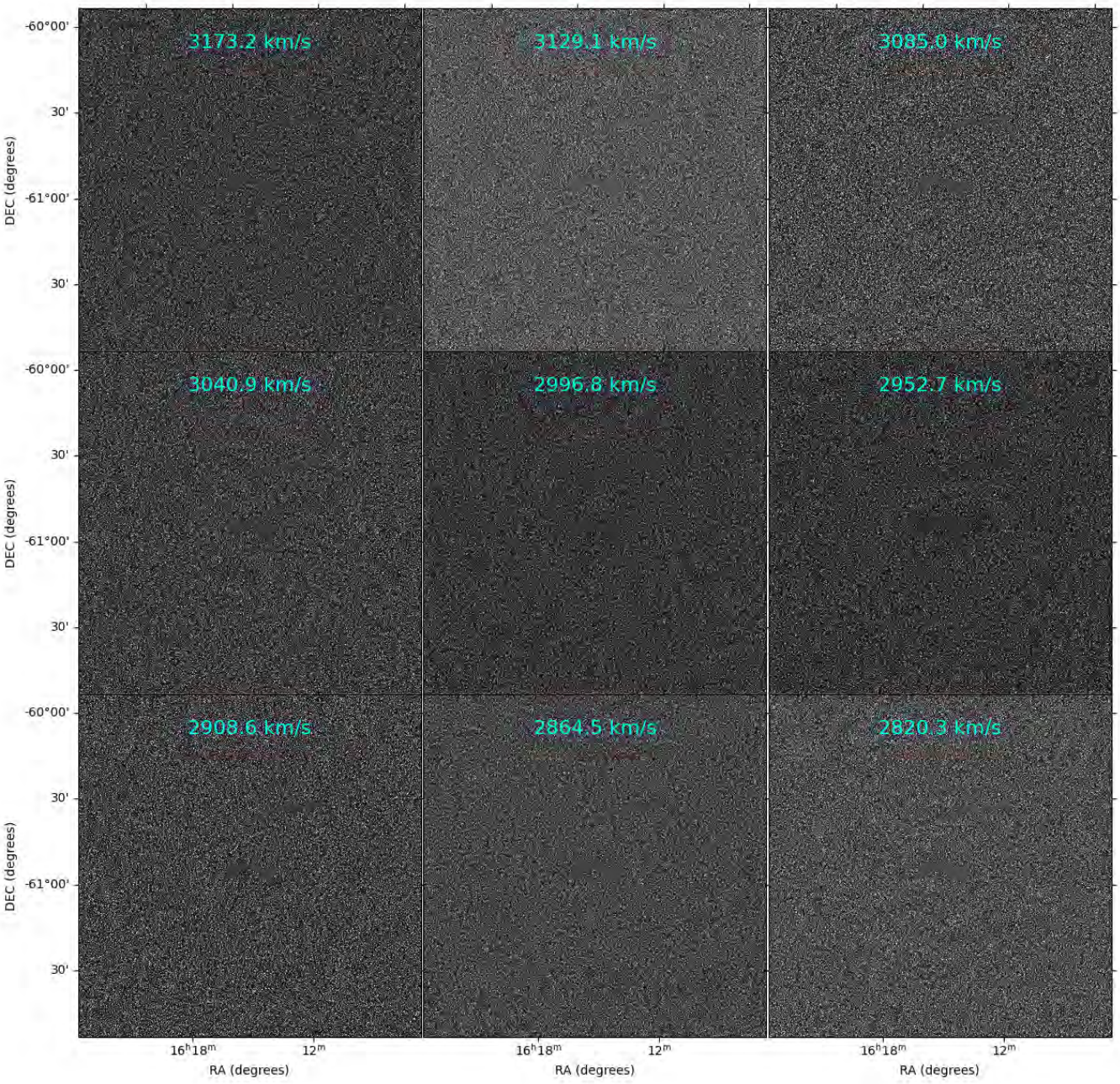
3173.2 km/s
3129.1 km/s
3085.0 km/s
3040.9 km/s
2996.8 km/s
2952.7 km/s
2908.6 km/s
2864.5 km/s
2820.3 km/s
-60°00'
30'
-61°00'
30'
DEC (degrees)
16h18m
12m
RA (degrees)

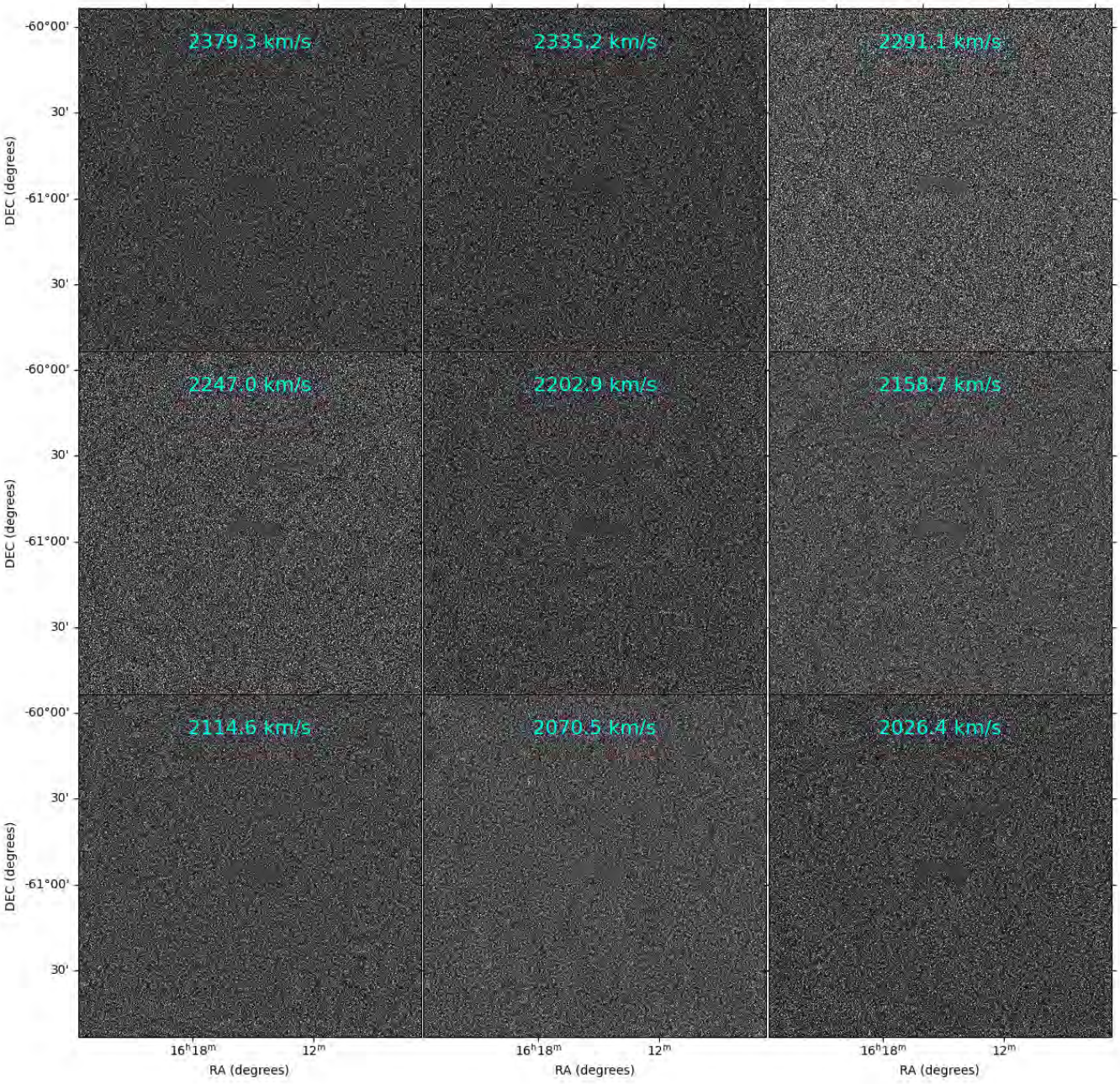
2379.3 km/s
2335.2 km/s
2291.1 km/s
2247.0 km/s
2202.9 km/s
2158.7 km/s
2114.6 km/s
2070.5 km/s
2026.4 km/s
-60°00'
30'
-61°00'
30'
DEC (degrees)
16h18m
12m
RA (degrees)

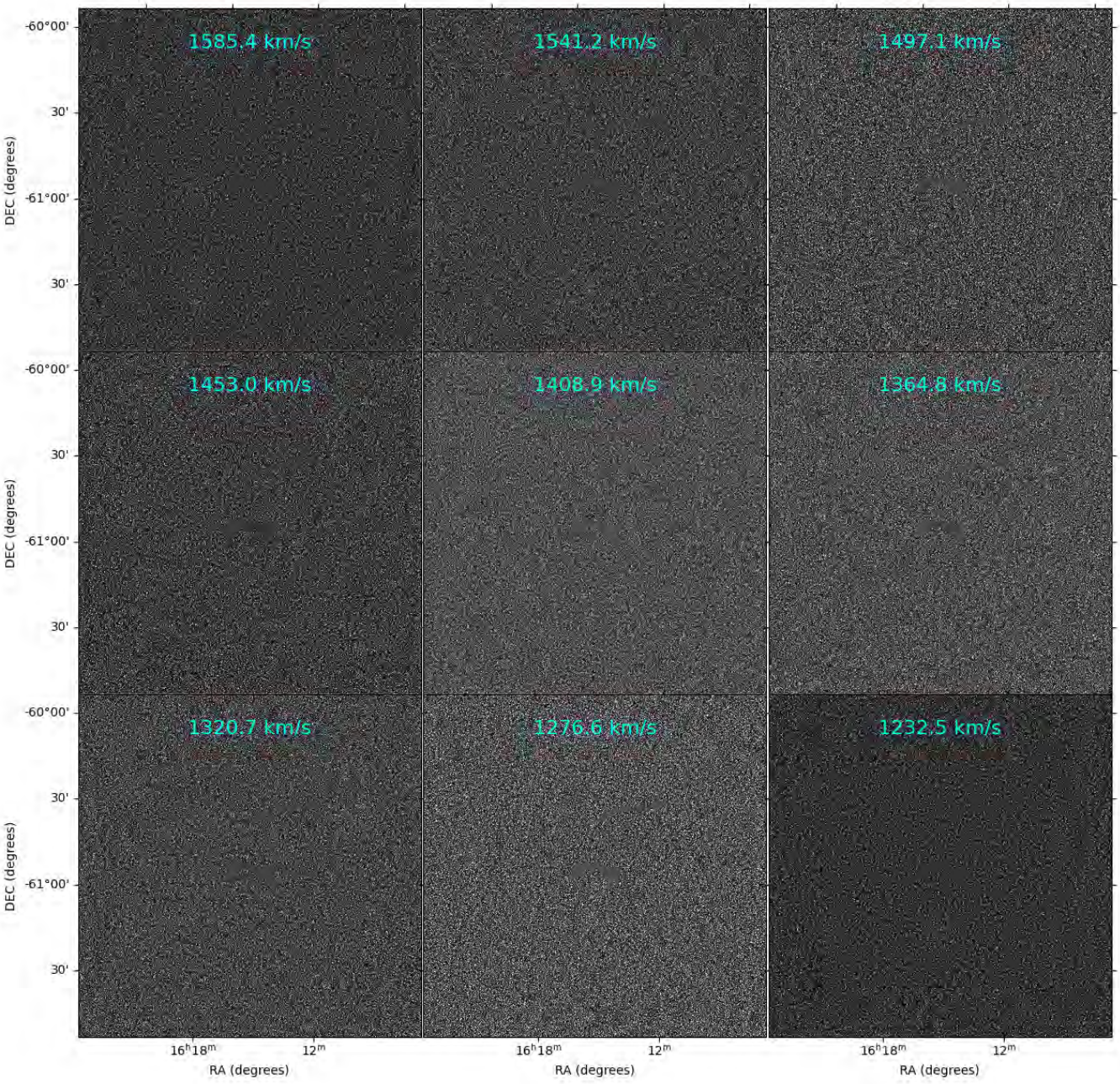
1585.4 km/s
1541.2 km/s
1497.1 km/s
1453.0 km/s
1408.9 km/s
1364.8 km/s
1320.7 km/s
1276.6 km/s
1232.5 km/s
-60°00'
30'
-61°00'
30'
DEC (degrees)
16h18m
12m
RA (degrees)

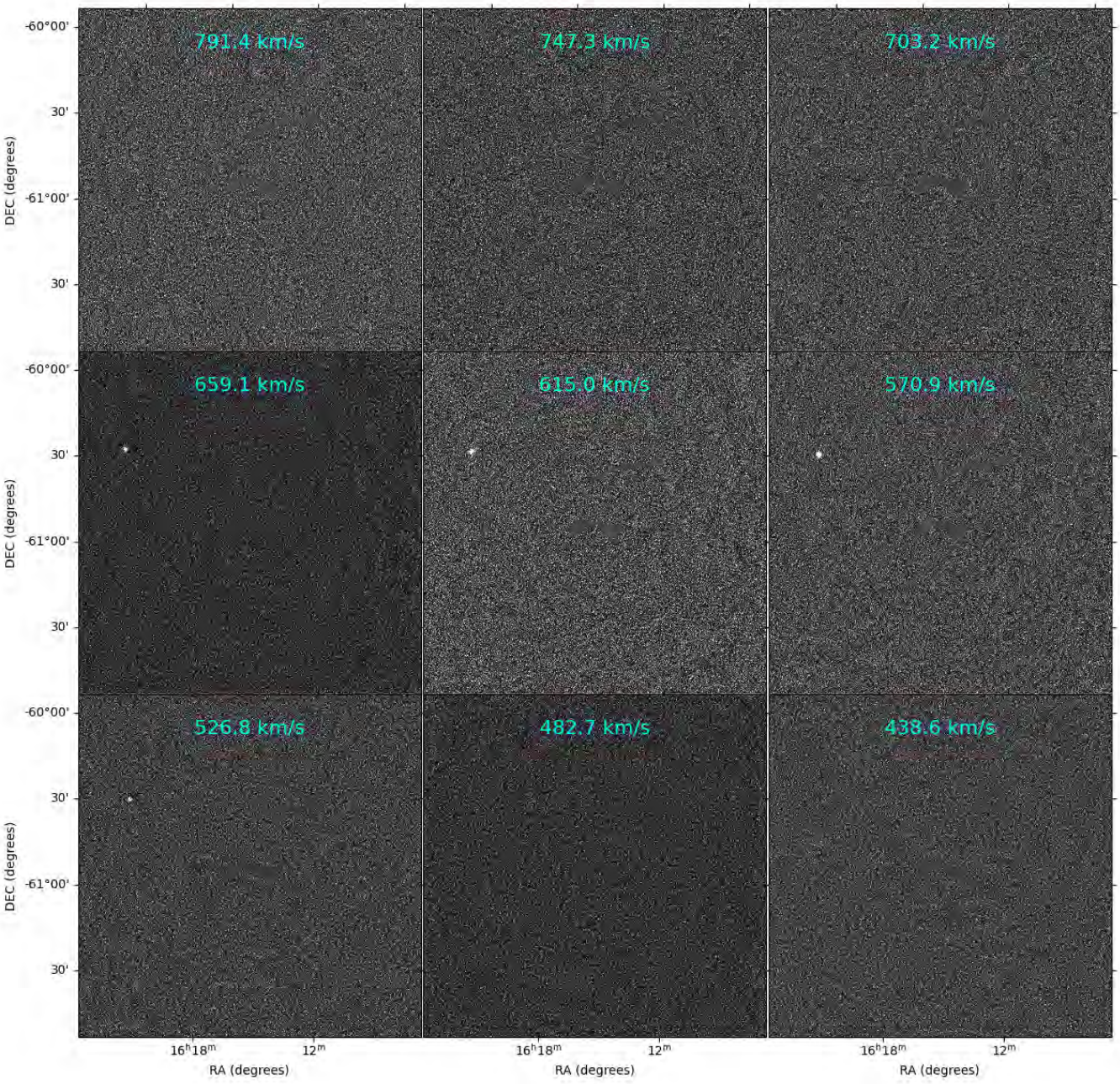
791.4 km/s
747.3 km/s
703.2 km/s
659.1 km/s
615.0 km/s
570.9 km/s
526.8 km/s
482.7 km/s
438.6 km/s
DEC (degrees)
-60°00'
30'
-61°00'
30'
16h18m
12m
RA (degrees)

A.2 SoFiA parameters

The SoFiA parameter file that was used to detect 31 galaxies in the Norma cluster field within a velocity range of $\sim 604 - 11,113$ km/s is added here.

```
CNHI.maxScale = -1
CNHI.medianTest = true
CNHI.minScale = 5
CNHI.pReq = 1e-5
CNHI.qReq = 3.8
CNHI.verbose = 1
SCfind.edgeMode = constant
SCfind.kernelUnit = pixel
SCfind.kernels = [[ 0, 0, 0,'b'],[ 0, 0, 3,'b'],[ 0, 0, 7,'b'],[ 0, 0, 15,'b'],
[ 3, 3, 0,'b'],[ 3, 3, 3,'b'],[ 3, 3, 7,'b'],[ 3, 3, 15,'b'],[ 6, 6, 0,'b'],
[ 6, 6,3,'b'],[ 6, 6, 7,'b'],[ 6, 6, 15,'b']]
SCfind.maskScaleXY = 2.0
SCfind.maskScaleZ = 2.0
SCfind.rmsMode = mad
SCfind.sizeFilter = 0.0
SCfind.threshold = 4.0
SCfind.verbose = true
flag.regions = []
import.inFile = /path/to/file/directory
import.maskFile =
import.subcube = []
import.subcubeMode = pixel
import.weightsFile =
import.weightsFunction =
merge.minSizeX = 3
merge.minSizeY = 3
merge.minSizeZ = 2
merge.positivity = false
merge.radiusX = 3
```

```
merge.radiusY = 3
merge.radiusZ = 3
optical.sourceCatalogue =
optical.spatSize = 0.01
optical.specSize = 1e+5
optical.storeMultiCat = false
parameters.dilateChan = 1
parameters.dilateMask = false
parameters.dilatePixMax = 10
parameters.dilateThreshold = 0.02
parameters.fitBusyFunction = false
parameters.getUncertainties = false
parameters.optimiseMask = false
reliability.autoKernel = true
reliability.fMin = 10.0
reliability.kernel = [0.15,0.05,0.1]
reliability.logPars = [1,1,1]
reliability.makePlot = true
reliability.negPerBin = 1.0
reliability.parSpace = ['n_pix','snr_sum','snr_max']
reliability.scaleKernel = 0.50
reliability.skellamTol = -0.5
reliability.threshold = 0.90
reliability.usecov = true
scaleNoise.edgeX = 0
scaleNoise.edgeY = 0
scaleNoise.edgeZ = 0
scaleNoise.scaleX = false
scaleNoise.scaleY = false
scaleNoise.scaleZ = true
scaleNoise.statistic = mad
smooth.edgeMode = constant
smooth.kernel = gaussian
```

```
smooth.kernelX = 3.0
smooth.kernelY = 3.0
smooth.kernelZ = 3.0
steps.doCNHI = false
steps.doCubelets = true
steps.doDebug = false
steps.doFlag = false
steps.doMerge = true
steps.doMom0 = true
steps.doMom1 = true
steps.doOptical = false
steps.doParameterise = false
steps.doReliability = true
steps.doSCfind = true
steps.doScaleNoise = false
steps.doSmooth = true
steps.doSubcube = false
steps.doThreshold = true
steps.doWavelet = false
steps.doWriteCat = true
steps.doWriteFilteredCube = true
steps.doWriteMask = true
threshold.clipMethod = relative
threshold.rmsMode = std
threshold.threshold = 4.0
threshold.verbose = false
wavelet.iterations = 3
wavelet.positivity = false
wavelet.scaleXY = -1
wavelet.scaleZ = -1
wavelet.threshold = 5.0
writeCat.basename = 10June2022
writeCat.compress = false
```

```
writeCat.outputDir = /path/to/output/directory
writeCat.overwrite = true
writeCat.parameters = ['*']
writeCat.writeASCII = true
writeCat.writeSQL = true
writeCat.writeXML = true
```

A.3 X-ray image of the intracluster medium

In Figure A.1, we present the overlays of moment-0 images of the identified galaxies on the X-ray image depicting the ICM within the Norma cluster. We only plot 7 (54%) of the cluster members within $1/3 \times R_A$.

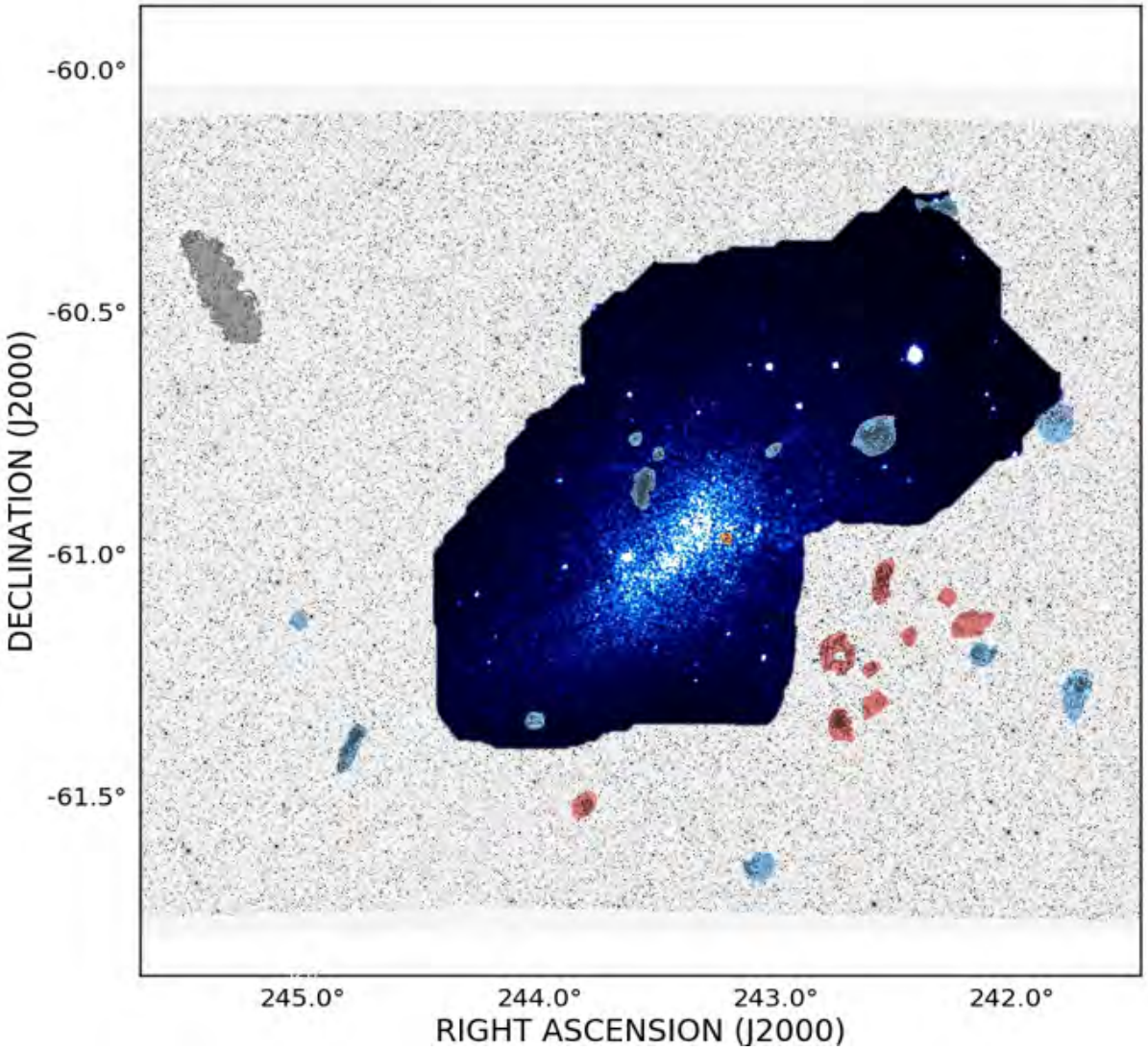

Figure A.1: X-ray spectroscopic image of the ICM colourmap in the core of the Norma cluster with up-scaled moment-0 overlays. The X-ray map is colour-coded using the Inferno colour map. The red contours in the core of the Norma cluster within $1/6 \times R_A$ in Figure 3.2, were observed in X-ray with the XMM-Newton facility. The inner regions are dense and hot, where no galaxy was detected in HI. Cluster members are coloured in blue while the background group ($v_{rad} \sim 10,000$ km/s) and the foreground source ($v_{rad} \sim 604$ km/s) are coloured in red.

References

Abadi M. G., Moore B., Bower R. G., 1999, , 308, 947

Abell G. O., 1958, The Astrophysical Journal Supplement Series, 3, 211

Abraham R. G., Valdes F., Yee H., van den Bergh S., 1994, The Astrophysical Journal, 432, 75

Allen S., Fabian A., 1998, Monthly Notices of the Royal Astronomical Society, 297, L63

Argudo-Fernández M., et al., 2015, Astronomy & Astrophysics, 578, A110

Bahcall N. A., 1996, Formation of Structure in the Universe, 135

Bahé Y. M., McCarthy I. G., Balogh M. L., Font A. S., 2013, Monthly Notices of the Royal Astronomical Society, 430, 3017

Balick B., Heckman T., 1981, Astronomy and Astrophysics, 96, 271

Banfield J., Koribalski B., Johnston-Hollitt M., Wong O. I., Serra P., Schnitzeler D., Dehghan S., 2013, Mapping the intracluster medium of Abell 3627, ATNF proposal id.C2891, Semester: October, 2013

Banfield J. K., et al., 2015, Monthly Notices of the Royal Astronomical Society, 453, 2326

Barnes J. E., Hernquist L., 1996, The Astrophysical Journal, 471, 115

Battye R. A., Davies R. D., Weller J., 2004, , 355, 1339

Bekki K., 2014, , 438, 444

Bekki K., Couch W. J., Shioya Y., 2002, The Astrophysical Journal, 577, 651

Belokurov V., Evans N. W., 2022, Nature Astronomy, 6, 911

Bertola F., Pizzella A., Persic M., Salucci P., 1993, The Astrophysical Journal, 416, L45

Biffi V., et al., 2017, Monthly Notices of the Royal Astronomical Society, 468, 531

Bigiel F., Leroy A., Walter F., Brinks E., De Blok W., Madore B., Thornley M. D., 2008, The Astronomical Journal, 136, 2846

Binney J., Tremaine S., 2011, Galactic dynamics. Vol. 13, Princeton university press

Blitz L., Rosolowsky E., 2006, The Astrophysical Journal, 650, 933

Böhringer H., Werner N., 2010, The Astronomy and Astrophysics Review, 18, 127

Bohringer H., Neumann D. M., Schindler S., Kraan-Korteweg R. C., 1996, , 467, 168

Booth R. S., Jonas J. L., 2012, African Skies, 16, 101

Booth R., Blok W., Jonas J., Fanaroff B., 2009

Boselli A., Boissier S., Cortese L., Buat V., Hughes T., Gavazzi G., 2009, The Astrophysical Journal, 706, 1527

Boselli A., et al., 2016, Astronomy & Astrophysics, 596, A11

Bothun G. D., Dressler A., 1986, , 301, 57

Bournaud F., Elmegreen B. G., Martig M., 2009, The Astrophysical Journal, 707, L1

Bovy J., Rix H.-W., 2013, The Astrophysical Journal, 779, 115

Braglia F., Pierini D., Biviano A., Böhringer H., 2009, Astronomy & Astrophysics, 500, 947

Bridge C. R., et al., 2007, , 659, 931

Brown S., 2011, Measures of shape: Skewness and kurtosis

Burstein D., Faber S., Dressler A., 1990, The Astrophysical Journal, 354, 18

Byrd G. G., 1988, in Valtonen M. J., ed., IAU Colloq. 96: The Few Body Problem. p. 371, doi:10.1007/978-94-009-2917-3_56

Carlberg R., Yee H., Ellingson E., Abraham R., Gravel P., Morris S., Pritchet C., 1996, The Astrophysical Journal, 462, 32

Catinella B., et al., 2018, Monthly Notices of the Royal Astronomical Society, 476, 875

Cattaneo A., 2015, , 521, 164

Cavaliere A., Fusco-Femiano R., 1976, Astronomy and Astrophysics, 49, 137

Cayatte V., Kotanyi C., Balkowski C., Van Gorkom J., 1994, The Astronomical Journal, 107, 1003

Cellone S. A., Forte J. C., 1997, The Astronomical Journal, 113, 1239

Cerulo P., et al., 2016, Monthly Notices of the Royal Astronomical Society, 457, 2209

Chanamé J., Infante L., Reisenegger A., 2000, The Astrophysical Journal, 530, 96

Chen H., et al., 2020, Monthly Notices of the Royal Astronomical Society, 496, 4654

Chung A., van Gorkom J. H., Kenney J. D. P., Crowl H., Vollmer B., 2009, , 138, 1741

Chung E. J., Yun M. S., Verheijen M. A., Chung A., 2017, The Astrophysical Journal, 843, 50

Churazov E., Khabibullin I., Lyskova N., Sunyaev R., Bykov A., 2021, Astronomy & Astrophysics, 651, A41

Cicone C., et al., 2014, , 562, A21

Cicone C., et al., 2018, The Astrophysical Journal, 863, 143

Clemens M., Bressan A., Nikolic B., Alexander P., Annibali F., Rampazzo R., 2006, Monthly Notices of the Royal Astronomical Society, 370, 702

Cluver M. E., et al., 2014, The Astrophysical Journal, 782, 90

Collett T. E., et al., 2018, Science, 360, 1342

Combes F., 2018, in Multiphase AGN Feeding & Feedback; Linking the Micro to Macro Scales in Galaxies, Groups, and Clusters. p. 10

Conselice C. J., 1997, Publications of the Astronomical Society of the Pacific, 109, 1251

Conselice C. J., 2003a, The Astrophysical Journal Supplement Series, 147, 1

Conselice C. J., 2003b, , 147, 1

Conselice C. J., Bershady M. A., Jangren A., 2000, The Astrophysical Journal, 529, 886

Conselice C. J., Yang C., Bluck A. F., 2009, Monthly Notices of the Royal Astronomical Society, 394, 1956

Corwin H. G., de Vaucouleurs A., de Vaucouleurs G., 1994, VizieR Online Data Catalog, p. VII/116

Courteau S., et al., 2014, Reviews of Modern Physics, 86, 47

Davies J. I., Roberts S., Sabatini S., 2005, Monthly Notices of the Royal Astronomical Society, 356, 794

De Lucia G., Kauffmann G., White S. D., 2004, Monthly Notices of the Royal Astronomical Society, 349, 1101

De Lucia G., Weinmann S., Poggianti B. M., Aragon-Salamanca A., Zaritsky D., 2012, Monthly Notices of the Royal Astronomical Society, 423, 1277

De Vaucouleurs G., de Vaucouleurs A., Corwin J., 1976, Second reference catalogue of bright galaxies, 1976, 0

Deeley S., et al., 2017, Monthly Notices of the Royal Astronomical Society, 467, 3934

Dekel A., et al., 2009, Nature, 457, 451

Di Matteo P., Combes F., Melchior A.-L., Semelin B., 2007, Astronomy & Astrophysics, 468, 61

Donahue M., 1998, in Origins. p. 109

Dressler A., 1980, The Astrophysical Journal, 236, 351

Dressler A., Oemler A., Poggianti B. M., Gladders M. D., Abramson L., Vulcani B., 2013, The Astrophysical Journal, 770, 62

Ebeling H., Stephenson L. N., Edge A. C., 2014, The Astrophysical Journal Letters, 781, L40

Eisenhardt P. R., et al., 2012, The Astrophysical Journal, 755, 173

Ellingson E., Lin H., Yee H. K. C., Carlberg R. G., 2001, , 547, 609

England M. N., 1989a, , 337, 191

England M. N., 1989b, , 344, 669

Fabian A. C., 2012, , 50, 455

Fabian A., et al., 2011, Monthly Notices of the Royal Astronomical Society, 418, 2154

Fiacconi D., Feldmann R., Mayer L., 2015, Monthly Notices of the Royal Astronomical Society, 446, 1957

Fluetsch A., et al., 2019, , 483, 4586

Fumagalli M., Gavazzi G., 2008, Astronomy & Astrophysics, 490, 571

Gabor J., Davé R., Finlator K., Oppenheimer B., 2010, Monthly Notices of the Royal Astronomical Society, 407, 749

Gabor J. M., Davé R., Oppenheimer B. D., Finlator K., 2011, Monthly Notices of the Royal Astronomical Society, 417, 2676

Gaspari M., Brighenti F., Temi P., 2012, Monthly Notices of the Royal Astronomical Society, 424, 190

Gavazzi G., Consolandi G., Gutierrez M., Boselli A., Yoshida M., 2018, Astronomy & Astrophysics, 618, A130

George D., Mallery P., 2010, GEN, Boston, MA: Pearson Education, Inc, 10

Geyer M., et al., 2021, Monthly Notices of the Royal Astronomical Society, 505, 4468

Ghigna S., Moore B., Governato F., Lake G., Quinn T., Stadel J., 1998, Monthly Notices of the Royal Astronomical Society, 300, 146

Glover S. C., Clark P. C., 2012, Monthly Notices of the Royal Astronomical Society, 421, 9

Gordon K. D., et al., 2006, , 638, L87

Goulding A. D., et al., 2017, Publications of the Astronomical Society of Japan, 70

Grossi M., et al., 2015, Astronomy & Astrophysics, 574, A126

Gunn J. E., Gott J. Richard I., 1972, , 176, 1

Gunn J. E., Gott III J. R., 1972, The Astrophysical Journal, 176, 1

Guo H., Jones M. G., Wang J., Lin L., 2021, The Astrophysical Journal, 918, 53

Gurzadyan V., Stepanian A., 2018, The European Physical Journal C, 78, 1

Haines C., Gargiulo A., La Barbera F., Mercurio A., Merluzzi P., Busarello G., 2007, Monthly Notices of the Royal Astronomical Society, 381, 7

Hausman M., Ostriker J., 1978, The Astrophysical Journal, 224, 320

Haynes M. P., Giovanelli R., Chincarini G. L., 1984, , 22, 445

Hernández-Fernández J. D., Haines C. P., Diaferio A., Iglesias-Páramo J., Mendes de Oliveira C., Vilchez J. M., 2014, Monthly Notices of the Royal Astronomical Society, 438, 2186

Hester J. A., 2006, , 647, 910

Hilker M., Bomans D. J., Infante L., Kissler-Patig M., 1997, , 327, 562

Holwerda B. W., Pirzkal N., de Blok W. J. G., van Driel W., 2011, Monthly Notices of the Royal Astronomical Society, 416, 2447

Hopkins A., McClure-Griffiths N., Gaensler B., 2008, The Astrophysical Journal, 682, L13

Hopkins P. F., Cox T. J., Younger J. D., Hernquist L., 2009, The Astrophysical Journal, 691, 1168

Hubble E. P., 1926, The Astrophysical Journal, 64

Hubble E., 1937, Ciel et Terre, 53, 194

Hughes T. M., Cortese L., Boselli A., Gavazzi G., Davies J., 2013, Astronomy & Astrophysics, 550, A115

Hunter D., Gallagher III J., 1985, The Astrophysical Journal Supplement Series, 58, 533

Ibarra-Medel H. J., et al., 2016, Monthly Notices of the Royal Astronomical Society, 463, 2799

Iono D., Yun M. S., Mihos J. C., 2004, The Astrophysical Journal, 616, 199

Ivison R., Smail I., Le Borgne J.-F., Blain A., Kneib J.-P., Bezecourt J., Kerr T., Davies J., 1998, Monthly Notices of the Royal Astronomical Society, 298, 583

Jáchym P., et al., 2019, The Astrophysical Journal, 883, 145

Jaffé Y. L., et al., 2018, , 476, 4753

Jaffé Y. L., Smith R., Candlish G. N., Poggianti B. M., Sheen Y.-K., Verheijen M. A. W., 2015, Monthly Notices of the Royal Astronomical Society, 448, 1715

Jansen F., et al., 2001, Astronomy & Astrophysics, 365, L1

Jarrett T., et al., 2011, The Astrophysical Journal, 735, 112

Jarrett T., et al., 2012, The Astronomical Journal, 145, 6

Jarrett T. H., et al., 2013, , 145, 6

Jarrett T. H., et al., 2017, , 836, 182

Jarrett T. H., Cluver M. E., Brown M. J. I., Dale D. A., Tsai C. W., Masci F., 2019, , 245, 25

Jarvis M. J., 2012, African Skies, 16, 44

Jonas J., 2009, in Panoramic Radio Astronomy: Wide-field 1-2 GHz Research on Galaxy Evolution. p. 4

Jonas J., MeerKAT Team 2016, in MeerKAT Science: On the Pathway to the SKA. p. 1

Jones P. A., McAdam W. B., 1992, The Astrophysical Journal Supplement Series, 80, 137

Józsa G. I. G., et al., 2020, CARACal: Containerized Automated Radio Astronomy Calibration pipeline, Astrophysics Source Code Library, record ascl:2006.014 (ascl:2006.014)

KOLE C. B. M., 2018, CERN Courier

Kapferer W., Kronberger T., Ferrari C., Riser T., Schindler S., 2008, , 389, 1405

Kapferer W., Schindler S., Ziegler B., Ferrari C., 2010, in 38th COSPAR Scientific Assembly. p. 5

Kaviraj S., et al., 2014, Monthly Notices of the Royal Astronomical Society, 443, 1861

Kenney J. D., Abramson A., Bravo-Alfaro H., 2015, The Astronomical Journal, 150, 59

Kim D.-W., Guhathakurta P., Van Gorkom J., Jura M., Knapp G., 1988, Astrophysical Journal, Part 1 (ISSN 0004-637X), vol. 330, July 15, 1988, p. 684-694., 330, 684

King A., Pounds K., 2015, , 53, 115

Knebe A., Power C., Gill S. P., Gibson B. K., 2006, Monthly Notices of the Royal Astronomical Society, 368, 741

Knowles K., et al., 2022, Astronomy & Astrophysics, 657, A56

Kochanek C., et al., 2001, The Astrophysical Journal, 560, 566

Koopmann R. A., Kenney J. D., 2004, The Astrophysical Journal, 613, 851

Kormendy J., Fisher D. B., Cornell M. E., Bender R., 2009, The Astrophysical Journal Supplement Series, 182, 216

Kotov O., Vikhlinin A., 2006, The Astrophysical Journal, 641, 752

Kraan-Korteweg R. C., Lahav O., 2000, , 10, 211

Kravtsov A. V., Borgani S., 2012, Annual Review of Astronomy and Astrophysics, 50, 353

Krumholz M. R., McKee C. F., Tumlinson J., 2009a, The Astrophysical Journal, 693, 216

Krumholz M. R., McKee C. F., Tumlinson J., 2009b, The Astrophysical Journal, 699, 850

Kuntschner H., 2000, Monthly Notices of the Royal Astronomical Society, 315, 184

Lake G., Schommer R., Van Gorkom J., 1987, The Astrophysical Journal, 314, 57

Lambas D. G., Alonso S., Mesa V., O'Mill A. L., 2012, , 539, A45

Laudari S., et al., 2022, , 509, 3938

Leccardi A., Molendi S., 2008, Astronomy & Astrophysics, 486, 359

Lee N., Cosmos Team 2015, in American Astronomical Society Meeting Abstracts #225. p. 329.03

Lee-Waddell K., et al., 2018, Monthly Notices of the Royal Astronomical Society, 474, 1108

Lee J., Lee M., Mun J., Cho B., Kang J., 2022a, Enhanced Star Formation Activity of Extreme Jellyfish Galaxies in Massive Clusters and the Role of Ram Pressure Stripping

Lee J. H., Lee M. G., Mun J. Y., Cho B. S., Kang J., 2022b, , 931, L22

Lees J. F., Knapp G., Rupen M. P., Phillips T., 1991, The Astrophysical Journal, 379, 177

Lelli F., Verheijen M., Fraternali F., 2014, Monthly Notices of the Royal Astronomical Society, 445, 1694

Leroy A. K., Walter F., Brinks E., Bigiel F., De Blok W., Madore B., Thornley M., 2008, The astronomical journal, 136, 2782

Lewis M. E., 2002, Child and adolescent psychiatry: A comprehensive textbook. Lippincott Williams & Wilkins Publishers

Lewis I., et al., 2002, , 334, 673

Lindblad P., Kristen H., 1996, Astronomy and Astrophysics, 313, 733

Lindblad P., Kristen H., Joersaeter S., Hoegbom J., 1997, Astronomy and Astrophysics, 317, 36

Lu N., Dow M., Houck J., Salpeter E., Lewis B., 1990, The Astrophysical Journal, 357, 388

Mahajan S., Mamon G. A., Raychaudhury S., 2011, Monthly Notices of the Royal Astronomical Society, 416, 2882

Mainzer A. K., Eisenhardt P., Wright E. L., Liu F.-C., Irace W., Heinrichsen I., Cutri R., Duval V., 2005, in UV/Optical/IR Space Telescopes: Innovative Technologies and Concepts II. pp 262–273

Mainzer A., et al., 2011, The Astrophysical Journal, 731, 53

Mamon G. A., Biviano A., Murante G., 2010, Astronomy & Astrophysics, 520, A30

Martin G., et al., 2021, Monthly Notices of the Royal Astronomical Society, 500, 4937

Martis N. S., 2020, PhD thesis, Tufts University, Massachusetts

Masiero J. R., Grav T., Mainzer A., Nugent C., Bauer J., Stevenson R., Sonnett S., 2014, The Astrophysical Journal, 791, 121

Mathewson D., Ford V., Buchhorn M., 1992, Astrophysical Journal, Part 2-Letters (ISSN 0004-637X), vol. 389, April 10, 1992, p. L5-L8., 389, L5

Mauch T., et al., 2020, The Astrophysical Journal, 888, 61

Mayer L., Governato F., Colpi M., Moore B., Quinn T., Wadsley J., Stadel J., Lake G., 2001, The Astrophysical Journal, 559, 754

Mazzei R., Vijayaraghavan R., Sarazin C. L., 2018, in American Astronomical Society Meeting Abstracts #231. p. 252.12

McGaugh S. S., 2012, The Astronomical Journal, 143, 40

McGaugh S. S., De Blok W., 1997, The Astrophysical Journal, 481, 689

McGee S. L., Balogh M. L., Bower R. G., Font A. S., McCarthy I. G., 2009, Monthly Notices of the Royal Astronomical Society, 400, 937

Meidt S. E., et al., 2012, , 748, L30

Mihos J. C., Keating K. M., Holley-Bockelmann K., Pisano D. J., Kassim N. E., 2012, , 761, 186

Miller R. H., 1986, , 167, 41

Mohr J. J., Evrard A. E., Fabricant D. G., Geller M. J., 1995

Molnár D. C., et al., 2022, Astronomy & Astrophysics, 659, A94

Moore B., Katz N., Lake G., Dressler A., Oemler A., 1996, , 379, 613

Moore B., Lake G., Katz N., 1998, The Astrophysical Journal, 495, 139

Moore B., Lake G., Quinn T., Stadel J., 1999, , 304, 465

Mora M. D., Chanamé J., Puzia T. H., 2015, The Astronomical Journal, 150, 93

Mutabazi T., 2021b, The Astrophysical Journal, 911, 16

Mutabazi T., 2021a, , 911, 16

Mutabazi T., Blyth S., Woudt P., Lucey J., Jarrett T., Bilicki M., Schröder A., Moore S., 2014, Monthly Notices of the Royal Astronomical Society, 439, 3666

Naab T., Khochfar S., Burkert A., 2006, The Astrophysical Journal, 636, L81

Negroponte J., White S. D., 1983, Monthly Notices of the Royal Astronomical Society, 205, 1009

Nelson D., et al., 2019, Monthly Notices of the Royal Astronomical Society, 490, 3234

Nishino S., Fukazawa Y., Hayashi K., 2012, , 64, 16

Ogle P. M., Jarrett T., Lanz L., Cluver M., Alatalo K., Appleton P. N., Mazzarella J. M., 2019, The Astrophysical Journal Letters, 884, L11

Oman K. A., Hudson M. J., Behroozi P. S., 2013, Monthly Notices of the Royal Astronomical Society, 431, 2307

Oosterloo T., Fraternali F., Sancisi R., 2007, , 134, 1019

Pahre M. A., Ashby M. L. N., Fazio G. G., Willner S. P., 2004, , 154, 229

Panko E., 2015, Introduction to Cosmology, pp 85–88

Park C., Hwang H. S., 2009, The Astrophysical Journal, 699, 1595

Pedraz S., Gorgas J., Cardiel N., Sánchez-Blázquez P., Guzmán R., 2002, Monthly Notices of the Royal Astronomical Society, 332, L59

Peng Y.-j., et al., 2010, , 721, 193

Peng Y., Maiolino R., Cochrane R., 2015, Nature, 521, 192

Piotrowska J. M., Bluck A. F. L., Maiolino R., Peng Y., 2021, Monthly Notices of the Royal Astronomical Society, 512, 1052

Popesso P., Biviano A., Böhringer H., Romaniello M., 2006, Astronomy & Astrophysics, 445, 29

Press W., Davis M., 1982, The Astrophysical Journal, 259, 449

Pritchard J. R., Loeb A., 2012, Reports on Progress in Physics, 75, 086901

Quintero A. D., Berlind A. A., Blanton M. R., Hogg D. W., 2005, arXiv preprint astro-ph/0512004

Rafieferantsoa M., Davé R., 2018, , 475, 955

Raimond E., Faber S., Gallagher III J., Knapp G., 1981, The Astrophysical Journal, 246, 708

Ramatsoku M. A., 2017, PhD thesis, University of Cape Town

Ramatsoku M., et al., 2020, Astronomy & Astrophysics, 636, L1

Ranchod S., Deane R., Obreschkow D., Blecher T., Heywood I., 2021, Monthly Notices of the Royal Astronomical Society, 509, 5155

Randriamampandry T. H., Wang J., Mogotsi K. M., 2021, The Astrophysical Journal, 916, 26

Raychaudhury S., 1989, Nature, 342, 251

Ressler M. E., Cohen M., Wachter S., Hoard D., Mainzer A. K., Wright E. L., 2010, The Astronomical Journal, 140, 1882

Rhee J., Smith R., Choi H., Sukyoung K. Y., Jaffé Y., Candlish G., Sánchez-Jánssen R., 2017, The Astrophysical Journal, 843, 128

Roberts I. D., Parker L. C., 2017, Monthly Notices of the Royal Astronomical Society, 467, 3268

Roberts I., Parker L., 2020a, Monthly Notices of the Royal Astronomical Society, 495, 554

Roberts I. D., Parker L. C., 2020b, Monthly Notices of the Royal Astronomical Society, 495, 554

Roediger E., Hensler G., 2005, , 433, 875

Roediger E., et al., 2015, , 806, 103

Rosenberg J. L., Schneider S. E., 2002, , 567, 247

Saintonge A., et al., 2016, Monthly Notices of the Royal Astronomical Society, 462, 1749

Salim S., Fang J. J., Rich R. M., Faber S., Thilker D. A., 2012, The Astrophysical Journal, 755, 105

Sancisi R., Fraternali F., Oosterloo T., van der Hulst T., 2008, The Astronomy and Astrophysics Review, 15, 189–223

Sandage A., 1961, The Hubble atlas of galaxies. Vol. 618, Carnegie Institution of Washington Washington, DC

Sarazin C. L., 1988

Schiminovich D., Van Gorkom J., Van der Hulst J., Malin D., 1995, The Astrophysical Journal, 444, L77

Schiminovich D., van Gorkom J., van der Hulst T., Oosterloo T., Wilkinson A., 1997, in The Nature of Elliptical Galaxies; 2nd Stromlo Symposium. p. 362

Schlegel D. J., Finkbeiner D. P., Davis M., 1998, The Astrophysical Journal, 500, 525

Schweizer F., van Gorkom J. H., Seitzer P., 1989, Astrophysical Journal, Part 1 (ISSN 0004-637X), vol. 338, March 15, 1989, p. 770-788., 338, 770

Semczuk M., Łokas E. L., del Pino A., 2017, , 834, 7

Serra P., et al., 2015, , 448, 1922

Serra P., et al., 2023, arXiv preprint arXiv:2302.11895

Shin J., Woo J.-H., Chung A., Baek J., Cho K., Kang D., Bae H.-J., 2019, The Astrophysical Journal, 881, 147

Simpson C. M., Grand R. J. J., Gómez F. A., Marinacci F., Pakmor R., Springel V., Campbell D. J. R., Frenk C. S., 2018, Monthly Notices of the Royal Astronomical Society, 478, 548

Sinha M., Holley-Bockelmann K., 2012, The Astrophysical Journal, 751, 17

Sivanandam S., Rieke M. J., Rieke G. H., 2010, The Astrophysical Journal, 717, 147

Skelton R. E., Woudt P. A., Kraan-Korteweg R. C., 2010, VizieR Online Data Catalog, p. J/MNRAS/396/2367

Smith R. J., Blakeslee J. P., Lucey J. R., Tonry J., 2005, The Astrophysical Journal, 625, L103

Smith R., Davies J. I., Nelson A. H., 2010, Monthly Notices of the Royal Astronomical Society, 405, 1723

Solanes J. M., Manrique A., García-Gómez C., González-Casado G., Giovanelli R., Haynes M. P., 2001, The Astrophysical Journal, 548, 97

Sparke L. S., Gallagher III J. S., 2007, Galaxies in the universe: an introduction. Cambridge University Press

Staniszewski Z., et al., 2009, The Astrophysical Journal, 701, 32

Steinhauser D., Schindler S., Springel V., 2016, , 591, A51

Stern D., et al., 2012a, in American Astronomical Society Meeting Abstracts #219. p. 243.13

Stern D., et al., 2012b, , 753, 30

Stewart I. M., Blyth S., de Blok W., 2014, arXiv: Instrumentation and Methods for Astrophysics

Steyrleithner P., Hensler G., Boselli A., 2020, Monthly Notices of the Royal Astronomical Society, 494, 1114

Sun M., Donahue M., Roediger E., Nulsen P. E. J., Voit G. M., Sarazin C., Forman W., Jones C., 2010, , 708, 946

Tayler R. J., 1993, Galaxies: structure and evolution. Cambridge University Press

Tempel E., Tenjes P., 2006, Monthly Notices of the Royal Astronomical Society, 371, 1269

Terrazas B. A., et al., 2020, Monthly Notices of the Royal Astronomical Society, 493, 1888

Theron I. P., Lehmensiek R., de Villiers D. D., 2012, 2012 International Conference on Electromagnetics in Advanced Applications, pp 539–542

Thomas D., Maraston C., Bender R., De Oliveira C. M., 2005, The Astrophysical Journal, 621, 673

Toloba E., et al., 2015, The Astrophysical Journal, 799, 172

Tonry J., 1996, HST Proposal, p. 6579

Toomre A., 1977, in Evolution of Galaxies and Stellar Populations. p. 401

Tornatore L., Borgani S., Dolag K., Matteucci F., 2007, Monthly Notices of the Royal Astronomical Society, 382, 1050

Treu T., Ellis R. S., Kneib J.-P., Dressler A., Smail I., Czoske O., Oemler A., Natarajan P., 2003, , 591, 53

Trujillo I., Ferré-Mateu A., Balcells M., Vazdekis A., Sánchez-Blázquez P., 2013, The Astrophysical Journal Letters, 780, L20

Trussler J., Maiolino R., Maraston C., Peng Y., Thomas D., Goddard D., Lian J., 2020, Monthly Notices of the Royal Astronomical Society, 491, 5406

Tully R. B., Fisher J. R., 1977, Astronomy and Astrophysics, 54, 661

Upadhyay A. K., Oman K., Trager S., 2021, Astronomy & Astrophysics, 652, A16

Van Gorkom J., Knapp G., Raimond E., Faber S., Gallagher J. S., 1986, The Astronomical Journal, 91, 791

Van Gorkom J., Van der Hulst J., Haschick A., Tubbs A., 1990, The Astronomical Journal, 99, 1781

Van den Bergh S., 2009, The Astrophysical Journal, 702, 1502

Verdes-Montenegro L., Yun M., Williams B., Huchtmeier W., Del Olmo A., Perea J., 2001, Astronomy & Astrophysics, 377, 812

Verheijen M. A., 2001, The Astrophysical Journal, 563, 694

Vijayaraghavan R., Ricker P. M., 2013, Monthly Notices of the Royal Astronomical Society, 435, 2713

Vivek A., Sen S., Prerana A., 2022

Vollmer B., Cayatte V., Balkowski C., Duschl W. J., 2001a, , 561, 708

Vollmer B., Cayatte V., Balkowski C., Duschl W., 2001b, The Astrophysical Journal, 561, 708

Wang J., Xu W., Lee B., Du M., Overzier R., Shao L., 2020, , 903, 103

Westmeier T., et al., 2021, Monthly Notices of the Royal Astronomical Society, 506

Wetzel A. R., Tinker J. L., Conroy C., van den Bosch F. C., 2013, , 432, 336

Wilson W. E., et al., 2011, Monthly Notices of the Royal Astronomical Society, 416, 832

Woudt P. A., Kraan-Korteweg R. C., 2001, Astronomy & Astrophysics, 380, 441

Woudt P., Kraan-Korteweg R., Lucey J., Fairall A., Moore S., 2007, Monthly Notices of the Royal Astronomical Society, 383, 445

Wright E. L., et al., 2010, The Astronomical Journal, 140, 1868

Yang T., Hu B., Cai R.-G., Wang B., 2019, The Astrophysical Journal, 880, 50

Yegorova I. A., Salucci P., 2007, Monthly Notices of the Royal Astronomical Society, 377, 507

Yoon H., Chung A., Smith R., Jaffé Y. L., 2017, The Astrophysical Journal, 838, 81

Yuan H.-B., Liu X.-W., Xiang M.-S., 2013, Monthly Notices of the Royal Astronomical Society, 430, 2188

Zabludoff A. I., Mulchaey J. S., 1998, The Astrophysical Journal, 496, 39

Zasov A. V., Saburova A. S., Egorov O. V., Dodonov S. N., 2019, Monthly Notices of the Royal Astronomical Society, 486, 2604

Zeng G., Wang L., Gao L., 2021, Monthly Notices of the Royal Astronomical Society, 507, 3301

Zepf S. E., Ashman K. M., 1993, Monthly Notices of the Royal Astronomical Society, 264, 611

Zhang B., et al., 2013, , 777, 122

Zinger E., et al., 2020, Monthly Notices of the Royal Astronomical Society, 499, 768

Zolotov A., et al., 2015, , 450, 2327

Zwicky F., 1933, Helvetica Physica Acta, 6, 110

Zwicky F., 1937, The Astrophysical Journal, 86, 217

de Gouveia Dal Pino E., Clavijo-Bohórquez W., Melioli C., 2018, arXiv e-prints, p. arXiv:1809.07588

de Wet S., et al., 2021, Astronomy & Astrophysics, 649, A72

2016, Nature, 535, 117

van den Bosch R. C., Gebhardt K., Gültekin K., van de Ven G., van der Wel A., Walsh J. L., 2012, Nature, 491, 729